Departamento de Matemática Aplicada
Facultad de Ciencias
UNIVERSIDAD DE GRANADA

Non-Linear Dynamics in Earth Sciences: Morphology, Self-organized Structures, Pattern Formation and Synchronization

Bruno Escribano

Tesis Doctoral

Granada, 2010

Editor: Editorial de la Universidad de Granada
Autor: Bruno Escribano
D.L.: GR 1974-2011
ISBN: 978-84-694-1143-8

Contents

List of Figures

Chapter 1

General Introduction

The work presented in this thesis involves the study of patterns and morphologies appearing in nature. There are many spatial images that most people would identify as patterns, like for example the repeating designs of wallpaper or carpets, but there is always an element of subjectivity when perceiving patterns and forms. When scientists speak of pattern formation, they usually refer to the visible, ordered formations that are a consequence of self-organization.

Sometimes we find similar patterns appearing in totally independent systems. Sand ripples formed in the desert by the blowing wind can resemble the colored stripes on some animals. Dendritic crystal growth can also form patterns similar to those of tree branches. These similarities are not a coincidence, they are the consequence of common physical principles being applied at the local interactions between the component parts of these systems.

We can find pattern formation almost everywhere in nature. Animal markings such as the leopard's spots or the zebra's stripes are formed during the development of the embryo. Alan Turing explained that the symmetry breaking of the embryo that produces the color pattern is induced through a reaction-diffusion process of two different compounds, an activator and an inhibitor, each with different diffusion rates [3]. These compounds are chemical morphogens that will later be read by the melanocytes in the epidermis, which will accordingly secrete the pigments that color the hair and ultimately produce the stripes or spots on the animals fur. In a similar way, the patterns formed on the exterior of mollusk shells can also be explained by an activator-inhibitor process that controls the deposition of pigment in the calcifying cells at the shell's growing edge [4]. Each cell secretes pigments according to the activating or inhibiting activity of its neighboring pigment cells. The cell band leaves the colored pattern on the shell as it grows slowly.

Patterns formed in the growth of bacterial colonies have been extensively studied experimentally (see Fig. 1.1). The resulting morphologies depend on the growth conditions and their complexity increases with the hardening of the medium or the lack of nutrients. Some of the patterns produced are well known from reaction-diffusion systems in chemistry, such as Turing patterns or those produced by the Belousov-Zhabotinsky reaction. They can be easily modeled using cellular automata, which has proved useful at identifying the most relevant mechanisms for the different morphologies.

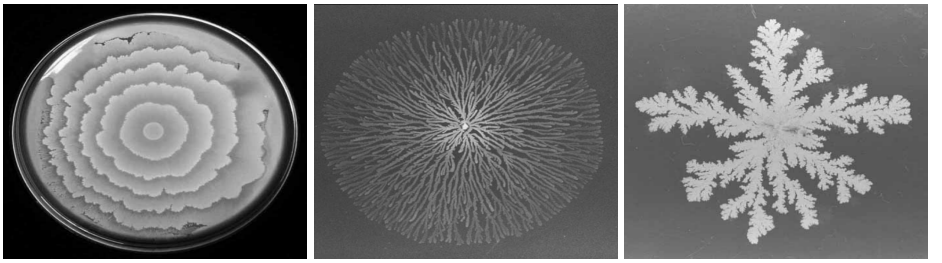

FIGURE 1.1: Patterns formed by bacterial colony growth Bacillus: concentric ring pattern (left), dense branched morphology pattern (middle) and diffusion limited aggregation pattern (right) [5].

Vegetation growing in arid areas can often produce a large variety of distinctive and repetitive patterns that are developed during its expansion. In this case the patterns are usually a consequence of the resource distribution, which may be limited or unevenly concentrated. Sometimes they are produced by an external factor, such as strong directional wind or a sloped landscape. Some examples of patterned vegetation include fir waves and tiger bush (see Fig. 1.2).

Dendritic patterns are quite common in crystallography, paleontology or metallurgy. They are recognizable by a branching morphology that resembles that of a tree. Even the word dendrite derives from the Greek *dendros*, which means *tree*. Dendritic crystal growth is typically exemplified by the snowflake formations, where the microscopic hexagonal lattice symmetry is extended to a macroscopic scale. But not all mineral dendrites preserve their crystallographic symmetry. In fact in order for there to be dendritic crystal growth the process must be out of equilibrium and rich in defects. Regular, faceted crystals grow by accretion of impinging particles that rearrange themselves along the crystal surface forming flat layers. This kind of rearrangement takes place at the surface of a crystal that is growing slowly, since the atoms at the surface can generally pass back into solution again, or move across the surface, until the lowest energy configuration is achieved. In this way a crystal finds its way to a regular stacked network of atoms. But if the particle deposition is too fast to allow enough time for this rearrangement to occur, or if the particles do not have enough energy to relocate

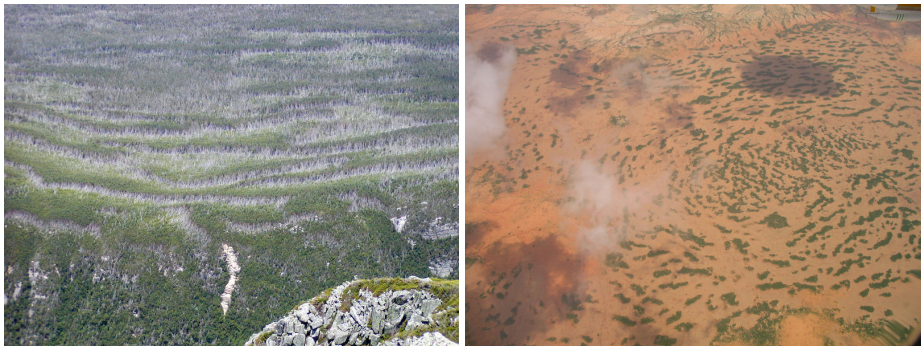

FIGURE 1.2: Fir wave pattern, caused when a row of trees blocks the wind from subsequent rows (left); tiger bush vegetation pattern, caused as a consequence of limited moisture distribution in the ground (right) [6, 7].

(as at low temperature), the particles will just stick together upon contact. In these conditions, particles simply diffuse randomly through the medium until they find a cluster or surface to stick to. So there is no preferred crystallographic direction and growth rate is defined by the rate of diffusion of the particles. This growth regime is known as diffusion-limited aggregation (DLA) and was first described by Witten and Sandler [8]. Once the regular faceted crystal growth is disturbed, any bump or protrusion in the surface will be a preferential deposition spot, as it sticks out into the medium and is more likely to catch diffusing particles. In this way a bump will become a finger that will grow faster than the rest of the crystal surface. As its growth progresses, it will acquire surface irregularities of its own that will produce further branching and the whole system will develop a fractal morphology.

FIGURE 1.3: Sand ripples formed by the desert wind (left) and zebra stripes formed by the presence or absence of melanin [9, 10].

Sand ripples and dunes are patterns commonly appearing in deserts as a consequence of the interaction between the wind and the sand grains. These formations are not motionless topographic features, but instead travel and flow as water ripples do on the sea's surface. It is well known that granular media can sometimes behave as liquids, a property known as liquefaction. The formation process of sand ripples was described in detail by Bagnold [11] as an example of a growth instability. When a steady wind continuously sweeps a sandy plain, it picks up surface grains and carries them elsewhere. If there is a random bump on the plain surface, the deposition rate of sand grains is increased at this spot. As more sand is deposited, the barrier becomes larger, in turn favoring more deposition on its windward side, but at the same time it inhibits the deposition at the downwind side by depleting the amount of sand grains carried in the wind. In this way the first ripple is formed, which in turn triggers by its presence the appearance of another ripple downwind. In fact, the whole process can also be regarded as an activator-inhibitor process, just as the formation of stripped patterns on animal skin. The process continues and develops into a ripple field with a characteristic wavelength that will depend on the wind speed, angle and grain size. Sand ripples typically are a few centimeters high with wavelength between centimeters and a few meters. Dunes are generated in the same way but at a larger scale, with wavelengths from ten to several hundred meters.

One last example worth mentioning are those patterns that, while being of inorganic nature, give us the appearance of having a biological origin. We have learned to instinctively identify living organisms by their shape. They have a complex form with some sort of regularity (bilateral symmetry of bodies, branching in trees...) but not the geometric symmetry of crystals. We must, however, be aware that shape alone is not enough to discriminate the organic from the inorganic, an assumption that has led to several mistakes in the recent history of science. In mineralogy and paleontology, dendritic mineral crystals are often mistaken for fossils. These crystals are formed when naturally occurring fissures in the rock are filled by percolating mineral solutions. Water rich in manganese and iron flows along fractures in the rock and deposits dendritic crystals as the solution flows through. Another possible example are the rock formations known as stromalites. They are found in ancient reef environment around the world and their origin is still been disputed. Their morphology has led scientists to believe that they are the fossil remains of mat-like structures created by marine microorganisms such as cyanobacteria. If this was true, they would be some of the oldest evidence for life on Earth, dating back to more than three billion years. However, it has also been proved that the typical stromalite morphology can also be generated by simple physical processes of sedimentation and precipitation of minerals from the overlying water [12].

This precaution is specially relevant for astrobiologists looking for evidence of life on other planets and moons. In 1984 a four billion year old meteorite of Martian origin was found in Allan Hills, Antarctica. Upon further studies, scientists from NASA announced in 1996 that they had found microscopic worm-like features on the meteorite and suggested that they might be fossilized remains of bacteria [13]. There is still an

ongoing debate over whether this should be considered the first true evidence of extraterrestrial life or just a collection of patterns formed through inorganic processes.

The works presented in this thesis study several examples of morphologies, self-organized structures, pattern formation and synchronization appearing in earth sciences. We use a non-linear dynamics approach and focus our interest on the basic physical and chemical interactions that are responsible for each described phenomenon.

Our research about ice was triggered by the possibility of finding a morphological change between amorphous ices of different densities, and some very interesting morphology patterns were found. This work was part of a project of the Spanish Research Council (CSIC), where 5 research Institutes of Spain were involved in different aspects of the Ice Science from a multidisciplinary focus. In our work in nacre we tried to find a simple mathematical model based on liquid crystal bi-dimensional growth to explain the nacre surface patterns found on bivalve shells. We managed to reproduce said patterns using few mathematical rules on a cellular automata model. Our chemical garden studies started when NASA and Bioserve Space Technologies from University of Colorado (USA) gave us the chance to perform these classic experiments in microgravity conditions on the International Space Station. The morphologies of these self-organized systems are biomimetic and cannot be controlled yet. We have found some explanations for the formation of these morphologies. In our work on tidal synchronization we have tried to approach tidal forces and their effects on satellite orbits using a dynamical system that reduces the problem to its simplest physical principles.

In our research into these diverse topics, rather than seeking out arcane details, we looked into the fundamental science underlying each of these processes, always keeping a critical mind and trying to separate the essentials from the expendable. Therefore, in this work very different phenomena of self-organized pattern formation are treated in the macrophysical process of tidal synchronization, in the nanophysical process of ice formation, in the chemical physical process of chemical garden formation, and in the more complex biophysical process of nacre formation.

Part I

Tidal Synchronization

Chapter 2

Tidal Synchronization: Introduction

Tidal forces arise from the differential gravitational pull exerted from a primary body, for example a star or a planet, upon the different parts of an orbiting secondary body, a satellite. The gravitational force will be stronger on the side of the secondary that is closer to the primary body and will be weaker on the opposite side, producing a pair of forces that can affect not only the state of the secondary but its orbit as well. This effect works both ways, so the secondary will also produce tidal forces on the primary, although of a smaller magnitude because the secondary body is by definition always lighter than the primary [14]. In this work we study the effects of tidal forces on orbit synchronization and their influence on orbital parameters. We use a dynamical systems approach, reducing the system to its most fundamental principles and trying to reproduce the effects of tidal forces seen in our Solar System with computer simulations based on a very simple model.

Effects of tidal forces

If we consider astronomical bodies to be elastic spheres, which is reasonable for bodies bigger than a minimum size where gravity makes them spherical, the effect of a tidal force is to distort the shape of the body without changing its volume. The sphere becomes an ellipsoid, with two bulges, pointing towards and away from the other body. Figure 2.1 shows the differential force of gravity on a spherical body exerted by another. This is what happens to the Earth's oceans under the influence of the Moon's gravity and is the reason why in general we have two high and low tides every 24 hours. But the planet or satellite that is subjected to gravity does not need to have a liquid surface to show the effects of tidal forces. In a general sense, the strains caused by tidal forces

on both bodies can deform them and, in extreme cases, disintegrate them. The Roche limit is the closest distance an object can come to another object without being pulled apart by tidal forces supposing its cohesion comes only from gravity, so a large moon orbiting inside the Roche limit of a planet will be destroyed. It was first described by Edouard Roche in 1848[15].

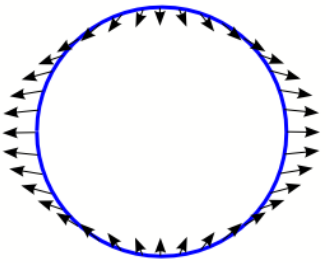

FIGURE 2.1: Differential tidal forces produced by gravity.

If a body is rotating while being subjected to tidal forces, internal friction results in gradual dissipation of its rotational kinetic energy as heat. If the body is close enough to its primary, this can slow down the rotation speed until it becomes similar to the orbiting speed. Then we say that the satellite is tidally locked or has a synchronous rotation and always shows the same side to its primary, as in the case of the Earth's Moon. Tidal heating can also produce earthquakes and volcanic activity, as in the case of Jupiter's moon Io.

Tidal forces can also contribute to ocean currents, which moderate global temperatures by transporting heat to the poles. It has been suggested that they may have an influence in climate change [16]

Tidal acceleration

Tidal acceleration is an effect of tidal forces between an orbiting satellite and the primary planet that it orbits. The acceleration is usually negative, as it causes a gradual slowing and recession of the satellite in a prograde orbit away from the primary, and a corresponding slowdown of the primary's rotation. The process eventually leads to tidal locking of first the secondary, in a synchronous rotation, and then the primary, producing a synchronous orbit in which both bodies always show each other the same side. The similar process of tidal deceleration occurs for satellites that have an orbital period that is shorter that the primary's rotation period or that orbit in a retrograde direction.

The best example of this effect is the Earth-Moon case. The mass of the Moon is sufficiently large, and it is sufficiently close to raise appreciable tides in the matter of the Earth. In particular, the water of the oceans bulges along both ends of an axis passing through the centers of the Earth and the Moon. The average tidal bulge closely follows the Moon in its orbit, and the Earth rotates under this tidal bulge in just over a day. However, the rotation drags the position of the tidal bulge ahead of the position directly under the Moon. As a consequence, there is a substantial amount of mass in the bulge that is offset from the line through the centers of mass of both bodies. The differential gravitational pull from these offset bulges produces a torque between the Earth and the Moon which tends to boost the Moon in its orbit and decelerate the Earth in its rotation.

The conclusion is that the length of the Earth's day is becoming longer, approximately at a rate of 2 ms every 100 years[17]. If there were no other effects involved, this acceleration would continue until the rotational period of the Earth matched the orbital period of the Moon. If that were to happen, the Moon would only be visible from half of the Earth's surface. However, the Earth-Moon system will not reach that state because the Sun's radiation will vaporize the water masses on Earth long before, which will remove the bulk of the tidal friction and acceleration.

The second consequence of the gravitational torque between the Moon and the tidal bulge of the Earth is the promotion of the Moon to a higher orbit. We can explain this effect through the conservation of energy and angular momentum. Energy and angular momentum are transferred from the rotation of the Earth to the orbit of the Moon. The Moon stores this energy by moving farther away from the the Earth, so its potential energy in the Earth's gravity well increases. It stays in orbit and from Kepler's 3rd law it follows that its velocity actually decreases, so the tidal action on the Moon actually causes a deceleration of its motion across the celestial sphere.

Tidal locking

We say a satellite is tidally locked to a primary when its rotation and orbit periods are similar, so the same side of the satellite always faces the primary. This is the most stable configuration for any binary system. Usually it is the satellite which becomes tidally locked to the primary because it is lighter, but if the difference of mass between the two bodies and their physical separation is small, they both may become tidally locked to the other, as in the case of Pluto and its moon Charon.

The change in rotation rate necessary to tidally lock a body B to a larger body A is caused by the torque applied by A's gravity on the bulges it has induced on B by tidal forces. The angular momentum of the whole A-B system is conserved in this process, so that when B slows down and loses rotational angular momentum, its orbital angular momentum is boosted by increasing the orbital radius. The opposite situation happens

when B has an initial rotational angular velocity slower than its orbital angular velocity. In that case tidal locking would speed up its rotation and lower its orbit. In some cases where the orbit is eccentric and the tidal effect is relatively weak, the smaller body may end up in an orbital resonance instead of tidally locked. This state is achieved when the rotational period and the orbital period of the secondary have a relation of integer numbers, p:q, different from 1:1. The best studied case is the orbit of Mercury around the Sun, which is locked in a 3:2 resonance.

A similar effect is experienced by the larger body A, but at a slower rate because B's gravitational field is weaker due to B's smaller mass. For example, the Earth's rotation is gradually slowing down because the Moon's gravity. This increases the duration of our days by an amount that can be measured over geological time in some fossils.

Most significant moons in the Solar System are tidally locked with their primaries, since they orbit very closely and tidal force increases rapidly with decreasing distance. Notable exceptions are the irregular outer satellites of the gas giant planets, which orbit much farther away than the large well-known moons. Pluto and Charon are an extreme example of tidal lock. Charon is a relatively large moon in comparison to its primary and also has a very close orbit. This has made Pluto also tidally locked to Charon. Close binary stars throughout the universe are also expected to be tidally locked with each other.

Tidal heating

Tidal heating occurs through the tidal friction processes explained above: orbital and rotational energy are dissipated as heat in the crust of the moons and planets involved. The most extreme example is Io, one of Jupiter's moons, which is the closest orbiting 'big' moon found in our solar system. It is the most volcanically active body in the solar system and has no surviving impact craters on its surface. The reason why Io is subjected to greater tidal forces than other moons resides in its eccentric orbit combined with Jupiter's large mass and the proximity of its orbit. Io's tidal bulges can vary in height by 100 meters over the course of an orbit, which produces a large amount of friction that heats up the interior of the moon.

A similar process, although weaker, is thought to have melted the lower layers of the ice surrounding the rocky mantle of Jupiter's next large moon, Europa. Saturn's moon Enceladus is similarly thought to have a liquid water ocean beneath its icy crust (see Figure 2.2). The water geysers which eject from its surface are thought to be powered by friction generated by tidal forces.

In this work we have tried to approach tidal forces and their effects on satellite orbits using a dynamical system that reduces the problem to its simplest physical principles.

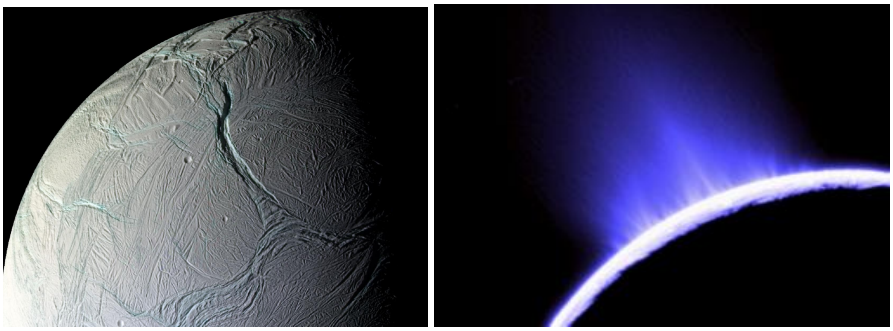

FIGURE 2.2: Saturn's moon Enceladus is thought to have a liquid water ocean beneath its icy crust. The water geysers which eject from its surface are thought to be powered by friction generated by tidal forces. [18]

Despite its simplicity, our model reproduces most of the effects of tidal forces observed in our solar system.

Chapter 3

Dynamics of tidal synchronization and orbit circularization of celestial bodies

3.1 Introduction

What is the dynamical origin of the fact that the Moon presents the same hemisphere facing perpetually towards the Earth? The other large moons of the solar system also have their rotations synchronized with their orbits, and Pluto and Charon are mutually locked in this way. All of these celestial bodies are in 1:1 spin–orbit resonance. The rotation of one planet, Mercury, is also synchronized with its orbit around the Sun, but it performs three rotations every two orbits, and thus, unlike the former instances, is locked not in 1:1, but instead in 3:2 resonance [14]. Similar synchronization phenomena are thought to occur too in solar systems with so-called 'hot Jupiters' or short-period planets [19], and in systems of binary stars [20], whose orbits also evolve to become circular. All these instances are clearly a consequence of a spin–orbit interaction brought about by the gravitational torque exerted by the larger primary body on the smaller secondary body elastically deformed by the differential gravity combined with the corresponding tidal friction induced in the secondary. The phenomenon has long been studied [21, 22], but existing models [23–27] are designed for quantitative analysis of a specific instance or a particular part of the problem, and are correspondingly complicated; the details obscure the basic mathematical structure of the dynamical system.

Here we take the opposite course: we study the simplest possible system that displays tidal synchronization and orbit circularization with a minimal model that takes into

account only the essential ingredients of tidal deformation and dissipation in the secondary body. In our qualitative dynamical-systems approach, without including the full panoply of details, we treat in a self-consistent way the temporal evolution of the eccentricity and the energy flow from orbital to rotational motion; important ingredients to understand the long-term evolution of the orbit. Despite its simplicity, our model can account for both synchronization into the 1:1 spin-orbit resonance and the circularization of the orbit as the only true asymptotic attractors, together with the existence of relatively long-lived metastable orbits with the secondary in p:q (coprime integers) synchronous rotation.

From the point of view of dynamical-systems theory, this phenomenon of synchronization is of even broader interest than its application to celestial dynamics, because it belongs to a relatively little studied class of dissipative systems that contain an embedded submanifold of conservative motion. Other examples, unrelated in physical origin but with this same mathematics, are the dynamics of neutrally buoyant particles in incompressible fluid flows [28], the bailout embedding of volume-preserving and Hamiltonian dynamics [29] and strategies to control Hamiltonian systems [30].

3.2 Experimental methods

We model an extended secondary body of mass m by two point masses of mass $m/2$ connected with a damped spring; see Figure 3.1a. This composite body moves in the gravitational field of a primary of mass $M \gg m$ located at the origin. In this simplest case oscillation and rotation of the secondary are assumed to take place in the plane of the Keplerian orbit. We use polar coordinates r, β for the center of mass of the secondary, with l as the instantaneous length of the spring and ϕ the rotational angle characterizing the orientation of the secondary. Both angles β and ϕ are measured from the x-axis in an inertial reference frame. The spring is characterized by its spring constant D and rest length L_0. The gravitational interactions of both point masses with the primary are taken into account, but that between the point masses is neglected. To describe the conservative part of the dynamics we construct a dimensionless Lagrangian in terms of the generalized coordinates $\vec{q} = (r, \beta, l, \phi)$:

$$\mathscr{L} = \frac{\dot{r}^2}{2} + \frac{r^2\dot{\beta}^2}{2} + \frac{\dot{l}^2}{8} + \frac{l^2\dot{\phi}^2}{8} + \frac{1}{2r_1} + \frac{1}{2r_2} - \frac{\omega^2}{8}(l-l_0)^2, \tag{3.1}$$

where $r_i = \left(r^2 + l^2/4 + (-1)^i rl\cos(\phi-\beta)\right)^{1/2}$ is the distance of the ith component of the secondary to the primary. $\mathscr{L}$ is measured in units of $(mL^2)/(T^2)$, where the unit of length L is chosen to be the major semiaxis a_0 of the initial Keplerian orbit, and the unit of time $T = (a_0^3/fM)^{1/2}$ is $1/(2\pi)$ times the period of the Keplerian orbit. The dimensionless vibrational frequency and natural spring length are $\omega = \sqrt{4D/m}T$ and $l_0 = L_0/a_0$. The damping of the spring is introduced via a dimensionless Rayleigh

dissipation function, $\mathscr{F}(\dot{l}) = \frac{1}{4}\gamma \dot{l}^2$, where γ is the dimensionless damping constant. The equations of motion are then given by the modified Euler–Lagrange equations [31]

$$\frac{d}{dt}\frac{\partial \mathscr{L}}{\partial \dot{q}_k} - \frac{\partial \mathscr{L}}{\partial q_k} = -\frac{\partial \mathscr{F}}{\partial \dot{q}_k}, \quad k = 1, \ldots, 4; \tag{3.2}$$

the set of dimensionless parameters is γ, l_0, ω, and the eccentricity of the initial Keplerian orbit, ε_0. We take the initial conditions at apapsis, the greatest distance of the center of mass of the secondary from the primary on the initial Keplerian ellipse: $r(0) = 1+\varepsilon_0$, $\dot{r}(0) = 0$, $\beta(0) = 0$. This condition, along with the value of the eccentricity ε_0, determines $\dot{\beta}(0)$. $\dot{\phi}(0)$ was chosen in the range $(0,5)$ with $\phi(0)$ typically zero and $\dot{l}(0) = 0$, and $l(0)$ was specified as the value corresponding to a steady rotation with angular velocity $\dot{\phi}(0)$ in the absence of any gravitational force. The numerical solution of the equations of motion was carried out with a fourth-order Runge-Kutta method at fixed step size $\Delta t = 2\pi/1000$.

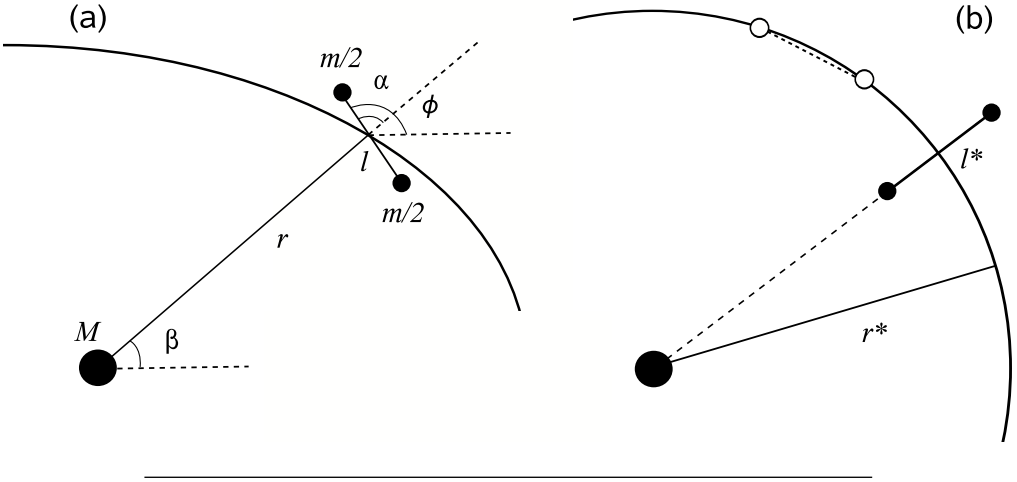

FIGURE 3.1: (a) Instantaneous configuration of the system given by the generalized coordinates r, β, l, ϕ. The relative angle $\alpha = \phi - \beta$ is indicated. (b) Two conservative synchronized configurations on a circular orbit of radius r^*. That of the black circles, corresponding to a solution of Eqs (3.3) with the spring stretched ($l^* > l_0$), is stable. The other of white circles and the spring relaxed is unstable.

Owing to the damping, the only energy-conserving trajectories of the system are those that maintain the distance between the two point masses making up the secondary constant. These trajectories can only be circular and just two configurations for such orbits are possible: either the two bodies travel along the same circular orbit at a constant distance r^* from the primary or they occupy the same radial line while traveling around two different concentric circular orbits; see Figure 3.1b. In the latter case the radii of the two orbits $r_1^* < r_2^*$ must satisfy the balance between the centrifugal, elastic and

gravitational components of the force,

$$\left(\frac{a_0}{r^*}\right)^3 r_i^* = \frac{1}{r_i^{*2}} + (-1)^i \frac{\omega^2}{2}(r_2^* - r_1^* - l_0) \tag{3.3}$$

where $(a_0/r^*)^{3/2}$ is the dimensionless orbital angular velocity along the asymptotic circular orbit of radius r^*. It is intuitively clear and readily verifiable by solving Eqs (3.3) that the equilibrium size $l^* = r_2^* - r_1^*$ is greater than l_0, so that the composite secondary body is stretched in this state.

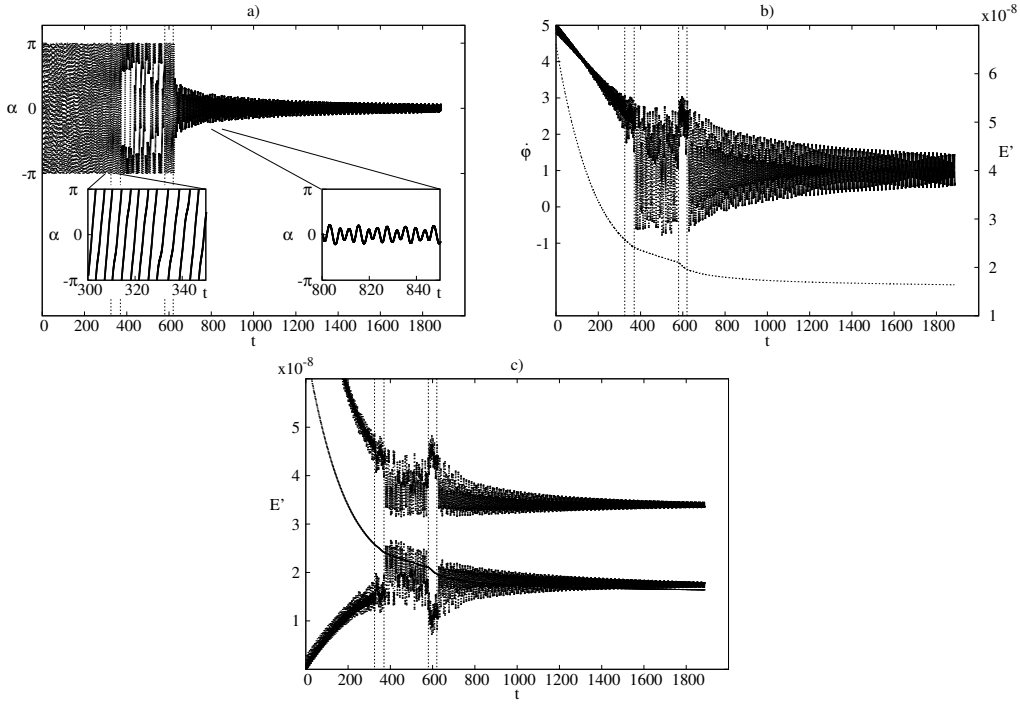

FIGURE 3.2: (a) Angle α versus time t. (b) Angular velocity $\dot{\phi}$ versus time. The decay of the mechanical energy E (thin line) is also shown. Different subregimes are separated by dashed vertical lines; note that the energy decay differs between them. (c) Energy of the different subsystems (shifted by constants) versus time. Smooth line: total energy $E' = E + 1/2$, lower curve: center-of-mass energy $E' = E_c + 1/2$, upper curve: rotational and vibrational energy $E' = E_r + E_v + 3.5 \cdot 10^{-8}$ (cf. Eq. (3.4)).
$\varepsilon_0 = 0.1$, $\gamma = 1.0$, $l_0 = 10^{-4}$; the initial condition is $\phi(0) = 0$, $\dot{\phi}(0) = 5$.

3.3 Results

Figure 3.2 shows a numerical computation of the angle α and angular velocity $\dot{\phi}$ of the secondary as a function of time; the behavior seen is typical for all the parameters investigated for initially rapidly rotating secondaries. A strong initial decay is followed by irregular (transiently chaotic) rotation of the secondary. This may be interrupted by trapping into different resonant states in which the ratio of the rotational and orbital periods is a rational number. Although the use of the term 'resonant' is typically applied to Hamitonian problems, we use it here in the context of a weakly dissipative system since these states appear as attractors or metastable attractors. Eventually, a roughly exponential decay sets in towards a steady state. Two qualitatively different regimes can be observed in the time dependence of the angle α in Figure 3.2a: regimes of rotation and of libration, the details of which are exemplified in two insets. The first regime consists of four different subregimes which can best be distinguished on an angular velocity versus time plot. These subregimes are separated by dashed lines in Figure 3.2b. After an initial deceleration phase the angle dynamics is trapped into resonance; a 5:2 resonance in this case. This is followed by an irregular rotation which ends by a further approach to a resonant state; the same one as before in this particular example. The escape from this state occurs in the form of damped oscillations. Figure 3.2c displays how the energy of the different subsystems changes with time. The total dimensionless energy E is split into a center-of-mass energy, a rotational energy, and a vibrational energy $E = E_c + E_r + E_v$ as

$$\begin{aligned} E_c &= \frac{1}{2}\left(\dot{r}^2 + r^2\dot{\beta}^2\right) - \frac{1}{r}, \\ E_r &= \frac{1}{8}I^2\dot{\phi}^2 - \frac{1}{2r_1} - \frac{1}{2r_2} + \frac{1}{r}, \\ E_v &= \frac{1}{8}\left(I^2 - \omega^2(I - I_0)^2\right). \end{aligned} \tag{3.4}$$

Figure 3.2c demonstrates that in spite of the overall initial decay of energy, the center-of-mass energy increases, i.e., rotation and vibration pump energy into the Keplerian orbit. In the chaotic stage, the subsystem energies E_c, E_r, and E_v all change irregularly, while the total energy decays smoothly, and slower than originally. Around resonances the center-of-mass motion pumps energy into the rotational and vibrational degrees of freedom: a regular center-of-mass motion is an efficient driving of the secondary's internal dynamics. This accumulated vibrational energy quickly dissipates in the last phase. Since the total energy is dominated by the center-of-mass motion, the total decrease of the major semiaxis can be estimated via the Keplerian rule $E^*/E_0 = a_0/r^*$, where E_0 and E^* denote the initial and asymptotic total energy.

On intermediate time scales metastable attractors may appear. In particular, the 3:2 resonance may be present for a long period of time. It is, however, asymptotically unstable, and the 1:1 state finally sets in. We see in Figure 3.3, which shows the average

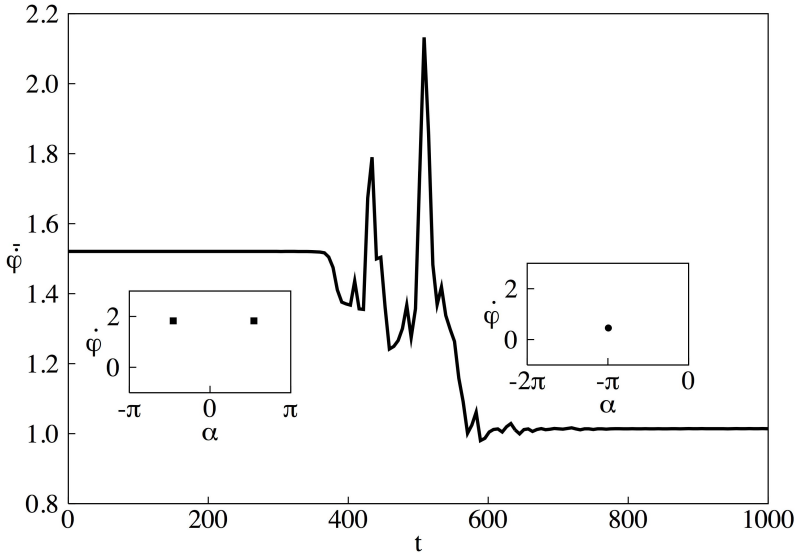

FIGURE 3.3: Average angular velocity $\overline{\dot{\phi}}$ versus time for $\varepsilon_0 = 0.2$, $\gamma = \omega = 10$, $l_0 = 10^{-4}$ shows the crossover from 3:2 to 1:1 resonance. The initial condition is $\phi(0) = 1.2$, $\dot{\phi}(0) = 1.0$. The insets show the metastable 3:2 and asymptotic 1:1 attractors on the Poincaré map $\dot{\phi}, \alpha$ taken at apapsis. Time is measured in units of T. The transition shown occurs after the system has spent a long time, $t = 3.73522 \cdot 10^7$, in the 3:2 resonance, and is very abrupt, lasting 300, or about 50 periods. The average angular velocity on the first plateau is somewhat larger than 1.5 because the semiaxis has decreased by a few percent by this time.

angular velocity between two successive apapses, that the crossover between the two resonances is rather abrupt, without any long-lasting transients. A change in the the parameters or the initial conditions can also lead to a decay direct to 1:1 resonance without an appearance of the metastable 3:2 attractor. Other resonant states can also appear as metastable attractors. Figure 3.4 presents a case with a 9:4 resonance. Here the transients are very long, with pronounced chaos. Figure 3.4a shows angle α at apapsis versus time; its appearance is that of a bifurcation diagram. A large period-four window appears in the middle of the chaotic regime, and a more detailed investigation reveals further windows. The metastable chaotic and period-four attractors are shown in the insets. Figure 3.4b presents the periapsis precession — the change $\Delta\beta$ of the angle between apsidal points — as a function of time. There is a sudden decrease of this quantity in the periodic windows, but the arrival at the asymptotic 1:1 attractor is marked by a sudden jump upwards followed by a slow decrease towards zero.

The long-term dynamics always leads to the 1:1 resonance and the energy approaches a constant value; cf. Figure 3.2c. This implies that the full dissipative dynamics converges to a conservative asymptotic state in which the secondary no longer vibrates but

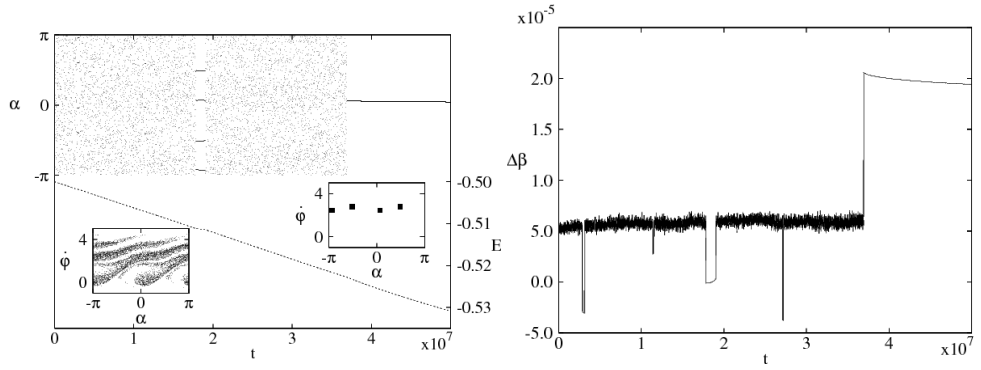

FIGURE 3.4: Long chaotic transients before arrival at 1:1 resonance: (a) Angle α taken at apapsis points versus time and energy E versus time (dashed line) for $\varepsilon_0 = 0.4$, $\gamma = 20$ and initial condition $\phi(0) = 0$, $\dot{\phi}(0) = 3.5$. The insets show the chaotic and periodic quasiattractors on a Poincaré map. (b) Periapsis precession $\Delta\beta$ versus time. Note the sudden changes in the periodic windows.

behaves as a rigid body orbiting in a circular Keplerian orbit. In order to characterize the approach to this state, we may follow the eccentricity as a function of time. The decay is exponential, but the decay rate varies dramatically with the parameters. The different decay curves however follow the same long-term exponential form when plotted as a function of a rescaled dimensionless time t'. In the range $\omega > 10$, the scaled time is $t' = t\gamma l_0^2 \omega^{-4}$. Figure 3.5 shows the collapse of a large number of data onto a master curve in this representation. The characteristic relaxation time τ is thus found to scale for $\omega > 10$ as $\tau \sim \omega^4/(\gamma l_0^2)$ in the original dimensionless time. The asymptotic state of $\varepsilon = 0$ is approached to a good approximation after some 2–3 τ. For $\gamma = 1$, $l_0 = 10^{-4}$, and $\omega = 10$, for example, the relaxation time is on the order of 10^{10}. The scaling relation in dimensional form reads:

$$\tau_{dim} \sim \frac{1}{\gamma_{dim}} \frac{4^2 D^2}{m^2} \frac{a_0^6}{f^2 M^2} \frac{a_0^2}{L_0^2} = \frac{1}{\gamma_{dim}} \left(\frac{T_{orb}}{T_{osc}}\right)^4 \left(\frac{a_0}{L_0}\right)^2,$$

where T_{osc} is the period of oscillation and T_{orb} the orbital period of the secondary. For a given material composition of the secondary, γ_{dim} and the speed of the elastic waves $c \sim L_0/T_{osc}$ are constants, and the despinning time depends strongly on the size of the secondary and its distance to the primary, which is why large moons are locked to their planets but most planets are not locked to the Sun. This scaling illustrates a interesting feature of the tidal problem: the relaxation time γ_{dim}^{-1} of the isolated oscillator is increased by several orders of magnitude owing to the broad separation of length scales and frequencies. In order to be dissipated by the damping, the energy must be transferred from the orbital and rotational Hamiltonian degrees of freedom to the vibrational one, and this transfer, mediated by the tidal forces, is rather inefficient if the secondary

is small. This inefficiency suggests the interesting idea of modeling the secondary in an increasingly complex way as an ensemble of masses linked with conservative — perhaps nonlinear — springs. This might allow for the spontaneous appearance of tidal dissipation as the energy injected by the orbit into the secondary as internal energy thermalizes faster than the time it takes to be fed back into the orbit, and could allow for tidal synchronization and circularization even when no damping at all is present in the secondary if the number of internal degrees of freedom were large enough.

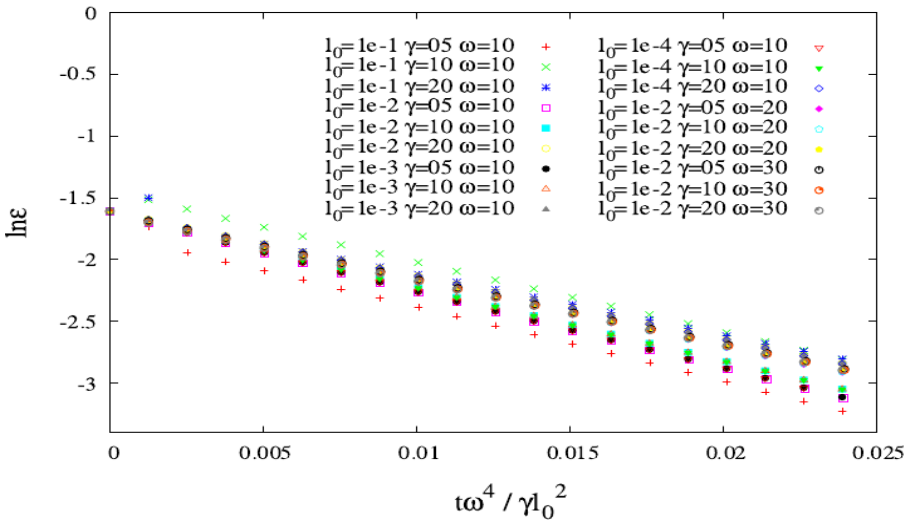

FIGURE 3.5: Master curve of the logarithm of eccentricity ε versus rescaled time $t' = t\gamma l_0^2 \omega^{-4}$ for initial eccentricity $\varepsilon_0 = 0.2$, and $\omega = 10,\ 20,\ 30$, $l_0 = 10^{-n}$, $n = 1,2,3,4$ and $\gamma = 5,\ 10,\ 20$ on a log–linear scale. The initial condition is in all cases $\phi(0) = 0$, $\dot{\phi}(0) = 4$.

3.4 Discussion

We have introduced here a minimal model that displays the physics of tidal synchronization and orbit circularization without the complexity of an extended body. Although the model does not contain many realistic aspects of real satellites (e.g. that they distort along the satellite-planet line, and not along a principal axis), it faithfully describes the basic aspects of tidal synchronization and orbit circularization. Extensions of the model could eventually include the addition of a nonzero obliquity of the spin axis of the secondary; a more complex secondary; and quasiperiodic or chaotic forcing, as in the three-body problem. We shall develop these ideas in future work.

Chapter 4

A minimal dynamical model for tidal synchronization and orbit circularization

4.1 Introduction

Ever since Darwin [32] models have been constructed of the tidal synchronization of the Moon and other celestial bodies [19–27, 33]. These models have become more quantitatively accurate, but at the same time more complex, so that it is not particularly clear what are the essential features of the problem. Here we take the opposite approach: we strip the problem of tidal synchronization to its bare bones with a minimal model that captures just the qualitative dynamical aspects of the problem. In previous work we introduced the model [34]; here we investigate in depth the complex dynamics that can arise from this simplest model of tidal synchronization and orbit circularization.

To our knowledge there are only two approaches modeling the tidal interaction as a few-body problem. Hut [35] investigated a close binary system where the primary is modeled by three gravitationally interacting point masses (the secondary is point like). Equilibrium tides are described, and the effect of weak friction is taken into account by means of the introduction of a constant time lag. In the approach of Hurford et al [36] the primary is modeled as a sphere coupled to two small point masses via damped springs which do not keep their straight shape but can become curved. The point-like secondary can move along a spherical orbit only and the primary is assumed to spin uniformly.

Although our model consists of two point masses only bound with a damped spring (as the secondary), no specific restrictions are applied. We can thus study dynamical

tides, the nonuniform rotation of the secondary, resonances between rotation and orbital motion, and the effect of circularization. This simple model fundamentally differs from others where the secondary is described as a spatially extended object. The two-point-mass feature is nevertheless similar in spirit to restricting those models to the $l = 2$ normal mode, as done e.g. in Mardling [20], [37] and Witte et al [38]. It is perhaps due to this feature that we find chaotic dynamics as Mardling [20] did although, owing to the presence of dissipation, in our case chaos is unavoidably of a transient character.

Our elementary model also enables us to investigate the nature of resonances in detail. We introduce a new definition of resonant states based on a resonance function which distinguishes resonances $p : p$ and $1 : 1$, and clearly characterizes the different types of temporal behavior. A necessary condition for the existence of a resonance is formulated: the energy of the secondary should be constant on average. The response of the dynamics of the secondary to the temporal change of orbital elements can be monitored.

The model is well-defined and easy-to-treat numerically in its original form [34]. Nevertheless, we carry out a large distance Taylor expansion ($l \ll r$) over the exact equations of motion. The approximate equations enable us to identify and isolate the different effects of tidal interactions.

Special attention is paid to chaotic cases where the applicability of the expansion method is nontrivial. Our finding is, that the exact and approximate equations might lead to different resonances (quasi-attractors) owing to sensitivity to the initial conditions, but if the two solutions reach the same asymptotic state, even the second-order approximation provides a rather accurate description of the dynamics over long times. We can also obtain insight into apapsis precession and the temporal change of orbital elements via the approximate equations.

4.2 The model

As in the previous chapter, we model an extended secondary body of mass m by two point masses of mass $m/2$ connected with a damped spring; see Fig. 4.1(a). The spring and damper or dashpot are in parallel in a Kelvin–Voigt configuration [39].

The composite body moves in the gravitational field of a primary of mass $M \gg m$ located at the origin. In this simplest case oscillation and rotation of the secondary are assumed to take place in the plane of the Keplerian orbit. We use polar coordinates r, β for the center of mass of the secondary, with l as the instantaneous length of the spring and ϕ as the rotational angle characterizing the orientation of the secondary. Both angles β and ϕ are measured from the x-axis in an inertial reference frame. The gravitational interactions of both point masses with the primary are taken into account, but that between the point masses is neglected.

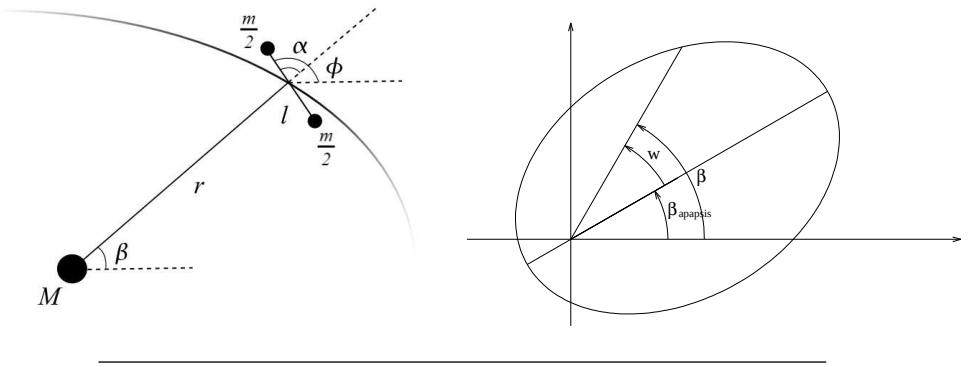

FIGURE 4.1: (a) Instantaneous configuration of the system given by the generalized coordinates r, β, l, ϕ. The relative angle $\alpha = \phi - \beta$ is indicated. (b) Schematic diagram illustrating $\beta_{apapsis}(t)$

To describe the conservative part of the dynamics we use the same dimensionless Lagrangian as in the last chapter, with the initial semi-major axis as the unit of length and the corresponding Keplerian period as the unit of time, in terms of the generalized coordinates $\vec{q} = (r, \beta, l, \phi)$:

$$\mathscr{L} = \frac{\dot{r}^2}{2} + \frac{r^2\dot{\beta}^2}{2} + \frac{\dot{l}^2}{8} + \frac{l^2\dot{\phi}^2}{8} + \frac{1}{2r_1} + \frac{1}{2r_2} - \frac{\omega^2}{8}(l - l_0)^2, \tag{4.1}$$

where $r_i = \left(r^2 + l^2/4 + (-1)^{i+1} rl\cos(\phi - \beta)\right)^{1/2}$, $i = 1, 2$, is the distance of the ith component of the secondary to the primary and ω is the vibrational frequency of the spring. After including dissipation proportional to $\dot{l}$ the equations of motion are

$$\ddot{r} = r\dot{\beta}^2 - \frac{1}{2}rR_+ - \frac{1}{4}lR_-\cos(\phi - \beta), \tag{4.2}$$

$$\ddot{\beta} = -2\frac{\dot{r}\dot{\beta}}{r} - \frac{1}{4}\frac{l}{r}R_-\sin(\phi - \beta), \tag{4.3}$$

$$\ddot{l} = l\dot{\phi}^2 - \omega^2(l - l_0) - 2\gamma\dot{l} - \frac{1}{2}lR_+ - rR_-\cos(\phi - \beta), \tag{4.4}$$

$$\ddot{\phi} = -2\frac{\dot{l}\dot{\phi}}{l} + \frac{r}{l}R_-\sin(\phi - \beta), \tag{4.5}$$

where γ is the dissipation constant and the shorthand notation

$$R_\pm = \frac{1}{r_1^3} \pm \frac{1}{r_2^3} \tag{4.6}$$

has been used.

The set of generalized coordinates can be split into two parts. The first subsystem is

related to the orbital motion (r, β) and the second subsystem describes the internal dynamics (rotation, vibration) of the secondary (l, ϕ).

In order to understand the temporal evolution of the full system we can study the energy and angular momentum transfer between the degrees of freedom and subsystems. The angular momenta of the first and second subsystems are defined as

$$N_1 = r^2\dot{\beta} \quad \text{and} \quad N_2 = \frac{1}{4}l^2\dot{\phi}, \tag{4.7}$$

respectively. The angular momentum is transferred between the two subsystems but the sum is conserved as we only have central forces ($N_1 + N_2 = N_0 = const.$). Because $l \ll r$, in practice $N_1 \approx N_0 = const.$ The total energy (E) is split into a center-of-mass energy E_c (energy of the 1st subsystem), a vibrational energy E_{vibr} and a rotational energy E_{rot}, defined as in the previous chapter:

$$E_c = \frac{1}{2}\left(\dot{r}^2 + (r\dot{\beta})^2\right) - \frac{1}{r}, \tag{4.8}$$

$$E_{vibr} = \frac{1}{8}\left(\dot{l}^2 + \omega^2(l-l_0)^2\right), \tag{4.9}$$

$$E_{rot} = \frac{1}{8}l^2\dot{\phi}^2 - \frac{1}{2}\left(\frac{1}{r_1} + \frac{1}{r_2}\right) + \frac{1}{r}. \tag{4.10}$$

With the above equations we can monitor how the energy is transferred from the center-of-mass orbit to vibration and rotation and how the total energy decreases through dissipation. We also define the energy of the secondary as

$$E_{sec} = E_{vibr} + E_{rot}. \tag{4.11}$$

The instantaneous angular momentum and the energy transfer are given by the time derivatives of these quantities ($\dot{E}$, $\dot{N}$).

In order to follow the orbital elements in continuous time, we recall some formulae from the Keplerian problem. The instantaneous dimensionless semi-major axis and the eccentricity can be expressed as

$$a(t) = -\frac{1}{2E_c(t)}, \quad \varepsilon(t) = \sqrt{1 + 2E_c(t)N_1^2(t)} = \sqrt{1 - \frac{N_1^2(t)}{a(t)}}. \tag{4.12}$$

respectively. According to (4.12) the change of E_c plays an important role in the change of the semi-major axis and eccentricity. The angle w between the vector pointing to the center of mass of the secondary and the semi-major axis of the orbit can be obtained

from the Keplerian form $r = p/(1-\varepsilon\cos w)$ as

$$w(t) = \arccos\frac{1-N_1^2(t)/r(t)}{\varepsilon(t)} \tag{4.13}$$

because $p = N_1^2$. So the angle of apapsis — see Fig. 4.1(b) — is

$$\beta_{apapsis}(t) = \beta(t) - w(t). \tag{4.14}$$

In this chapter t_i denote the instants when the secondary is at the apapsis (apapsis passages). If a quantity (f) is followed over such a long time that the change of the orbital elements is significant, we plot the quantity only at the instants t_i. In such cases we use the notation $f(t_i)$. To study the long term behavior of f, we use the time average of the time derivative of f over a suitable time period. The choice of the suitable time period depends on the state of the secondary. Generally, it is one period ($q = 1$) but if the system is in a $p:q$ resonance, the average is taken over q periods.

$$< \dot{f} >_q = \frac{1}{t_{i+q}-t_i}\int_{t_i}^{t_{i+q}} \dot{f}(t)dt. \tag{4.15}$$

4.3 Resonant and chaotic states

In dissipative cases ($\gamma > 0$) there is only one attractor, the 1:1 resonance, and a circular orbit [34]. The approach towards the attractor typically occurs through a series of resonances. Because of the change of orbital elements we introduce the following resonance functions

$$\rho(i) \equiv R(t_i) = \frac{1}{2\pi}\int_{t_i}^{t_{i+1}} \dot{\alpha}\,\mathrm{d}t + 1, \quad i = 1,2,3\ldots. \tag{4.16}$$

The integral term yields the overall rotational angle of the secondary between times t_i and t_{i+1} relative to the r axis in units of 2π; see Fig. 4.1(a). The unit term expresses the fact that the radius has carried out approximately one rotation. Because of the small apapsis precession, R or ρ differ slightly from the entire rotational angle of the secondary (in units of 2π). The resonance function is thus a characteristic of the rotation after eliminating the apapsis precession. If the system is in a $p:q$ resonance, function ρ is periodic in i, its period is q and

$$\sum_{i=1}^{q}\rho(i) = p. \tag{4.17}$$

The reason for the definition of the functions R is that they are more convenient to plot than $\rho(i)$. In the presence of constant apapsis precession, R would be periodic. Because of the time dependence of the orbital elements in our problem, R is not strictly periodic but is almost so. In a p:q resonance, during q orbital periods the rotation of the secondary relative to the r axis is $p-q$ and the average of the relative rotation is $(p-q)/q$. According to Eq. (4.16) the relative rotation during one period is $R-1$. Generally, the relative rotation is not exactly equal to the average of the relative rotation but almost so: $R-1 \approx (p-q)/q$. The average of R is therefore p/q and it typically takes on q different values around the average.

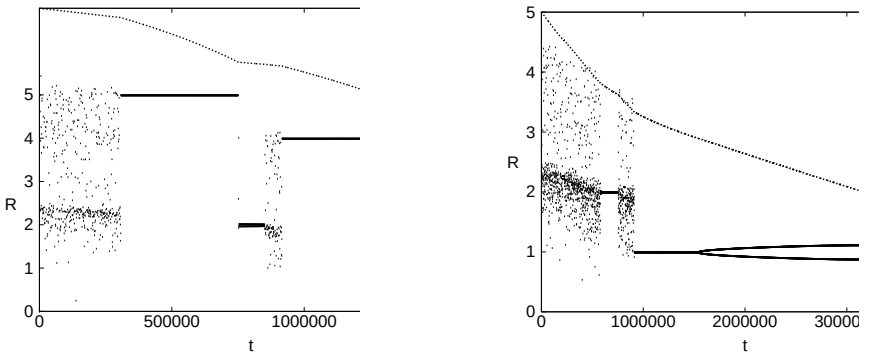

FIGURE 4.2: (a) Resonance function $R(t_i)$ (dots), $\varepsilon(t_i)$ (dashed line). Parameters and initial conditions: $\omega = 10$, $\gamma = 1$, $l_0 = 10^{-3}$; $\varepsilon_0 = 0.4$, $\phi(0) = 0$, $\dot{\phi}(0) = 5$. The series of resonances is 5:1, 4:2, 4:1, 2:2. (b) Resonance function $R(t_i)$ (dots and horizontal continuous lines), $E_c(t_i)$ (dashed line). Parameters and initial conditions: $\omega = 10$, $\gamma = 5$, $l_0 = 10^{-3}$; $\varepsilon_0 = 0.4$, $\phi(0) = 0$, $\dot{\phi}(0) = 5$. The series of resonances is 2:1, 1:1, 2:2, 1:1.

To understand better the features of R, consider two examples. In a 3:2 resonance, during two orbital periods the relative rotation of the secondary is one. During one of the periods the relative rotation is a little smaller than $1/2$ and during the other it is a little larger than $1/2$. Thus in the first case $R < 0.5 + 1 = 1.5$ and in the second case $R > 1.5$. When plotting R versus t_i, if the points are quite dense, we can see two lines near to the value 1.5. The other example is a 2:2 resonant state (see right side of Fig. 4.2(a) and the mid part of Fig. 4.2(b)), which is different from 1:1 resonance. In the former during two orbital periods the relative rotation of the secondary is two. During one of the periods the relative rotation is a little less than 0 (negative) and during the other the relative rotation is a little greater than 0 (positive). Thus in the first period $R < 1$ and in the second $R > 1$. In a 1:1 resonance $R = 1$. Although the average of R is the same in both cases ($\bar{R} = 1$), in a 1:1 resonance the position and the angular velocity relative to the r axis are always the same at apapsis. The 1:1 resonant state and the 2:2 should thus be distinguished from each other because they have quite different features; for example, the amplitude of the libration is larger and the changes of orbital elements

are faster in a 2:2 resonance. In this chapter the term $p:q$ *resonant state* will be used for resonances different from 1 : 1 only.

Fig. 4.2(a) shows an example of the time-dependent resonance function where we also plot the temporal change of eccentricity. It is easy to separate the different regimes in the figure. During the first regime (t=0-300000) the rotation of the secondary is chaotic. The orbital motion drives the secondary. Depending on the orbital elements the driving can cause chaotic rotation. The orbital elements are changing and the type of rotation caused by the driving is also changing. By $t \approx 300000$ the driving cannot cause chaotic rotation and the chaotic regime ends.

The second regime is a resonance. If the system is in a $p:q$ resonance the temporal behavior of the secondary is periodic, thus the average of its energy and the dissipation are constants: $<\dot{E}_{sec}>_q = 0$ and

$$<\dot{E}_{total}>_q = \frac{1}{t_{i+q}-t_i}\int_{t_i}^{t_{i+q}}\left(-\frac{1}{2}\gamma i^2\right)dt = C_{p:q} = const < 0. \tag{4.18}$$

A constant energy of the secondary can only be maintained if the system pumps the dissipated energy from the orbit to the secondary which means

$$<\dot{E}_c>_q = <\dot{E}>_q = C_{p:q}. \tag{4.19}$$

This is an energy condition for the existence of a $p:q$ resonant state. The subscript $p:q$ expresses that the value of C is determined mainly by the type of the resonant state. Of course C also depends on the parameters - e.g., on l_0 - and the orbital elements. The resonant state ends - because of the change of orbital elements - when the system cannot pump enough energy to the secondary. If the energy condition (4.19) is not valid, the resonant state loses its stability. The third regime (near $t \approx 750000$) is quite short. At the beginning of this regime a couple of stable resonant states are present. According to our simulations they behave as quasi-attractors with fractal basin boundaries. If the state of the secondary is close to a boundary between the basins of quasi-attractors, the orbit can exhibit long-time chaos.

The fourth regime is also a resonance. This time the mechanism of the disappearance of the resonance is not the same as in the second regime. The simple quasi-attractor changes into a strange (chaotic) quasi-attractor as a consequence of the change of the orbital elements.

Since all quasi-attractor are simple resonances, any type of chaos present in such dissipative systems can only be of transient type. As is known from the theory of transient chaos [40], [41] the chaotic set is in such cases a non-attracting set, called a chaotic saddle. Orbits initiated close to the stable manifold of the saddle converge towards the chaotic set, stay a long time around it, and will be led eventually to a quasi-attractor

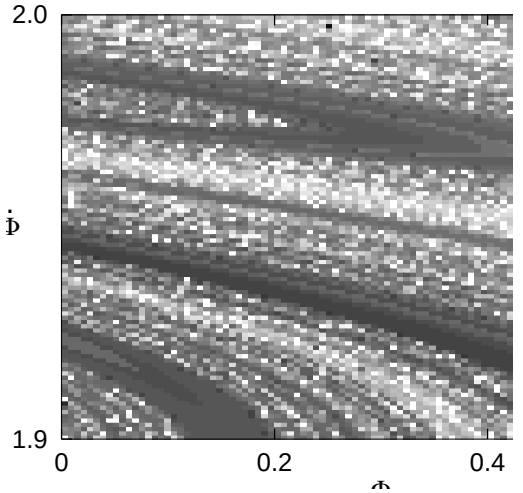

FIGURE 4.3: Lifetime distribution over a piece of the $\phi, \dot{\phi}$ plane with $\dot{l} = 0$. The initial value of l is chosen as $l = l_0/(\omega^2 - \dot{\phi}^2)$. Parameters are $\omega = 10$, $\gamma = 10$, $l_0 = 10^{-4}$, $\varepsilon = 0.1$ (The secondary is at the apapsis). Lifetimes are given in units of orbital periods. The filamentary structure is a manifestation of transient chaos.

along the unstable manifold of the saddle. The presence of a chaotic saddle can be demonstrated by plotting a lifetime distribution over the set of initial conditions. This is done in Fig. 4.3 where a clear fractal filamentation of the long-lived regions can be seen. Although this set of points is similar in appearance to a chaotic attractor, which is an unstable manifold, we emphasize that what we see here is the stable manifold of a chaotic saddle.

We have to distinguish two types of transient chaotic regimes. The first (second) type ends without (with) a change of the orbital elements. In Fig. 4.2(a) the second and fourth chaotic regimes (the short ones) are of the first type and the first and the third chaotic regimes (the longer ones) are of the second type.

The typical behavior of the eccentricity is a decrease toward zero. In every regime but the 1 : 1 resonance the function of eccentricity is piece-wise concave. The semi-major axis also decreases and approaches a given value, a_∞, determined by the initial conditions. The further evolution of the system in this case is that it falls into 1 : 1 resonance around $t \approx 1.1 \times 10^7$, and the eccentricity tends to zero exponentially as the orbit circularizes (see inset of Fig. 4.2(a)).

Fig. 4.2(b) shows another example illustrating that the 1 : 1 resonance can lose stability if the eccentricity is not so small. The figure also shows the center-of-mass energy E_c; our numerical experience is that the change of E_c is exponential only in a 1:1 resonance. In other resonant states the temporal change in E_c is approximately linear (for

an explanation see the next section). Another important feature illustrated in Fig. 4.2(b) is that the decrease of the center-of-mass energy is, in general, more intense in higher resonances than in 1 : 1 resonance.

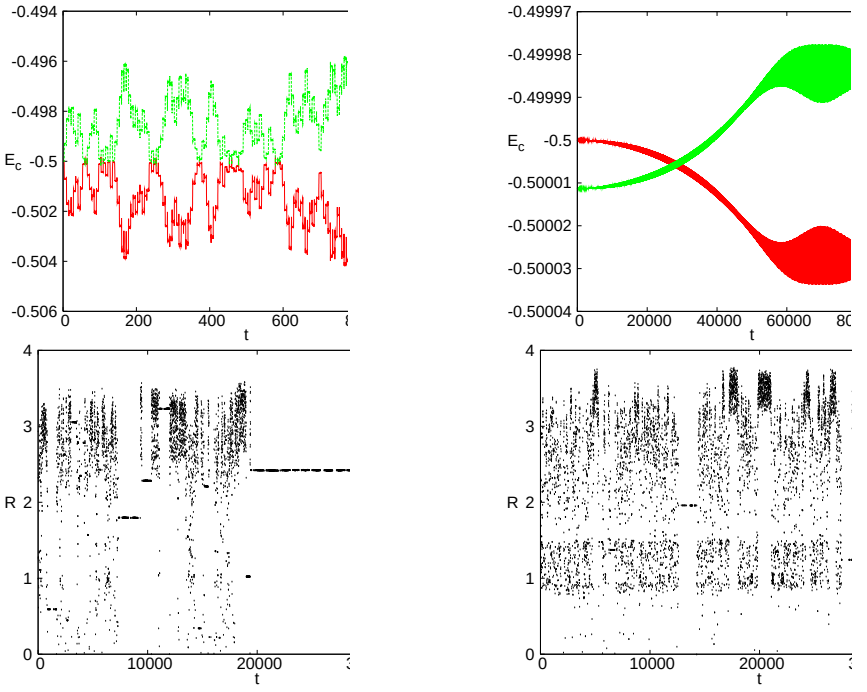

FIGURE 4.4: (a) Energy transfer from the orbit (center-of-mass kinetic energy, red line) to the secondary (rotation and vibration, green line). After some orbits the energy is transferred back to the center-of-mass motion. Longer runs show that this behavior is periodic. (i) $\varepsilon_0 = 0.50$, $\gamma = 0.0$, $l_0 = 1.0^{-2}$, $\omega = 10$. (ii) $\varepsilon_0 = 0.30$, $\gamma = 0.0$, $l_0 = 1.0^{-2}$, $\omega = 10$. (b) Function $R(t)$ for elastic secondary with no dissipation, with (i) $\omega = 5$ and (ii) $\omega = 10$. Weaker springs show more resonant states and these remain stable for a longer time.

In conservative cases ($\gamma = 0$), we do not have any attractor, but the system can still synchronize in several metastable resonances. The spring alone is enough for the secondary to interact with its orbit and temporarily store energy in the form of rotation and vibration. Eventually the energy will go back to the orbit and the system will return close to its initial state. In Fig. 4.4(a) we show how the energy is transferred from orbit to rotation and back. Stronger springs (higher ω) behave more like rigid bodies and hence produce fewer resonances. Weaker springs show a wide variety of synchronizations that can last from a few orbital periods to thousands of orbital periods. A very elastic secondary can easily synchronize in rarer resonances. For instance, we can have resonances with rotation velocity slower than the orbital velocity, or retrograde rotation:

with rotation in the opposite sense to the orbit. Fig. 4.4(b) compares the different resonances that are produced with different springs using $R(t)$ defined in Eq. (4.16). We can note how a more elastic secondary is more often synchronized and its resonances remain stable for longer times.

4.4 Approximate equations of motion

To calculate the approximate equations of motion we Taylor-expand the Lagrangian up to 4th order in $l/(2r)$:

$$\mathscr{L} = \frac{1}{2}\left[\dot{r}^2 + r^2\dot{\beta}^2 + \frac{\dot{l}^2}{4} + \frac{l^2}{4}\dot{\phi}^2\right] - \frac{1}{8}\omega^2(l-l_0)^2$$
$$+\frac{1}{r}\left[1 + \left(\frac{l}{2r}\right)^2 P_2(\cos\alpha) + \left(\frac{l}{2r}\right)^4 P_4(\cos\alpha)\right].$$

The Taylor-expanded equations of motion can be written as $\ddot{\vec{q}} = \ddot{\vec{q}}^{(0)} + \ddot{\vec{q}}^{(1)} + \ddot{\vec{q}}^{(2)} + \ldots$ where $\ddot{\vec{q}} = (\ddot{r}, \ddot{\beta}, \ddot{l}, \ddot{\phi})$ and

$$\ddot{\vec{q}}^{(0)} = \begin{pmatrix} r\dot{\beta}^2 - \dfrac{1}{r^2} \\ -2\dfrac{\dot{r}\dot{\beta}}{r} \\ l\dot{\phi}^2 - \omega^2(l-l_0) - 2\gamma\dot{l} \\ -2\dfrac{\dot{l}\dot{\phi}}{l} \end{pmatrix}, \tag{4.20}$$

$$\ddot{\vec{q}}^{(1)} = \begin{pmatrix} 0 \\ 0 \\ -\dfrac{l}{r^3}\left(1 - 3\cos^2\alpha\right) \\ -\dfrac{3}{2}\dfrac{1}{r^3}\sin 2\alpha \end{pmatrix}, \quad \ddot{\vec{q}}^{(2)} = \begin{pmatrix} \dfrac{3}{8}\dfrac{l^2}{r^4}\left(1 - 3\cos^2\alpha\right) \\ \dfrac{3}{8}\dfrac{l^2}{r^5}\sin 2\alpha \\ 0 \\ 0 \end{pmatrix}, \ldots \tag{4.21}$$

Another form of the Taylor-expanded equations of motion is

0th order	*1st order*	*2nd order*
$\ddot{r} = r\dot{\beta}^2 - \frac{1}{r^2}$		$+\frac{3}{8}\frac{l^2}{r^4}\left(1-3\cos^2\alpha\right)$
$\ddot{\beta} = -2\frac{\dot{r}\dot{\beta}}{r}$		$+\frac{3}{8}\frac{l^2}{r^5}\sin 2\alpha$
$\ddot{l} = l\dot{\phi}^2 - \omega^2(l-l_0) - 2\gamma\dot{l}$	$-\frac{l}{r^3}\left(1-3\cos^2\alpha\right)$	
$\ddot{\phi} = -2\frac{\dot{l}\dot{\phi}}{l}$	$-\frac{3}{2}\frac{1}{r^3}\sin 2\alpha$	

In general, the nth order approximation contains the nth power of l/r in the equations of $\ddot{r}$, $r\ddot{\beta}$, $\ddot{l}$ and $l\ddot{\phi}$ (accelerations).

In the 0th order approximation ($\ddot{\vec{q}} = \ddot{\vec{q}}^{(0)}$) the system of equations splits into two parts. The first pair of equations ($\ddot{r}, \ddot{\beta}$) form the equations of motion of the pure Keplerian problem and the second pair ($\ddot{l}, \ddot{\phi}$) describes the problem of two rotating point masses connected by a frictional spring.

It is worth emphasizing that in the 1st-order approximation ($\ddot{\vec{q}} = \ddot{\vec{q}}^{(0)} + \ddot{\vec{q}}^{(1)}$) the secondary has no feedback on the center-of-mass motion at all. That is why the first order approximation has important qualitative differences from the exact model: (i) The orbital elements are not changing; there is no circularization. (ii) It is a driven nonlinear system in which the drive is not changing in time. Depending on the orbital elements the attractor(s) can be simple or strange ones. Of course in the case of a strange attractor the dynamics of the secondary is permanently chaotic and in the case of simple attractors the dynamics can be either regular or transiently chaotic depending on the initial conditions. (iii) The orbit pumps energy into the secondary but the orbital energy remains constant. (iv) The total angular momentum is not constant. (v) The dimension of the phase space of this problem is only 5. In spite of these differences, it is important to consider this approximation because a couple of its features are reflected in the exact model.

We can also define approximations 1a and 2a. Approximation 1a is the 1st-order approximation without the term $-l/r^3\left(1-3\cos^2\alpha\right)$, i.e., an equation corresponding to rigid-body rotation of the secondary, provided $l = const$. In this approximation the action of the primary on the spring is neglected. Approximation 2a is the 2nd-order approximation without the term $3/8l^2/r^5\sin 2\alpha$ in the equation of $\ddot{\beta}$. The term kept in the equation of $\ddot{r}$ describes a central force perturbation proportional to $1/r^4$ provided l and α are constant. The force is then $3/8l^2/r^4\left(1-3\cos^2\alpha\right)$ and an analytic expression (Eq. (4.32)) exists for the apapsis precession.

In general, the trajectories calculated by the approximate and exact equations deviate from each other because of the chaoticity of the dynamics; in such cases we expect only the statistical behavior to be the same. On the other hand, if the motion is regular — as in a resonance — then the approximate equations are expected to be rather accurate.

4.5 The consequences of the energy condition

In this section, we show the typical response of the secondary to a change of orbital elements in resonant states.

The resonance we use for illustrative purposes is a $5:2$ resonance and the initial eccentricity is 0.1. By using the second-order approximate equations, the time average of the change of the center-of-mass energy can be written as

$$< \dot{E}_c >_q = \frac{1}{t_{i+q}-t_i} \int_{t_i}^{t_{i+q}} (\dot{r} q_1^{(2)} + r^2 \dot{\beta} q_2^{(2)}) dt =$$

$$\frac{1}{t_{i+q}-t_i} \frac{3}{8} \int_{t_i}^{t_{i+q}} \left(\frac{\dot{r}}{r^4} \left[l^2 \left(1 - 3\cos^2 \alpha \right) \right] + \frac{\dot{\beta}}{r^3} \left[l^2 \sin 2\alpha \right] \right) dt \tag{4.22}$$

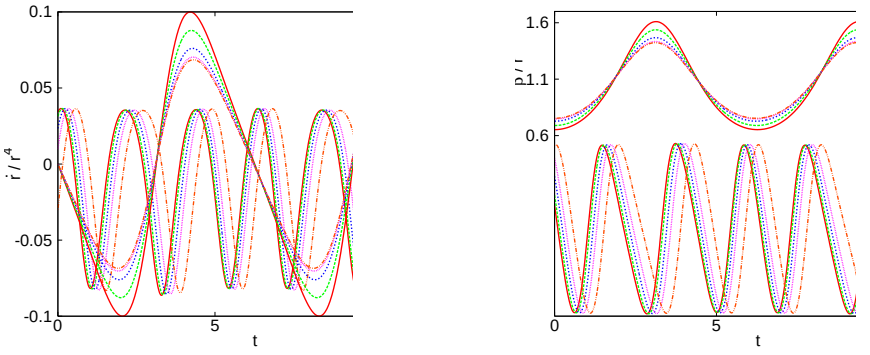

FIGURE 4.5: (a) Temporal change of the factors of the first term in the integral (4.22) over two orbital periods at different eccentricities. The secondary is at apapsis at $t = 0$. The colors correspond to the eccentricities: 0.9 (red), 0.8 (green), 0.7 (blue), 0.65 (purple) and 0.63 (orange). (b) Temporal change of the factors of the second term in the integral (4.22).

Fig. 4.5(a) [(b)] shows the first (the fraction) and the second (expression in square bracket) factors of the first [second] term in the integral over two orbital periods at different eccentricities. The amplitudes of the two first factors are directly proportional to

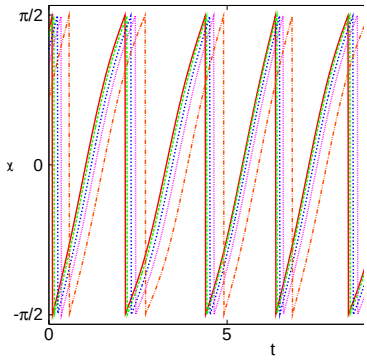

FIGURE 4.6: The shift of function $\alpha(t)$ with eccentricity. The colors mark the eccentricity values as in Fig. 4.5.

the eccentricity because the eccentricity and the change of the semi-major axis are relatively small. Because of the energy condition, the integral has to be constant. Therefore function $\alpha(t)$ has to change. Fig. 4.6 shows this $\alpha(t)$ function at $\varepsilon = 0.9$, 0.8, 0.7, 0.65, and 0.63. As the figure shows, the response of the secondary is a shift of function $\alpha(t)$. The shift becomes faster as the end of the resonance is approaching.

4.6 Temporal evolution of the orbital elements in the 1:1 resonant state

In order to obtain a continuous-time estimate of the orbital elements we give equations for

$$\dot{\varepsilon} = \frac{1}{\varepsilon}(\dot{E}_c N_1^2 + 2E_c N_1 \dot{N}_1), \tag{4.23}$$

$$\dot{a} = \frac{1}{2}\frac{1}{E_c^2}\dot{E}_c = 2a^2\dot{E}_c. \tag{4.24}$$

These equations appear in several models which treat the secondary as a spatially extended object, see e.g. [38]. The point is that $\dot{E}_c$ and $\dot{N}_1$ cannot be expressed by ε and a only, and the set of equations is thus not closed. The authors typically use special approximate formulas for $\dot{E}_c$ and $\dot{N}_1$ obtain a closure. We are not forced to do so since the numerical values of these quantities easily follow from (4.2)-(4.5) and (4.7), (4.8). In fact we consider (4.23), (4.24) only as diagnostic equations investigated along with the numerical solution of our model.

For later purposes we also write down an equation for $\beta_{apapsis}$, used in the same diagnostic sense. By taking the time derivative of (4.14), (4.13) and using (4.7) and (4.12)

we find:

$$\dot{\beta}_{apapsis} = \dot{\beta} + \frac{\varepsilon\left(3r^2\dot{r}\dot{\beta}^2 + 2r^3\dot{\beta}\ddot{\beta}\right) + \dot{\varepsilon}\left(1 - r^3\dot{\beta}^2\right)}{\dot{r}\varepsilon\sqrt{a(1-\varepsilon^2)}}. \tag{4.25}$$

The leading order behavior of these quantities follows from the second-order approximate equations. Substituting

$$\dot{N}_1 = 2r\dot{r}\dot{\beta} + r^2\ddot{\beta} \approx r^2 q_2^{(2)}, \tag{4.26}$$

$$\dot{E}_c = \dot{r}\left(\ddot{r} + \frac{1}{r^2}\right) + r\dot{r}\dot{\beta}^2 + r^2\dot{\beta}\ddot{\beta} \approx \dot{r}q_1^{(2)} + r^2\dot{\beta}q_2^{(2)}, \tag{4.27}$$

into (4.23) and (4.24), we obtain

$$\dot{\varepsilon} = \frac{1}{\varepsilon}\left[\left(\dot{r}q_1^{(2)} + r\dot{\beta}^2 q_2^{(2)}\right)N_1^2 + 2E_c N_1 r^2 q_2^{(2)}\right], \tag{4.28}$$

$$\dot{a} = 2a^2(\dot{r}q_1^{(2)} + r^2\dot{\beta}q_2^{(2)}). \tag{4.29}$$

In a similar way, one finds from (4.25)

$$\dot{\beta}_{apapsis} = \frac{2r^3\dot{\beta}\varepsilon q_2^{(2)} - \left(r^3\dot{\beta}^2 - 1\right)\dot{\varepsilon}}{\dot{r}\varepsilon\sqrt{a(1-\varepsilon^2)}}. \tag{4.30}$$

4.6.1 Apapsis precession

The apapsis precession $\Delta\beta$ is obtained by multiplying $\dot{\beta}_{apapsis}$ by the instantaneous period $T(t) = 2\pi a(t)^{3/2}$:

$$\Delta\beta(t) = 2\pi\sqrt{a^3(t)}\dot{\beta}_{apapsis}(t). \tag{4.31}$$

This equation provides the instantaneous tendency for producing a given apapsis precession. This can, in certain phases of the motion, be of opposite sign than after a full period , i.e., than the average of $\Delta\beta(t)$ over a period. A well-known result [42] for $\Delta\beta$ in the presence of a dimensionless perturbative force of the type $-\kappa/r^4$, $\kappa \ll 1$ yields

$$\Delta\beta_{pert}(t) = 2\pi\frac{\kappa(t)}{N_1^4(t)} \tag{4.32}$$

where $\kappa(t) = \frac{3}{8}l^2(t)\left(1 - 3\cos^2\alpha(t)\right)$, under the assumption that $\kappa(t)$ changes slowly.

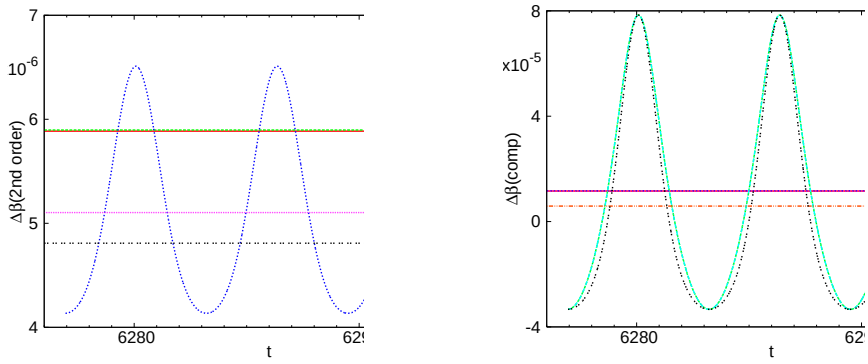

FIGURE 4.7: (a) Comparison of the different methods for the calculation of the apapsis precession in the case of a 1:1 resonance in approximation 2a: numerically measured $\Delta\beta$ (red), average of $\Delta\beta(t)$ from Eq. (4.31) (green), $\Delta\beta_{pert}(t)$ from Eq. (4.32) (blue), average of $\Delta\beta_{pert}(t)$ (violet), $\Delta\beta_{naive}$ from Eq. (4.33) (black). Parameters and initial conditions: $\omega = 10$, $\gamma = 1$, $l_0 = 10^{-3}$, $\varepsilon_0 = 0.1$, $\phi(0) = 0$, $\dot{\phi}(0) = 5$. (b) Comparison of the apapsis precession obtained by means of the different approximate equations. The red (measured exact) and the dark blue dashed (exact $\Delta\beta(t)$ averaged) line segments are covered by the purple one (measured $\Delta\beta$ in 2nd order), the green (exact $\Delta\beta(t)$) is covered by the light blue one (2nd order $\Delta\beta(t)$). Parameters and initial conditions: $\omega = 10$, $\gamma = 1$, $l_0 = 10^{-3}$, $\varepsilon_0 = 0.1$, $\phi(0) = 0$, $\dot{\phi}(0) = 5$.

In a time independent naïve approximation when $\kappa(t)$ is considered to be constant with $\alpha \approx 0$ and $l = l_0$, $N_1 = N$

$$\Delta\beta_{naive} = \frac{3\pi}{2}\frac{l_0^2}{N^4}. \tag{4.33}$$

In order to test the accuracy of the naïve and the perturbative approximations of the apapsis precession we compare the numerical results in the case of the simplest, 1:1 resonance. Fig. 4.7(a) shows $\Delta\beta_{naive}$ from Eq. (4.33), the measured $\Delta\beta$ (measurement has been made after a period but the value is represented by a continuous line), $\Delta\beta_{pert}(t)$ from Eq. (4.32), its average, and the time average of $\Delta\beta(t)$ from Eq. (4.31) all evaluated in approximation 2a. Our conclusion is that the naïve and the perturbative approximations can only estimate the magnitude of the apapsis precession; they are not suitable to give the exact value. The value of the time-averaged $\Delta\beta(t)$ is practically the same as that of the measured $\Delta\beta$. The difference between the averages of $\Delta\beta(t)$ and $\Delta\beta_{pert}(t)$ may be due to the fact that κ is also oscillating with an amplitude which is about one fifth of its average value. Therefore, the perturbative result based on the slow variation of κ is an educated guess only.

Fig. 4.7(b) shows that the apapsis precession, Eq. (4.31), evaluated with the 2nd order approximation and the exact equations coincide. This means that the equations of the 2nd order approximation are sufficient for calculating the apapsis precession to high accuracy. The figure also shows the function $\Delta\beta(t)$ and the numerically measured

apapsis precession in approximation 2a. The result is about one half of the measured apapsis precession of the 2nd order approximation and of the exact simulation. This implies that the contribution of the perturbation $3/8\, l^2/r^4 \sin 2\alpha$ in the equation of $\ddot{\beta}$ to the apapsis precession is practically as important as the well known central force contribution, Eq. (4.32), of approximation 2a.

Here we have concentrated on the case of the 1:1 resonance on time scales when the system is still far away from the circularized attractor. Since the interesting time dependencies all die out in the long-time limit, the approximate equations are expected to work even better for later times. The behavior of the approximation scheme around other resonances is also similar. Altogether, the 2nd-order approximate equations seem to provide a rather accurate description of the entire dynamics, provided that the resonant state under investigation is the same as that predicted by the exact equation. The observation that the approximate equations lead in some cases to different resonances or 'transient attractors' on intermediate time scales appears to be a consequence of the fact that the dynamics between resonances is chaotic and the errors attributable to using a perturbation expansion become drastically amplified.

We can study the influence that the different parameters – $\gamma, \omega, l_0, \varepsilon$ – have on the apapsis precession - $\Delta\beta_{apapsis}$. Looking at Eq. (4.30), we can see that $\Delta\beta_{apapsis}$ does not depend on γ directly. Numerical results indicate that an indirect dependence cannot be found either for a wide range of γ ($\gamma < 2$). $\dot{\beta}_{apapsis}$ (4.30) depends on $q_1^{(2)}$ (through $\dot{\varepsilon}$) and $q_2^{(2)}$, and the l-dependence of both terms is quadratic, so $\dot{\beta}_{apapsis} \sim l^2$. Using the approximation $l - l_0 << l$ we expect that the l_0 and ω dependencies can be written as

$$\Delta\beta_{apapsis} = c_1 \left(\frac{l_0}{1 - c_2/\omega^2} \right)^2, \tag{4.34}$$

where c_1 and c_2 are fitting parameters. Numerical fits confirm this conjecture. The l_0-dependence is perfectly quadratic and Fig. 4.8(a) shows that expression (4.34) as a function of ω is perfectly consistent with the measured data. Fig. 4.8(b) shows that the eccentricity dependence is basically also quadratic, but as $\varepsilon \to 0$, the apapsis precession seems to converge to a nonzero value.

4.7 Comparison of approximations in chaotic cases

To produce Fig. 4.9(a), the exact equations of motion have been integrated with 35 different initial conditions and the time averages of the angular velocity have been calculated in every period. The initial eccentricities of all 35 integrations were the same ($\varepsilon = 0.1$). Fig. 4.9(a) shows the average of the angular velocities versus time. There is a plateau at the end of the curve, since all 35 cases are in resonance. The height of the plateau is 1 implying that all the cases are in a 1:1 resonance. We integrated

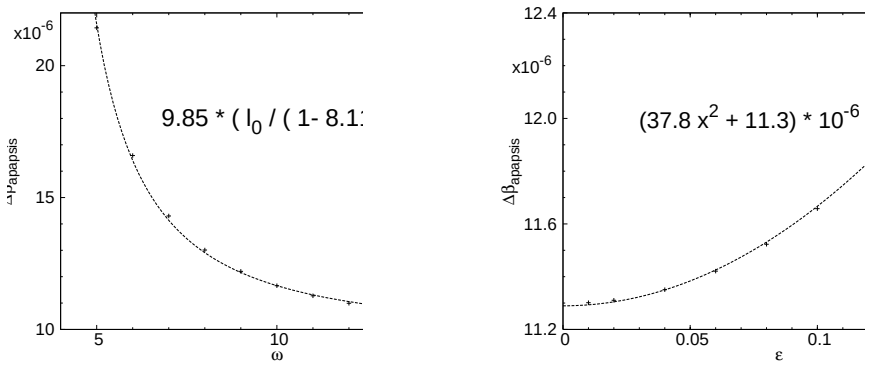

FIGURE 4.8: Numerical data (dots) and fits (lines) for the apapsis precession as a function of spring frequency (a) and eccentricity (b). (a) Parameters are $\gamma = 1$, $l_0 = 10^{-3}$; $\varepsilon_0 = 0.05$, and the fitted parameters of (4.34) are $c_1 = 9.85$, $c_2 = 8.11$. (b) Parameters are $\omega = 10$, $\gamma = 1$, $l_0 = 10^{-3}$. The form of the fitted function is $a\varepsilon^2 + b$. The result of the fit is $a = 3.78 \cdot 10^{-5}$, $b = 1.13 \cdot 10^{-5}$

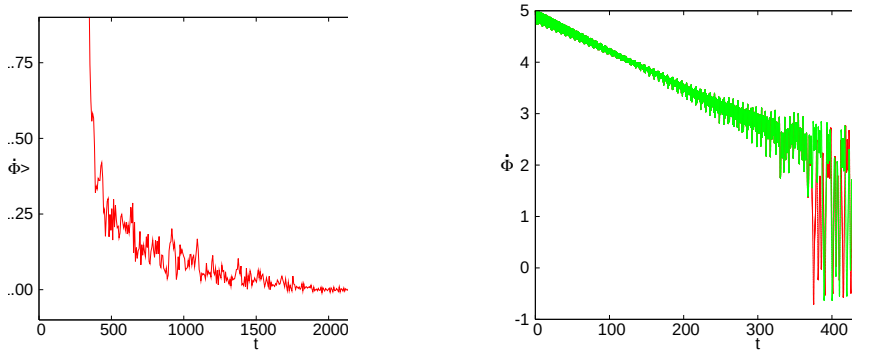

FIGURE 4.9: (a) Average angular velocity with the exact equations. Initial conditions: $\varepsilon_0 = 0.1$ and $(\phi_0, \dot{\phi}_0)$ is an element of the grid determined by the values $\phi_0 \in \{0,1,2,3,4,5,6\}$, $\dot{\phi}_0 \in \{4.98, 4.99, 5.0, 5.01, 5.02\}$. We used this set of initial conditions for every averaged plot in this chapter. In the chaotic case the only reliable information is related to averages. (b) $\dot{\phi}(t)$ in the 2th order approximation (red) and with the exact (green) equations of motion. Parameters and initial conditions: $\omega = 10$, $\gamma = 1$, $l_0 = 10^{-3}$; $\varepsilon_0 = 0.1$, $\phi(0) = 0$, $\dot{\phi}(0) = 5$.

the exact and the 2nd-order equations of motion with the same initial conditions. Angular velocity $\dot{\phi}$ versus time can be seen in Fig. 4.9(b). Here and even in the case of the highest-order approximation the trajectories deviate from each other in the transient chaotic regime ($t > 300$). Based on a study of a couple of similar cases we conclude that the 2nd-order (and higher-order) approximations have the same characteristic features as the exact equations of motion.

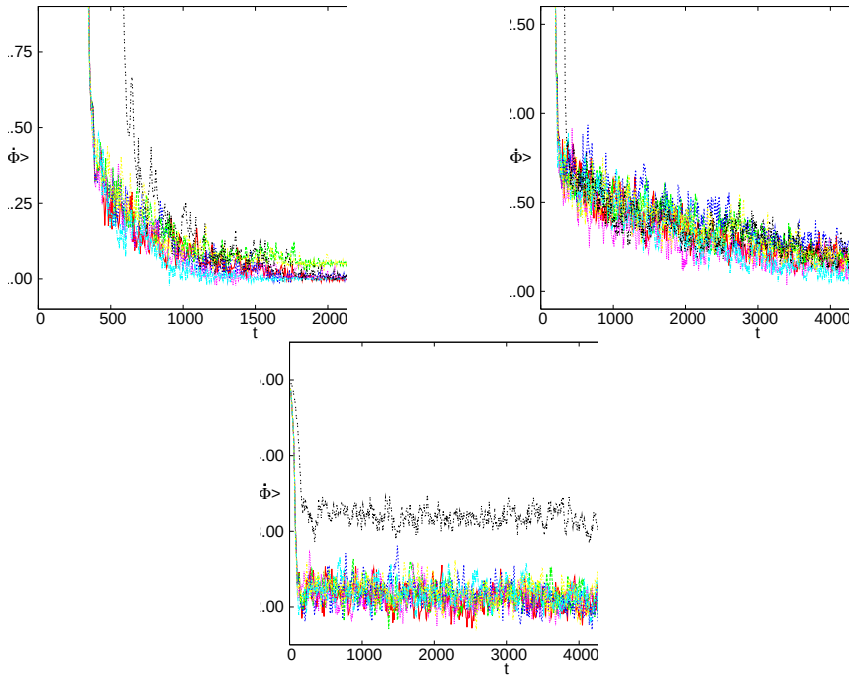

FIGURE 4.10: Comparison of the average behavior of the different approximate equations. Initial eccentricity is (a) $\varepsilon_0 = 0.1$; (b) $\varepsilon_0 = 0.2$; (c) $\varepsilon_0 = 0.3$.

We have also studied the statistical behavior of the different approximations. The same type of plot as Fig. 4.9(a) has been made to all orders of the approximations in Fig. 4.10(a). We conclude that any approximations other than 1a exhibit the same statistical behavior as the exact case. From the graphs the characteristic time, τ_1, needed to reach a 1:1 resonance can be estimated. This state is not yet the circularized attractor since $\varepsilon \approx \varepsilon_0$ after such short period of time. It takes typically a much longer time — denoted by τ in [34] — for the attractor, where $\varepsilon = 0$, to be reached; in this example $\tau_1 \approx 2000$ and $\tau \approx 10^6$. The plateau of the green, 4th-order curve is slightly higher than 1. The reason is that one of the 4th-order cases is in a 5:2 resonance and not in 1:1. Among the 1st-order simulations there were two in a 5:2 resonance, which is why the yellow curve is higher than the green one. It is hardly observable but the dark blue, 3rd-order curve is also higher than 1; this is owing to the presence of a 5:4 resonance.

Fig. 4.10(b) and (c) show a comparison of the exact and the approximate cases with different initial eccentricities. Based on these, we conclude that the higher the eccentricity the greater the time τ_1. In Fig. 4.10(c) the asymptotic value is not 1, which suggests that a 1:1 resonance has not yet been reached by the end of the integration; the curve is not smooth because most of the trajectories are not in resonance.

Fig. 4.11 shows the time dependence of the eccentricity $\varepsilon(t)$ in the different approximate equations. In all cases a 1:1 resonance has been reached by $t \approx 3000$. In the first order approximation there is no feedback of the secondary on the Keplerian problem, therefore $\varepsilon(t) = \varepsilon_0 = const$. The asymptotic slope of the other curves show the rate of decrease of eccentricity. These rates are the same in all cases with the exception of approximation 2a which indicates that the contribution of the term $3/8\, l^2/r^5 \sin 2\alpha$ missing from the equation for $\ddot{\beta}$ is important.

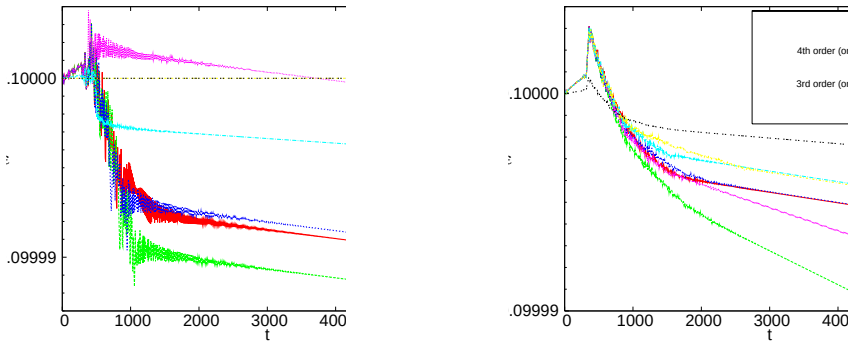

FIGURE 4.11: (a) Comparison of eccentricities with the different approximate equations. Parameters and initial conditions: $\omega = 10$, $\gamma = 1$, $l_0 = 10^{-3}$; $\varepsilon_0 = 0.1$, $\phi(0) = 0$, $\dot{\phi}(0) = 5$. (b) Comparison of the averaged eccentricities with the different approximate equations. Parameters and initial conditions: $\omega = 10$, $\gamma = 1$, $l_0 = 10^{-3}$; $\varepsilon_0 = 0.1$.

Fig. 4.11(b) shows the eccentricity averaged over 35 different initial conditions in the different approximate equations. It is a general observation that in resonances different from 1:1 the eccentricity decays much faster. This is the reason why in cases in which there are also other resonances than 1:1 in the ensemble (the 3rd and 4th order) the averaged eccentricities decrease faster. If we average only the 1:1 resonance cases then we get the light and the dark blue curves. As expected, the curves of the 2nd and 3rd order are close to each other, and close to the curves of the 4th order and to the exact numerical solution which practically coincide. Fig. 4.11(b) indicates that in exceptional cases even the 4th-order approximation can lead to a resonance — a 'transient attractor' — different from the exact one. The good agreement between the approximate and exact equations only holds under the condition that the same resonance has been reached.

4.8 Discussion

Spin-orbit resonances between a large primary body and a smaller secondary body are generally studied using models designed for quantitative analysis of a specific instance or a particular part of the problem [19, 20, 23–27, 33]. The complexity of these models tends to obscure the fundamental physical principles involved in this interaction. We have instead taken a qualitative dynamical-systems approach, using a minimalistic model that takes into account only the essential ingredients of tidal deformation and dissipation in the secondary body. Despite its simplicity, the model can account for both synchronization into the 1:1 spin-orbit resonance and the circularization of the orbit as the only true asymptotic attractors. Apart from its applicability to tidal synchronization and orbit circularization of celestial bodies, our model is also relevant to the problem of the dynamics of tethered satellites, which has recently provoked much interest and a number of space missions [43].

One interesting open question is whether a pseudo-energy — or energy-like — approach would provide new insight into the problem. In this case we have completely defined the gravitational and mechanical energies — the center of mass plus rotation and vibration of the secondary — and thus the dissipated energy can be obtained simply by subtraction from the initial energy; the same is true for the evolution between two arbitrary states. As the dissipation is strictly passive the total energy is necessary a decaying function, reaching a constant value only in a situation in which the dissipation term vanishes along the trajectory. In the approach of Sarasola et al. [44], energy dissipation is associated with a local change in phase space volume and on this basis they define a partial differential equation that an energy-like function must satisfy. The same depends on a part of the decomposition of the vector velocity field; the divergence free or rotational part in contrast with the part that carries the whole divergence. Once H is obtained we can calculate the energy derivative along a trajectory of the system which is due to the part carrying the divergence of the vector field. Probably this is the unique new information that can be obtained in our case: an analytical expression instead of the indirect calculation by subtraction of the mechanical plus gravitational energy. Nonetheless the pseudo-energy approach is of interest and we intend to pursue it in future work.

The main conclusions that may be drawn from the present investigations are: The 1:1 resonance is the only stable attractor. Dissipation drives the system towards this synchronization and circularizes the orbit. All other resonances are metastable, or transient attractors, and dissipate energy at a faster pace, and the approach towards the circular orbit is also faster. Conservative satellites can also produce resonances, although in this case there is no stable attractor and all resonances are relatively short. Isolating the dominant interactions between the degrees of freedom in terms of a Taylor expansion allows us to to study them separately. In general, the second-order approximation is sufficient to reproduce the typical behavior of the complete model, as long as we are in

the 1:1 resonance. This has been studied for apapsis precession, chaotic regimes and eccentricity evolution.

Finally, we summarize features of our model which are expected to remain valid in more general cases as well. Even if the expression of $< \dot{E} >_q$ can, in general, be quite complex, the energy condition (4.19) for resonant states holds in any case. The mechanism of the response of the secondary to the change of the orbital elements should remain similar as in our model. Of course, we have to use the general formula (4.22) where $q_1^{(2)}$ and $q_2^{(2)}$ can be rather complicated.

Part II

Ice

Chapter 5

Ice: Introduction

Ice is one of the most abundant and most studied solid crystalline material. It is of interest to geophysicists and glaciologists, concerned with the large ice masses on the surface of the Earth. There are meteorologists and cloud physicists concerned with the role of ice in our weather. There are chemists who see ice as the simplest example of a hydrogen-bonded solid. There are crystallographers concerned with the structural disorder that is specially characteristic of ice, and who are also concerned with the many different phases into which H_2O molecules can crystallize. There are also physicists concerned with electrical properties, lattice defects, lattice vibrations and the unusual properties of the surface.

The very existence of life on the planet Earth and the temperature stability of its atmosphere depend on the fact that the three phases of water (ice, liquid and vapor) are present in abundance. Most of the surface of the Earth is covered with water and, depending on the time of the year, some 5% of that water might be in liquid of solid state. The ice hence acts as a temperature balancing mechanism that helps to maintain the equlibirium between the radiation received from the Sun and that reflected or reradiated from the Earth. The resulting global average temperature is highly sensitive to the amount of snow, ice and cloud cover. Our environment is thus critically dependent on the properties of ice both in the meteorology of clouds and in the rheology of ice sheets. At earlier times in geological history ice has covered up to 30% of the land area and its motion has carved many features of the global landscape.

Water has always awakened scientific curiosity through its unususal properties. It is the only chemical compound that can be found naturally on Earth in the solid, liquid and vapor phases. When water is cooled below 4 ^{o}C it expands and becomes more compressible, the contratry situation to what happens to most liquids. Its dielectric constant in the normal liquid range is unusually large, and its melting and boiling temperatures are uncommonly high for a non-metallic hydride. In the crystalline state, water has fourteen known polymorphs, of which ten (ices II, III, V, VI, VII, VIII, X, XI, XIV and

ordinary hexagonal ice, Ih) are stable over a certain range of temperature and pressure, and four are metastable (ices IV, IX, XII and cubic ice, Ic). In 2009, ice XV was found at extremely high pressures and -143 ^{o}C [45]. When liquid water is cooled below the freezing point without crystallizing, we say it is in a 'supercooled' state. In that situation the unusual physical properties of water are more pronounced, and it becomes clear that the anomalies of liquid water are remnants of its low-temperature properties. It is therefore useful to study water in the supercooled range in order to fully understand its properties in ambient conditions.

Amorphous ice in its different forms has been the subject of intense research in the recent years. When cooled fast enough to avoid crystallization, water, like other liquids, vitrifies. Unlike most other substances, though, glassy water can apparently exist in at least two distinct forms, which may be separated by a first-order phase transition [46]. One of the most important ideas of the past two decades in this field is the realization that supercooled and glassy water are intimately related, and that fundamental understanding of metastable water must encompass both its liquid and vitreous states [47].

Our interest in ice came from the possibility to study the mesoscale morphology of amorphous ice using Environmental Scanning Electron Microscopy (ESEM). We were interested in studying the dynamics involved in the morphology of ice in extreme conditions and the appearance of self-organized patterns.

The Crystalline Phases

The phase diagram of water is complex, having a number of triple points and one or possibly two critical points. At ambient temperature and pressure (marked x on Figure 5.1) water is liquid, but it becomes solid (ice) if its temperature is lowered below 273 K and gaseous (vapor) if its temperature is raised above 373 K, at the same pressure.

The solid phase of water found on Earth can present itself in a variety of forms, from snowflakes to icebergs, with very different bulk properties, but at the microscopic level they are all composed of the same polymorph, hexagonal ice (ice Ih, see Figure 5.2) which is the stable phase at the temperatures and pressures of our biosphere. However, beyond the range of natural terrestrial conditions, ice can crystallize as many other polymorphs, and all of these are referred to as forms of 'ice'. Most of these phases are produced by the application of high pressures, which result in denser packing of molecules than in ice Ih.

The first high-pressure phases were discovered almost a century ago by Tammann (1900) in a program to study the pressure-volume-temperature relationships of various materials, and he named these phases 'ice II' and 'ice III'. The rest of the phases were labeled with the Roman numerals in the approximate order in which they were

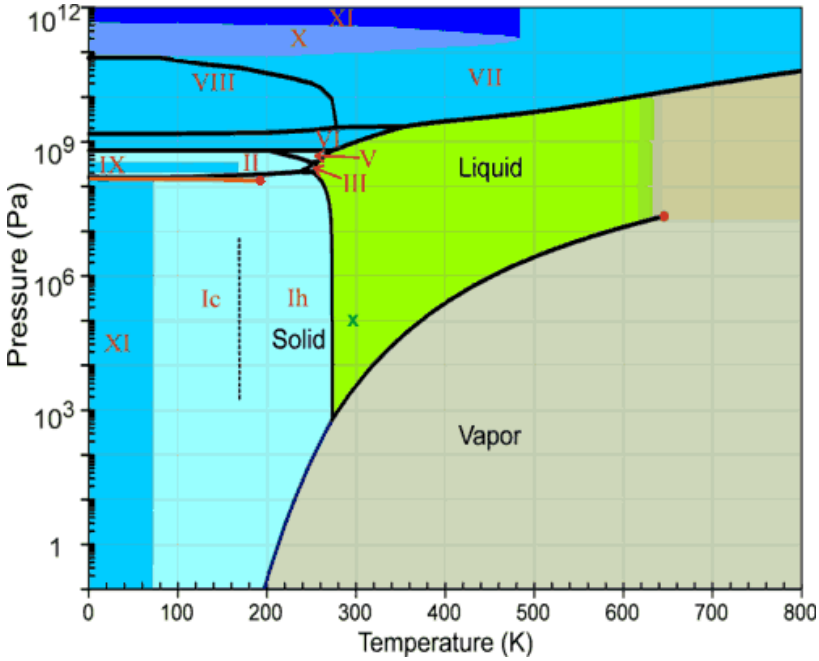

FIGURE 5.1: The phase diagram of water [1].

produced experimentally, with the result that the numbers indicate nothing about the structures or the relations of the phases to one another.

All the crystalline phases of ice involve the water molecules being hydrogen bonded to four neighboring water molecules. In all cases the two hydrogen atoms are equivalent, with water molecules retaining their symmetry, and they all obey the 'ice' rules: two hydrogen atoms near each oxygen, one hydrogen atom on each O–O bond (see Figure 5.2). The H-O-H angle in the ice phases is expected to be a little less than the tetrahedral angle (109.47°), at about 107°.

Crystalline Morphologies

As mentioned above, the same crystalline structure can lead to many different ice morphologies. For this reason the formation of ice crystals from water vapor is an excellent case to study crystal growth dynamics and pattern formation during solidification. It has awakened a great curiosity and has been a source of inspiration for many scientific studies, specially in the case of snow crystals (snowflakes) [48–50].

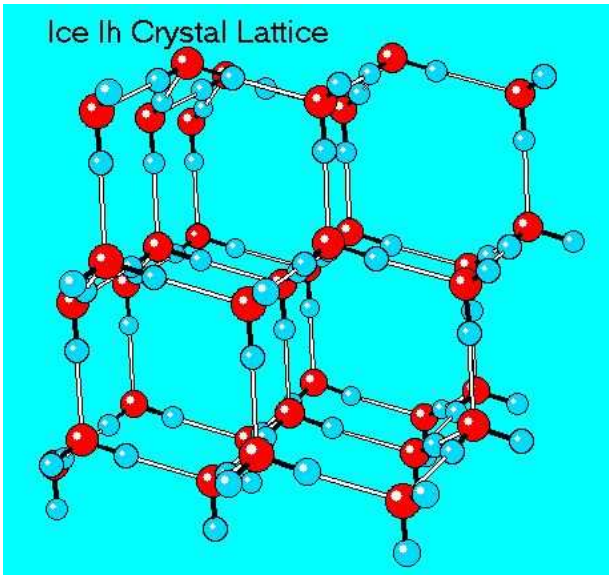

FIGURE 5.2: The hexagonal lattice of ice Ih [2].

The apparently infinite variety of snow crystals found in nature prompted the physicist Nakaya to perform the first thorough laboratory study of snow crystal growth in the 1930s [51]. Nakaya observed the different growth morphologies that appeared at different temperatures and supersaturations and combined these observations into what is called a *snow crystal morphology diagram*, shown in Figure 5.3. This diagram refers to snow crystals growing in air at a pressure near 1 atm, so applies to natural snow crystals. His observations reveal a surprisingly complex dependence of crystal morphology on temperature and supersaturation. Just below freezing, at temperatures near T = $-2°$C, the growth is plate-like, with thick plates at lower supersaturations, thinner plates at intermediate supersaturations, and plate-like dendritic structures at high supersaturations. For temperatures near T = $-5°$C, the growth is columnar, with stout columns at the lower supersaturations, more slender, often hollow columns at intermediate supersaturations, and clusters of thin, needle-like crystals at higher supersaturations. Colder still, near T = $-15°$C, the growth again becomes plate-like, and again one sees increasing structure with increasing supersaturation. Finally, at the lowest temperatures the growth becomes a mixture of thick plates at low supersaturations and columns at higher supersaturations.

The physical explanation for this phenomenon is rather complex and some aspects are not yet understood at a qualitative level. Its dynamics are dominated by attachment kinetics in combination with two transport effects: particle diffusion, which carries

molecules to the growing crystal, and heat diffusion, which removes latent heat generated by solidification. The result is a competition between faceted and branched growth. When the growth is not very strongly limited by particle diffusion (low supersaturation and small crystal size), the morphology of the crystal will be an hexagonal prism. When the supersaturation is high or the crystal has become large enough, particle diffusion begins to dominate the growth dynamics and at some point branching occurs. When the crystal morphology exhibits numerous branches and side-branches, then we say the growth is dendritic, which literally means 'tree-like'.

However, no information has been found about the morphology of ice at very low temperatures and pressures. One of the aims of this work is to explore this point.

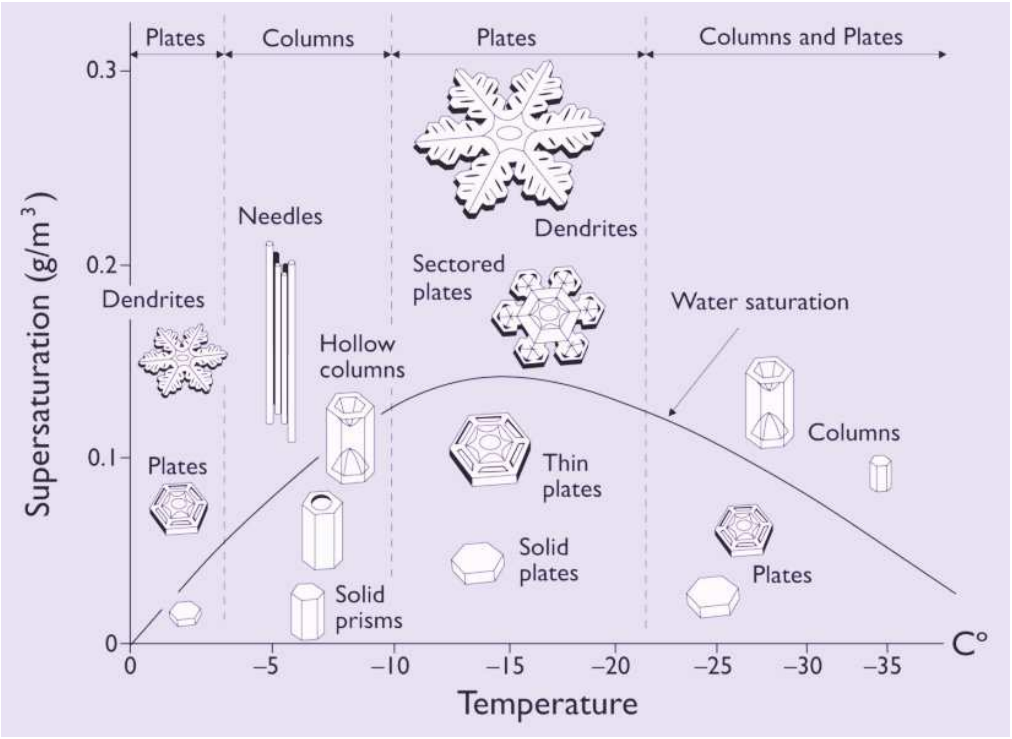

FIGURE 5.3: The snow crystal morphology diagram, showing different types of snow crystals that grow in air at atmospheric pressure, as a function of temperature and water vapor supersaturation [52].

The Amorphous Phases

Water, like any other liquid, can be vitrified when cooled sufficiently fast as to avoid crystallization. Unlike other substances, however, water can apparently form at least two distinct forms of glass, known as low-density and high-density amorphous ice (LDA and HDA, respectively). The properties of LDA and HDA, and the nature of the transition between them, are key to understanding the thermodynamics of supercooled and stable liquid water [53]. Recently, very-high-density amorphous ice (VHDA) has been proposed as a third distinct form of glassy water [54].

Low-density amorphous ice (LDA)

The direct vitrification of liquid water was first achieved by Brüggeller and Mayer [55] by ejecting a pressurized emulsion of μm-size water droplets in n-heptane onto liquid ethane at 90 K. These authors subsequently vitrified pure (non-emulsified) water by projecting a high-speed thin jet into liquid propane at 80 K [56]. Using rapid cooling of small aerosol water droplets ($3\ \mu\text{m} \leq \text{d} \leq 25\ \mu\text{m}$) onto a metal cryoplate ($15\ \text{K} \leq \text{T} \leq 77\ \text{K}$), Mayer was able to vitrify liquid water without resorting to a liquid cryomedium. Vitrification of water by rapid cooling of the liquid is referred to as hyper-quenching, since it requires cooling rates of about 106 K s^{-1}; the resulting material is called hyper-quenched glassy water (HGW).

But as well as production from the liquid or solid phases, amorphous ice can also be obtained from condensation of the gas phase. In fact, amorphous ice was first found in vapor deposition experiments. In 1935 Burton and Oliver [57] found that an amorphous solid was formed when water vapor at low pressure was deposited on a sufficiently cold substrate. This ice was later termed amorphous solid water (ASW). A large body of experimental work has since confirmed this observation [58]. Typically, thin films of vapor-deposited ASW are grown on single-crystal substrates (e.g., Au(111), Ru(001), Pt(111)) at deposition rates between 0.1 and 7 μm h^{-1} and temperatures between 10 and 130 K, using molecular beams [59].

High-density amorphous ice (HDA)

As first shown by Mishima and co-workers in 1984, application of pressure to ice Ih at low temperature leads to the formation of an amorphous solid, which has come to be known as high-density amorphous ice (HDA) [61]. The idea behind the original experiment was to cross the metastable extrapolation of the hexagonal ice melting curve. Because this locus has negative slope in the (P, T) plane, it (or its metastable extrapolation) will be crossed upon compression of the stable solid phase. By choosing a temperature, 77 K, low enough to thwart kinetically the transformation into stable ice IX, and also

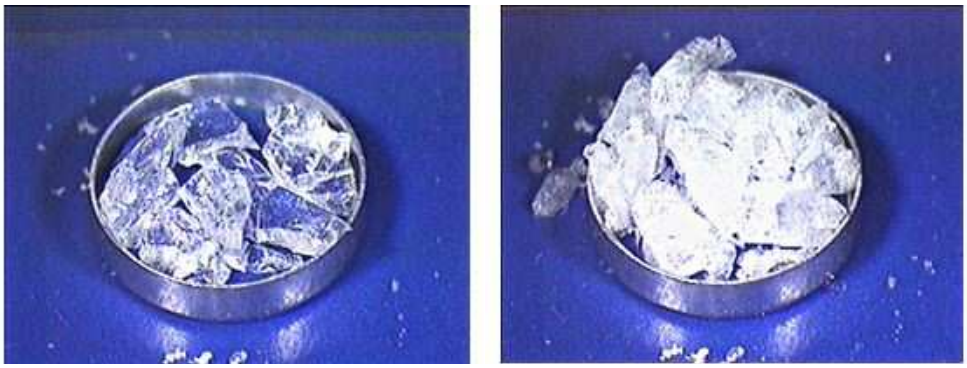

FIGURE 5.4: Transition between the amorphous phases of ice. High Density Amorphous HDA (left) and Low Density Amorphous LDA (right) at ambient pressure [60].

such that any liquid phase would be below its glass transition, Mishima succeeded in amorphizing ice Ih through a process that started at 10 kbar and was completed by 15 kbar.

Upon decompression to atmospheric pressure, HDA at 77 K remains a dense solid (1.17 g cm^{-3} [62]), which transforms irreversibly to LDA upon heating to about 120 K (Figure 5.4). Upon compressing LDA at 77 K, Mishima observed an abrupt transition to HDA, accompanied by a 22% volume decrease, at 6 kbar. The structure of HDA decompressed to ambient pressure has been studied by means of X-ray diffraction [63] and neutron scattering [64–67].

HDA can also be produced by vapor deposition. It has been shown that ASW differs when deposited at higher or lower temperatures. For surface temperatures below 30 K, a higher density ice is formed, while at higher temperatures ($\sim$30–130 K) a low density amorphous ice is deposited [46, 68]. These ices are similar to the high- and low-density amorphous ices produced in solid and liquid state transformations, and are considered by some to be LDA and HDA [68, 69], while others see essential differences [70].

The transition between LDA and HDA

In 1985 Mishima and co-workers compressed LDA (formed by heating decompressed HDA at atmospheric pressure above 130 K, and then rapidly cooling to 77 K) and observed a sharp transition at 6 ± 0.5 kbar [62]. The transition entailed an about 22% volume decrease, and did not reverse when the pressure was decreased. By increasing the temperature to about 135 K, Mishima showed that the transition can be reversed [71]. The sharpness and reversibility of the transformation are consistent with a first-order transition between LDA and HDA.

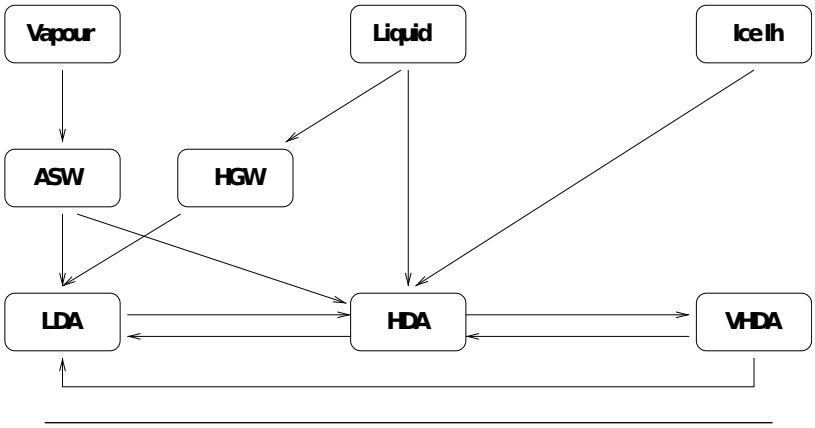

FIGURE 5.5: Transitions producing amorphous ices.

The progress of the LDA–HDA transition has been followed visually [72], as well as by Raman spectroscopy [73] and using neutron diffraction [74]. The observation of a well-defined propagating phase boundary [73] supports the notion of a first-order phase transition. In contrast, a recent neutron and X-ray diffraction investigation (at atmospheric pressure) of structural changes in recovered HDA upon annealing has been interpreted as implying that the transition to LDA proceeds through a series of metastable intermediates [75]. However, the temperatures in that study (95, 100, 105 and 110 K) were all below 135 K, the thermal level required for the transition to be reversible and hence the observations are instead fully consistent with incomplete structural relaxation upon annealing.

Very-high-density amorphous ice (VHDA)

Recently Loerting *et al.* [76] reported that an apparently distinct form of high-density amorphous ice can be recovered at 77 K and atmospheric pressure, following isobaric heating of HDA under pressure. They called this material very-high-density amorphous ice (VHDA). Specifically, they heated HDA at 11 kbar from 77 K up to 165 K, and at 19 kbar from 77 K to 177 K. The resulting material relaxed at atmospheric pressure and 77 K to the same structure, as characterized by X-ray diffraction and Raman spectroscopy, and had a density of 1.25 g cm^{-3}, that is to say $\sim$9% higher than recovered HDA. Both the Raman spectrum and the x-ray diffraction pattern of VHDA differ from those of HDA.

The detailed structure of VHDA has been determined by Finney *et al.* via neutron diffraction with isotope substitution [77], with site-site radial distribution functions and spatial density distributions calculated by the empirical potential structure refinement

Monte Carlo procedure. The OH and HH radial distribution functions of recovered VHDA were found to be very similar to those of HDA, but significant differences were found in the respective OO distributions. The first OH coordination number for VHDA is 2, indicating that each water molecule participates in two hydrogen bonds, and hence that VHDA is a fully coordinated hydrogen bond network. Integration of the area under the OO first peak out to the first minimum in HDA neuron diffraction reveals that the nearest neighbors increases from 5 in HDA to 6 in VHDA [77]. Despite these differences, Klotz *et al.* [78] noted that the structure of recovered VHDA is very similar to that of HDA at about 7 kbar.

Loerting *et al.* [76] found that the volume decreased continuously during isobaric heating of HDA. However, the recovered samples at 77 K and 1 bar showed just one distinct structure. They interpreted this observation as implying that pressurized amorphous ice with a continuum of densities relaxes upon depressurization to a new form of amorphous water, VHDA. Whether this recovered state is indeed a new form of amorphous water, or just a kinetically trapped structure, is not known at present.

Amorphous ice morphology

The physical properties of amorphous ice have been studied using many experimental methods ever since Burton and Oliver first identified amorphous solid water by means of X-ray diffraction [57]. It has been found that the morphology and physical properties of ASW films depend sensitively on the growth angle, thermal history of the film and substrate characteristics [79–82].

However, the microscopic morphology of amorphous ices has not been studied thoroughly owing to the intrinsic limitations of the experimental conditions in which such ices are produced. In 1987 Laufer et al. presented optical microscopy images of an ice film grown by ballistic water deposition onto a cold surface somewhere between 20–100 K [83]. The resulting morphology was described as smooth ice needles with no side branches, as opposed to the dendritic structure of hexagonal ice (see Fig. 5.6).

In 1991 Mishima et al.[72] reported a reversible transition between LDA and HDA under high pressure at $\sim$130–150 K. The transition at the LDA-HDA boundary could be followed through optical microscopy and the different phases were confirmed using Raman spectroscopy.

The development of Environmental Scanning Electron Microscopy (ESEM) during the 1990s opened new possibilities to the study of the microscopic morphology of ice. Conventional SEM required samples to be imaged under high vacuum, which meant samples that produced a significant amount of vapor, e.g. biological samples, needed to be either dried or cryogenically frozen. This meant that processes involving transitions to or from liquids or gases in general could not be observed. On the other hand, ESEM

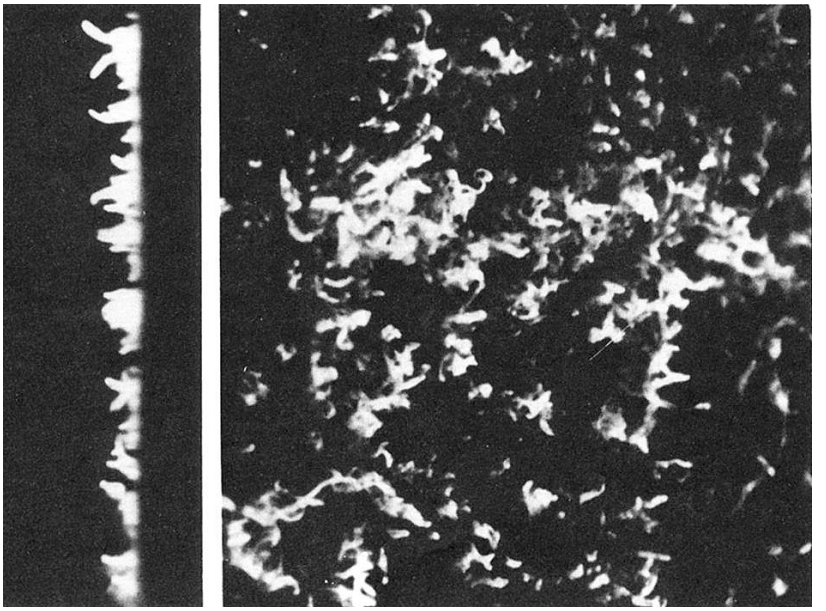

FIGURE 5.6: Optical microscopy of ice needles as photographed by Laufer et al.[83]. Both images are magnified 15 times. Needles are about 0.1 mm long.

allows the examination of specimens surrounded by a low-pressure gaseous environment (e.g. 1–50 Torr) and high humidity (up to 100%). Even liquids can be viewed in the microscope. In addition, it allows samples to be observed as they are grown by vapor deposition on a cold substrate, as is the case of ASW.

Chapter 6

The mesoscale morphologies of ice films

6.1 Introduction

Dust grains in interstellar space are typically covered with an icy film formed at the very low temperature (3–90 K) of the interstellar medium [84]; it has been estimated that most of the ice in the universe is to be found on these particles [68]. Larger icy bodies are supposed to have formed through the accretion and reprocessing of this material [85, 86]; icy films are found in the interstellar medium, in the Oort cloud, in planetesimals, asteroids, comets, and Kuiper-belt objects, on the surfaces of icy planets and moons, and in planetary ring systems and atmospheres, and much astrochemistry is presumed to take place on these icy surfaces. A fundamental question, on which hinge these astrophysical and astrochemical processes, is: in what forms — with what morphologies — may such ice films be deposited? An apparently unrelated area of science holds the key to answering this query. The deposition of films of ceramics, semiconductors, and metals is an extremely active field. Experimental results have been collated in an empirical *structure zone model*, which predicts the film morphology on the mesoscale depending on the substrate temperature and the gas pressure [87, 88]. To connect the two bodies of knowledge of film deposition and ice physics we undertook experiments in which we deposited films of ice at low pressure at 6–220 K. Our premise was to discover whether the structure zone model applies to ice, chemically very different to those materials from which it was derived. On one hand, our experiments were aimed at discovering the mesoscale morphologies of ice films with regard to bulk properties of astrophysical interest, such as porosity, which arise not only from the molecular scale but also from morphology at the mesoscale. On the other, this work furthers the understanding of the fundamental physics involved in the production of film morphologies, which as yet is only just beginning to be unraveled.

6.2 Ice films

6.2.1 Molecular structures

Although there are myriad forms of the solid phase of H_2O — ice — found on the Earth's surface [89], with very different morphologies and bulk properties, at the microscopic level they are all, from snowflakes to icebergs, composed of the same crystalline polymorph, hexagonal ice — ice Ih — which is the stable structure at the temperatures and pressures in our biosphere. Beyond these bounds, however, ice exhibits an extensive range of crystalline solid phases, or polymorphs, distinguished from one another by the arrangement of water molecules in the crystal lattice. The physical properties of the polymorph, such as density, conductivity, vapor pressure and sublimation rate, are dictated by its crystalline structure. There exist at least fifteen ice polymorphs [90]. Most are thermodynamically stable under some range of pressure–temperature conditions and many of the high-pressure polymorphs may be found in nature within icy moons and planets [91]. However, at the lowest temperatures and pressures, water freezes not in a crystalline phase, but as amorphous ice [90, 92]. In laboratory vapor-deposition experiments hexagonal crystalline ice (Ih) is formed above $\sim$ 150 K, while between $\sim$ 130–150 K there appears another crystalline phase: cubic ice (Ic). Below $\sim$ 130 K, the ice produced by vapor deposition is amorphous; this ice is frequently termed amorphous solid water (ASW). ASW differs when deposited at lower and higher temperatures. At $\lesssim$ 30 K, a higher density amorphous form is obtained, while at $\sim$ 30–130 K a lower density amorphous form is deposited [46, 68]. There is a great deal of debate as to whether different amorphous ice structures represent frozen versions of different liquid polymorphs of water with an associated phase transition [92, 93]. High-density amorphous ice constitutes the frost on interstellar dust grains, while the low-density form is present on comets and Kuiper-belt objects. Cubic and hexagonal crystalline ice is found at higher temperatures: on icy planets, moons and asteroids, in planetary atmospheres and ring systems, on comets that have undergone solar heating, and in the Kuiper belt [91].

The preceding summary has set out ice-film structure at the molecular scale, where the hydrogen bonds are responsible of all previous polymorphs. However, just as ice on the Earth's surface is all ice Ih at the microscale, but has different mesoscale and macroscale morphologies from snowflakes to icebergs, beyond their molecular structure, films of ice may have different morphologies at the mesoscale with a concomitant impact on their bulk properties.

6.2.2 Mesoscale morphologies

In another realm of science, for many years solid films of numerous different materials have been deposited onto substrates from the vapor phase [87, 88]. The field is driven

by a huge number of technological applications, but also has much scientific interest. One of the key differences between films and bulk materials is in their morphologies. While the very thinnest films of, say, less than twenty monolayers thickness, are epitaxial — that is, influenced by their substrate — this influence diminishes with film thickness, and it is found empirically with ceramics, semiconductors, and metals that once a growing film passes some hundred or so monolayers in thickness it begins to show characteristic morphologies independent of its substrate. From the 1960s on efforts have been made to construct an empirical classification of the morphology of a film depending on the conditions of its deposition. This has culminated in the *structure zone model*, which gives the distinct film morphologies obtained as a function of variables involved in the film deposition; in recent versions of the model, these variables are often the renormalized substrate temperature T/T_M, where T_M is the melting point of the material being deposited, and the ion energy, which is inversely related to the decrease of gas pressure in the sputtering techniques used in physical vapor deposition experiments [88, 94]. We portray a version of the model in Fig. 6.1. The structure zone model, it should be stressed, is simply a collection of empirical observations, which describes well the trends seen in experiments with ceramics, semiconductors, and metals.

The question we wished to answer is whether these same morphologies are found in films of ice, despite the very different chemical bonding in ice — which has an extensive network of directional hydrogen bonds — compared to the materials from which the structure zone model was devised. Our interest was principally to study sub-micrometer- to millimeter-thickness ice films at a range of low temperatures and pressures corresponding to a variety of astrophysical environments, in which conditions range from the lowest temperatures and pressures, to others in which, although still at low pressure, ice growth is subject to radiation (infrared, optical, ultraviolet, X-ray) and particle bombardment (electrons, protons, ions).

6.3 Experimental setup

In our experiments we used a FEI Quanta 200 environmental scanning electron microscope (ESEM) equipped with a liquid helium cold stage to grow ice films *in situ* at low pressures and at temperatures of 6–220 K. As well as a high-vacuum mode as in a conventional scanning electron microscope, an ESEM has further operating modes in which the chamber can function in the presence of water vapor and/or an auxiliary gas at pressures of up to 4000 Pa, and observations can be made without the need to metal coat the sample. The combination of the ESEM with a liquid helium cold stage makes it possible to grow and image ice films *in situ* within the instrument. We began by evacuating the chamber in the high-vacuum mode of the microscope (target pressure 6×10^{-4} Pa) and lowering the substrate to the working temperature. The microscope was set up so that the helium cold finger, together with a thermostat, was directly beneath the substrate on which we grew the ice film. We employed several substrates

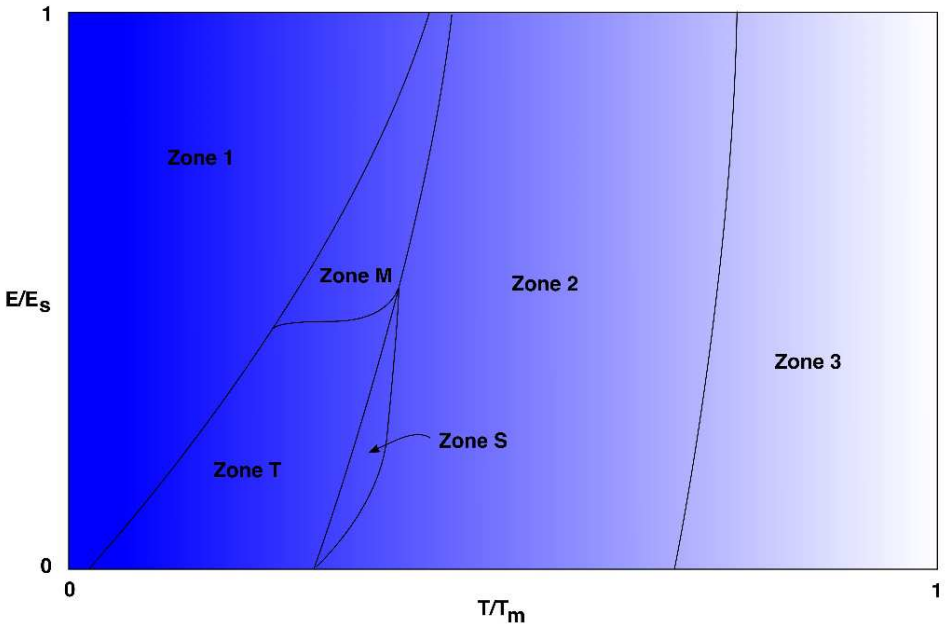

FIGURE 6.1: A version of the structure zone model of film deposition with axes T/T_m, where T is the substrate temperature and T_m is the melting point of the material being deposited, and E/E_s where E is the admolecule energy and E_s is the sputtering threshold of the material being deposited : zone 1 (Fig. 6.2), porous morphology consisting of tapered columns separated by voids; zone T (Fig. 6.3), transition morphology with no long-range structure beyond the nanoscale; zone S (Fig. 6.4), spongelike morphology characterized by a three-dimensional open network; zone M (Fig. 6.5), matchstick morphology consisting of parallel columns with domed tops; zone 2, columnar crystalline grain structure; and zone 3, recrystallized crystalline grain structure.

(brass, carbon, copper, platinum, and titanium in flat samples that were smooth at the micrometer resolution of the microscope and were thermally coupled as well as possible to the cold stage beneath them); we did not detect differences in film morphology between them. To grow an ice film we switched the microscope to low-vacuum mode, in which we could inject water vapor into the chamber for a given length of time and at a determined target pressure. We either used demineralized water alone, or else bubbled helium through the water prior to injection to provide an inert auxiliary gas in the chamber and to reduce the water vapor pressure. The ice film was then deposited on the substrate, which was the coldest point within the microscope. We switched again to high-vacuum mode to image the results.

After each experiment we heated the substrate to remove the ice film. As we took advantage of an existing ESEM setup for our experiments, rather than having to construct the experimental apparatus from scratch, which would have been prohibitively expensive, there were certain limitations around which we had to work. We did not have the means to measure the ice film thickness, except when the film peeled away from the substrate (see Fig. 6.3(a)), and the temperature measurement was at the base of the ice film, not at its surface. The microscope chamber walls were not thermally isolated from the room, so radiative heating of the sample altered the ice surface over a period of tens of minutes to an hour, even though the substrate was maintained at the programmed temperature.

The target pressure to which the ESEM controller was set would be the pressure present in the system if it were at equilibrium, but our experiments took place far from equilibrium; as soon as water vapor entered the experimental chamber it was sequestered by deposition on the substrate. The target pressure and injection time thus regulated the amount of water vapor allowed to enter the experimental chamber. After the entry of a controlled amount of vapor, the system was set back to high-vacuum mode. The pressure at the ice surface during injection is a dynamical variable dependent on the injection time and on the presence or absence of helium as an auxiliary gas, and the system tends to equilibrium at the vapor pressure of ice at the working temperature, given by the Clausius–Clapeyron equation $p = ae^{-b/T}$. For temperatures below around 150 K this implies that the pressure equilibrates to a value orders of magnitude lower than the high-vacuum mode target pressure 6×10^{-4} Pa. We are not aware of any direct measurements of ice vapor pressure performed at these temperatures — it does not seem to be a trivial task — and values sometimes quoted in the literature are from formulations based on theoretical studies (the Clausius–Clapeyron equation with higher order corrections), with the numerical values of the terms (a, and b in the Clausius–Clapeyron equation, etc) determined by fitting at higher temperatures. In general, then, the surface pressures involved in these experiments vary enormously from extremely low pressures in the lowest-temperature zones of the structure zone model, up to a few Pascals in the higher-temperature zones.

6.4 Results

6.4.1 Lowest temperature zones

The region of lowest substrate temperature in the structure zone model is occupied by zone 1. Zone 1, or cauliflower morphology, has been found in other materials to consist of competing void-separated tapered columns whose diameters expand with the film depth according to a power-law, so the film surface resembles a cauliflower, showing self-similarity over a range of scales. We produced an ice film of this morphology in

the example in Fig. 6.2 using water vapor accompanied by helium as an auxiliary gas in the chamber deposited on a substrate at 6 K. We injected water bubbled through with helium with a target pressure of 10 Pa for 6 s, then reset the microscope to target pressure 6×10^{-4} Pa, and the film was deposited on a titanium substrate maintained at 6 K. We show in Fig. 6.2 two images of cauliflower surface morphology from varying perspectives, an oblique view and a plan view; they are taken at different scales to illustrate the self-similarity.

By depositing the ice film at the same substrate temperature, but at a higher target pressure for a shorter time without an auxiliary gas, we obtained, in the example shown in Fig. 6.3, zone T, or transition morphology, in which there is no long-range structure above the nanoscale. We injected water with a target pressure of 133 Pa for 1 s, then reset the microscope to target pressure 6×10^{-4} Pa, and the film was deposited on a copper substrate at 6 K. The general view seen in Fig. 6.3(a) shows the featureless surface characteristic of zone T; the film in this experiment had poor adhesion to the substrate and peeled away in places, enabling us to measure its depth as approximately 2 μm. Successively closer views in Figs 6.3(b) and (c) allow us to see the boundaries of the individual densely-packed grains making up the surface, which were made visible as electronic charge accumulated on the grain boundaries of the poorly conducting ice surface during imaging.

In qualitative terms, the morphology of zone 1 is driven by a competitive process of growth of clusters at all scales, leading to a fractal geometry, while greater mobility of admolecules in zone T than in zone 1 smooths out the surface. As they form at the lowest temperatures, both zone 1 and zone T morphologies can be presumed to be composed of high-density amorphous ice. We heated the substrate to remove the ice film on concluding the experiment, and we noted that at close to 30 K the water vapor pressure in the chamber increased sharply, which we attribute to sublimation during the transition from high- to low-density amorphous ice. We did not however see any mesoscale structural change associated with this transformation at the molecular scale. These experiments at the lowest temperatures correspond to the conditions under which ices that have never been heated above 30 K should exist: in cold regions of the interstellar medium and the Oort cloud.

6.4.2 Intermediate temperature zones

At substrate temperatures above those of the transition morphology of zone T, a sponge-like morphology has been described for metallic films [95]. We were able to reproduce this morphology, zone S, with an ice film, by injecting water vapor for a longer time than for zone T. The two images of the morphology we present in Fig. 6.4 were taken at different stages during a long injection process. We used a copper substrate in this experiment. Fig. 6.4(a) was after 83 s of injection of water with a target pressure of 10 Pa, then reset to target pressure 6×10^{-4} Pa, with the substrate at 6 K, and (b)

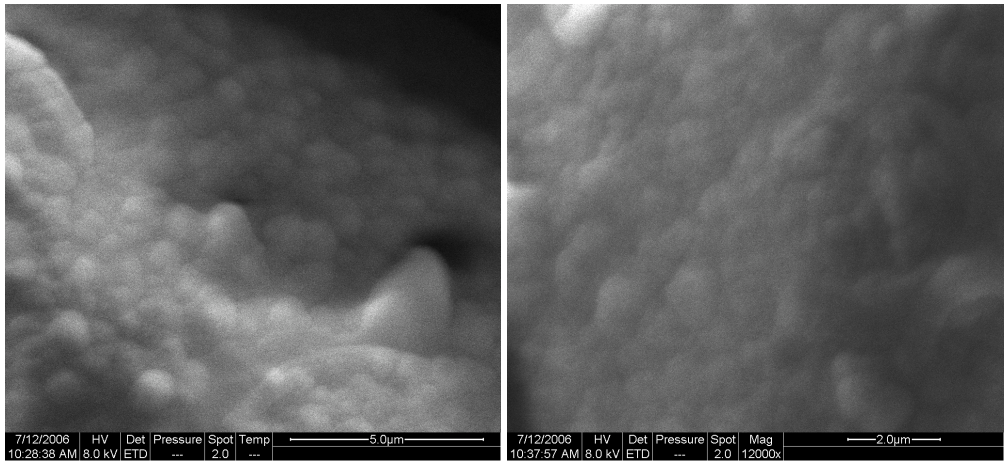

FIGURE 6.2: Zone 1, cauliflower morphology, film produced with water bubbled through with helium injected with a target pressure of 10 Pa for 6 s, then reset to target pressure 6×10^{-4} Pa, deposited on a titanium substrate at 6 K.

Fig. 6.4 was following a further 55 s of injection at target pressure of 10 Pa, during which the substrate temperature rose transiently to 80 K, followed by a reset to target pressure 6×10^{-4} Pa. As shown in Fig. 6.4, this morphology is characterized by a three-dimensional open network of material like a sponge.

On the other hand at substrate temperatures above those corresponding to zone 1 cauliflower morphology, and for relatively high admolecule mobility there appears the final zone in the low-temperature region of the structure zone model: zone M, or matchstick morphology. In the examples of this morphology we reproduce in Fig. 6.5 we see very large columns tens of micrometers in diameter resulting from ice deposition over several minutes using helium as an auxiliary gas in the chamber. We injected water bubbled through with helium for 6 minutes with a target pressure of 133 Pa, then reset the microscope to target pressure 6×10^{-4} Pa, and the film was deposited on a platinum substrate at 6 K. The columns display the domed tips characteristic of matchstick morphology, and also show interesting substructures; they are segmented both on the tip and along their length, giving them a biomimetic shape, like an icy worm. These large matchsticks may have been the morphology seen in experiments by Laufer et al. [83], who described an ice film grown at somewhere between 20–100 K as looking like "a shaggy woolen carpet".

The ice structures in zones S and M should appear in astrophysical contexts at low pressures and temperatures around the range $\sim$ 30–130 K typical of the Kuiper belt and colder icy moons; they should thence typically be composed of low-density amorphous ice.

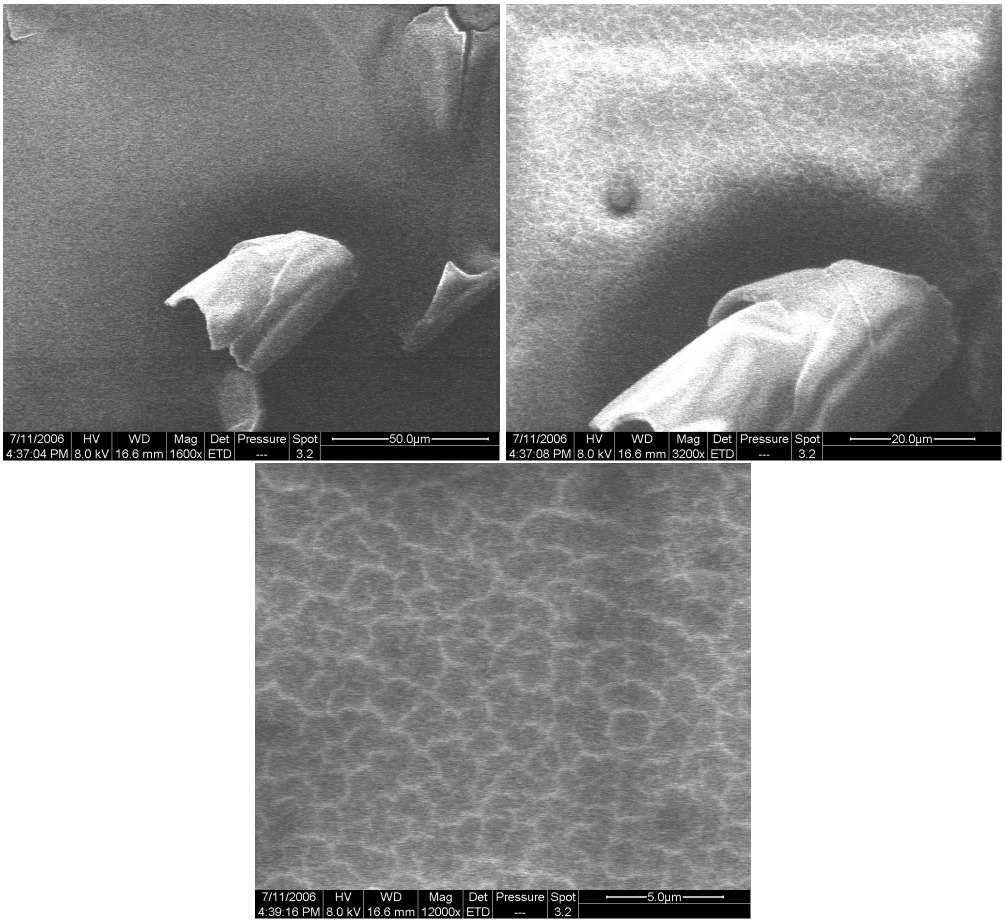

FIGURE 6.3: Zone T, transition morphology, film produced with water injected with a target pressure of 133 Pa for 1 s, then reset to target pressure 6×10^{-4} Pa, deposited on a copper substrate at 6 K.

6.4.3 Morphologies at higher temperatures

The zones in the structure zone model are not all disjunct; in Fig. 6.6(a) we present an example of a morphology intermediate between zones 1 and M. We injected water with a target pressure of 133 Pa for 13 minutes, then reset the microscope to target pressure 6×10^{-4} Pa, and the film was deposited on a brass substrate at 6 K. Although there is as yet no quantitative physical model for the transition from zone 1 to zone M, it can be viewed qualitatively in terms of competitive growth that produces a fractal morphology giving way to noncompetitive growth that leads to a columnar morphology; the existence of an intermediate morphology intimates that this is not a nonequilibrium

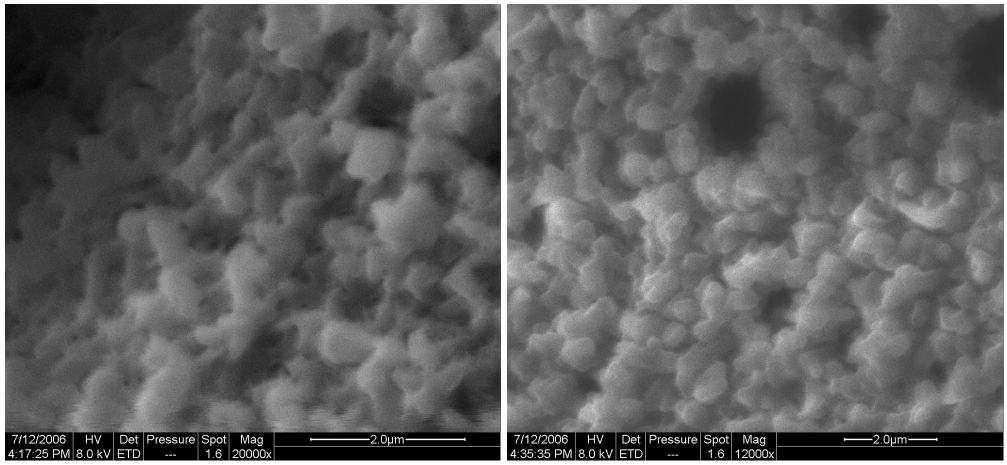

FIGURE 6.4: Zone S, spongelike morphology, film deposited on a copper substrate. Left: After 83 s of injection of water with a target pressure of 10 Pa, then reset to target pressure 6×10^{-4} Pa, with the substrate at 6 K. Right: Following a further 55 s of injection at target pressure of 10 Pa, during which the substrate temperature rose transiently to 80 K, followed by a reset to target pressure 6×10^{-4} Pa.

phase transition. Upon heating the substrate in this experiment we induced the transient growth of whiskers on top of this film at a substrate temperature of 220 K, as we see in the sequence of Figs 6.6(b)–(d). These whiskers are therefore almost certainly of hexagonal crystalline ice, whose propensity to form complex dendritic structures is familiar from snowflakes. This knowledge should forewarn us that the morphologies we should encounter in zones 2 and 3 of the structure zone model, at high substrate temperatures corresponding to the deposition of crystalline ice, would reflect this complexity. Nonetheless we were taken aback by the beauty of the structures we obtained in these conditions, seen in Fig. 6.7. The hexagonal crystalline nature of this ice is reflected in the 60^o angles of growth of the branches, shown most clearly in Fig. 6.7(c). Although these forms are consistent with the tendency of ice to dendritic growth, seen, for example, in snowflakes [96], here the environment is significantly different. This fascinating palmlike morphology of branched whiskers is intermediate between dendritic growth and the whiskers of Figs 6.6(c)–(d). To obtain these structures we injected water with a target pressure of 10 Pa for 15 minutes, then reset the microscope to target pressure 6×10^{-4} Pa, and the film was deposited on a carbon substrate at 6 K; the growing ice surface became progressively more thermally insulated from the substrate as the film depth increased and the morphology changed correspondingly. In our experiments the microscope chamber is evacuated but not thermally isolated from its surroundings, so the walls are at room temperature and radiate accordingly, and the film surface temperature reflects this. The temperature of the upper surface in this experiment can be

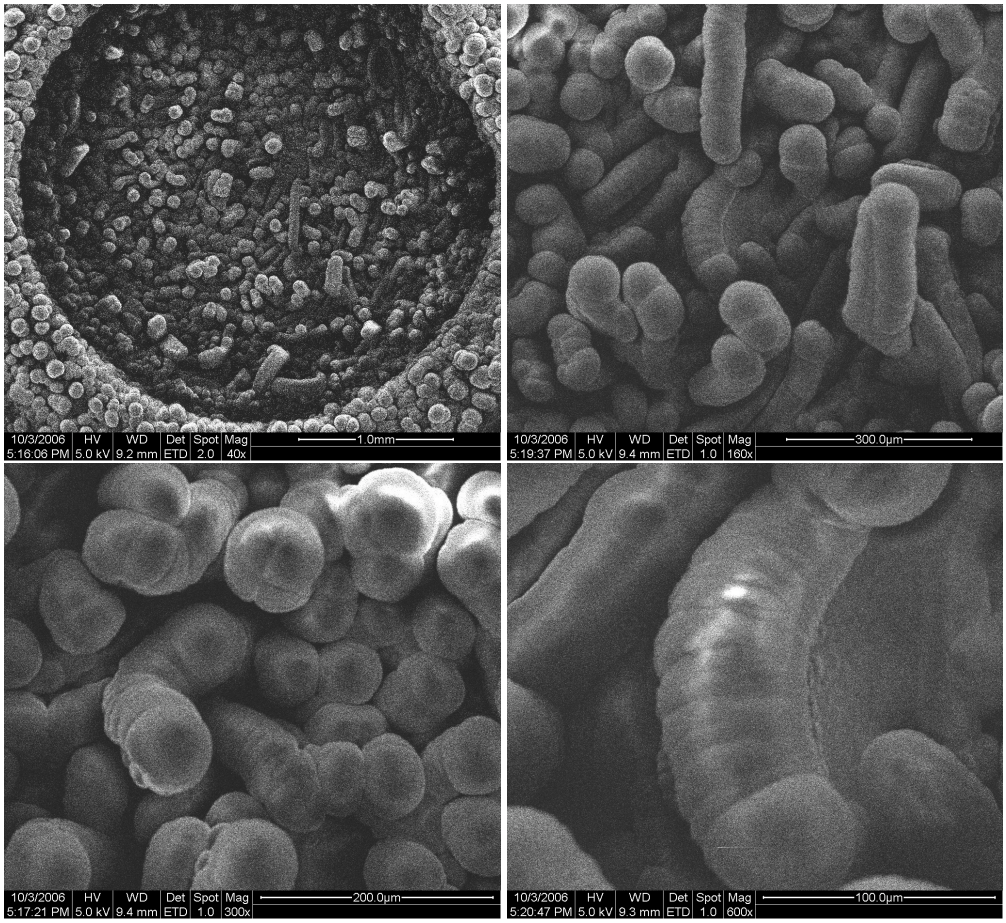

FIGURE 6.5: Zone M, matchstick morphology, film produced with water bubbled through with helium injected for 6 minutes with a target pressure of 133 Pa, then reset to target pressure 6×10^{-4} Pa, deposited on a platinum substrate at 6 K.

estimated to be close to 200 K, taking into account the low thermal conductivity of the ice and the substrate and the radiation received. At this temperature there is high admolecule mobility, resulting in surface diffusion, both of molecules and of heat, and sublimation; this dynamic equilibrium of fluxes along and perpendicular to the surface is presumably the basic physics involved in producing this skeleton of palmlike structures formed by highly ordered branched whiskers.

These whiskerlike and palmlike crystalline ice structures could be present under astrophysical environments in which the ice surface has been heated above 130 K, such as comets, Saturn's rings, or the surfaces of some icy moons and planets.

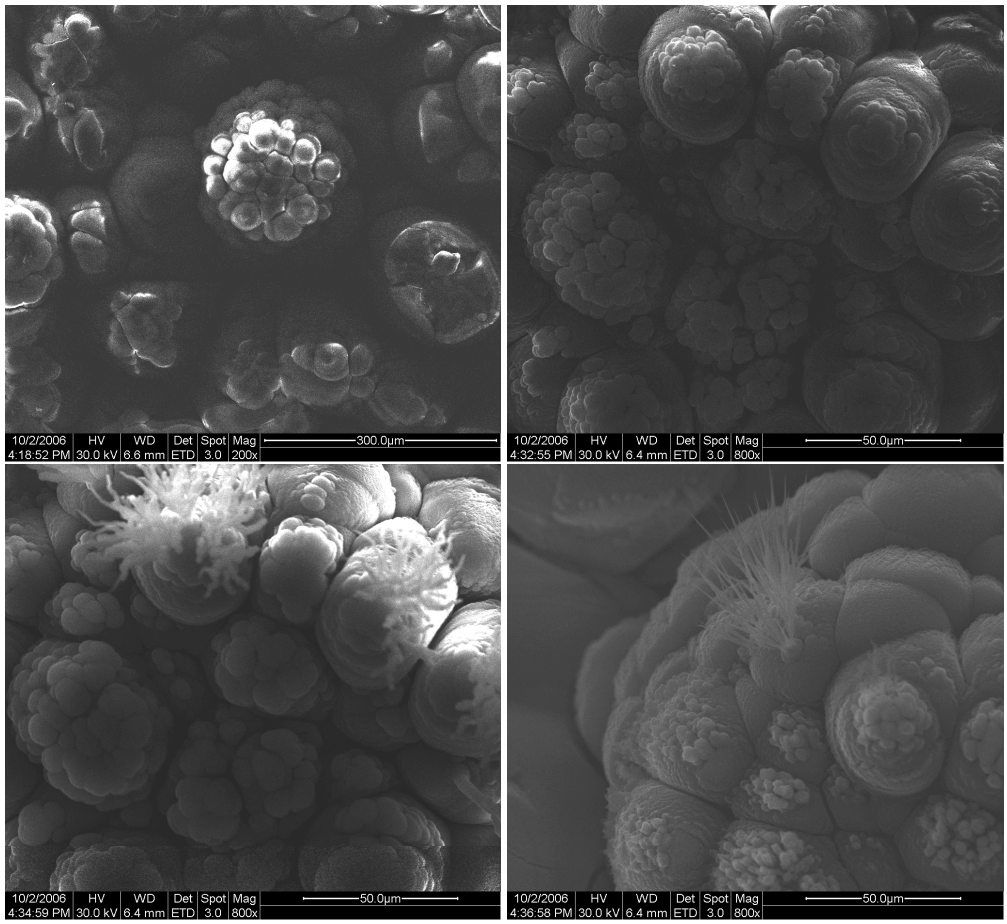

FIGURE 6.6: (a) Morphology intermediate between zones 1 and M produced with water injected with a target pressure of 133 Pa for 13 minutes, then reset to target pressure 6×10^{-4} Pa, deposited on a brass substrate at 6 K. (b, c, and d) Whiskers of ice form on top of this morphology during heating of the substrate as the temperature reaches 220 K.

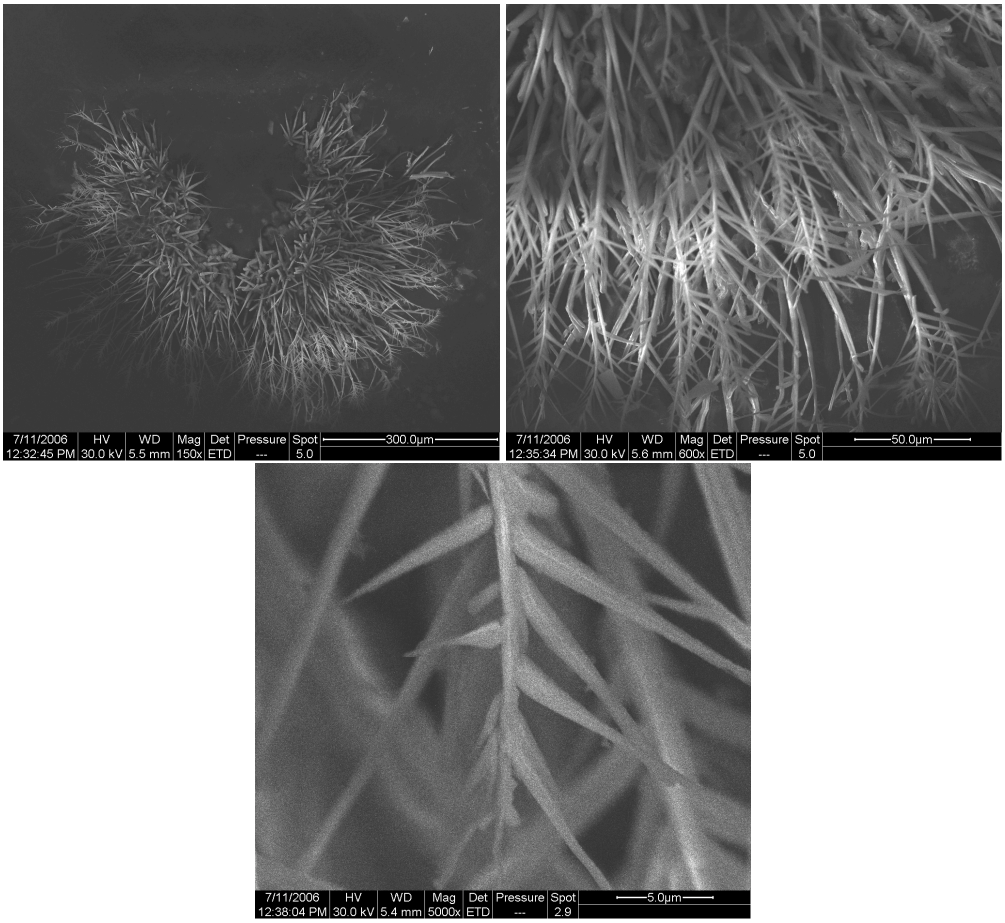

FIGURE 6.7: Dendritic morphology resembling a palm tree produced with water injected with a target pressure of 10 Pa for 15 minutes, then reset to target pressure 6×10^{-4} Pa, deposited on a carbon substrate at 6 K.

6.5 Discussion

As we have seen, structure zone model morphologies do appear in ice films. Can this knowledge contribute to understanding the fundamental physics of the structure zone model? And can such an understanding in turn allow us to comprehend better the astrophysics?

The two axes of the structure zone model commonly shown in work on ceramics, semiconductors or metals are the renormalized substrate temperature and the ion energy, which is inversely proportional to the gas pressure in sputtering experiments used in

that work [88, 94]. On the other hand the deposition technique employed in these experiments is evaporation, involving thermal energies ($3/2\,kT < 1$ eV) for the admolecules. However, the energy required to sputter a water molecule is ~ 0.2 eV [97], much lower than the 10–30 eV sputtering threshold for ceramics, semiconductors or metals [88]. To generalize the structure zone model we may renormalize the scale of the second axis by the sputtering threshold, in the same way as the substrate temperature is renormalized by the melting point for the first axis. This we have done in Fig. 6.1. It becomes apparent then that the physical basis for the two axes is admolecule mobility induced in one case by the temperature of the film itself, and in the other by the impinging admolecules from the vapor. The latter mechanism is related in these experiments to the presence or absence of helium as an auxiliary gas in the chamber that will thermalize with the chamber walls. For sputtered films material leaves the sputter source with relatively high energies (several electron volts). As the gas pressure is increased more scattering occurs and the arrival energy of the sputtered material decreases. For evaporated films, on the other hand, the arrival energies are low; if gas assist is added then the energy per admolecule increases. That the different effects of the two sources for admolecule mobility lead to more or less compact structures we can comprehend by noting that, unlike thermal mobility, admolecule movement induced by bombardment is highly directional. This directionality is an avenue to explore in moving towards a physical understanding of the structure zone model as a consequence of the competition between the spatially disordered deposition of particles on the growing film surface and the ordering effect of activated particle mobility processes.

The basic structure zone model is the result of normal deposition, and of deposition when the vapor flux has a spread of angles about the normal; this is our case, and is the most likely case in a natural setting. When the vapor flux is collimated and its angle is controlled, the columnar morphologies grow following the incident beam, and so-called sculptured thin films can be produced [88]. In columnar morphologies, the column spacing increases as the angle of beam and of the growing columns is further from the normal. It is probable that such sculptured thin films of ice were formed in experiments of Kimmel and coworkers, in which beams of water vapor were deposited at a variety of growth angles on a surface at low temperature, and the amorphous films grown at more oblique angles were found to be more porous [80, 98].

It has been noted in both experiments and simulations of film deposition that there is an equivalence in terms of the mesoscale morphology produced between the substrate temperature and the deposition rate [87, 99]. This we can comprehend in molecular terms as a competition between the timescale of the surface kinetics, and the mean time between admolecule arrival at the surface. As long as the latter is longer than the former — i.e., below a certain threshold deposition rate — the deposition rate is not significant in terms of morphology and alters only the time scale of the film growth. It should be stressed that the field of solid film growth is largely empirical, that experiments are generally undertaken on materials with industrial applications in mind, and that although there are complex simulations using molecular modeling techniques, there

is not yet a full understanding of the theoretical basis of why materials show these structures on the mesoscale; the latter question is being tackled in parallel with these experiments [99].

Knowledge of the existence and morphologies of these mesoscale structures ought to aid understanding fundamental physical and chemical processes involving surfaces coated with icy films. In the very thinnest films epitaxial growth upon the substrate is clearly determinant, as can be seen in work on very thin films of ice [100]. As the film thickness increases, the substrate ceases to play a role in the film morphology and the mesoscale morphologies of the structure zone model appear. Consistent with this development of mesoscale morphologies, ice-film experiments by Hornekaer et al. [101] show increasing porosity as the film thickness increases. Icy mantles of nanometer thickness form on dust particles in interstellar clouds, through condensation from the gas phase or by reactions on the grain surfaces. As dense cores within interstellar clouds collapse, icy grains are incorporated in the coldest regions of the disk. Closer to the protostar, icy mantles are evaporated and reform as the disk cools. Over a few million years, the icy dust aggregates, forming small planetesimals, and subsequently planets and moons. The remaining planetesimals form the Oort cloud and Kuiper belt, asteroids and comets made up of regolith and ices. The bulk properties of these ice morphologies are important for understanding physical and chemical processes involving the surfaces of these bodies. On Earth, once such porous materials aggregate beyond the micrometer scale their weight compacts them. This will not occur in low-gravity environments, so the mesoscale porosity materials we have obtained in our experiments can only occur in thin films on Earth, but may be much more widespread as aggregates in lower-gravity conditions. The agglomeration of particles during planetismal formation should certainly be affected by the porosity of the icy film, which should aid aggregation and prevent fragmentation; the case of cometary dust aggregates is similar. Cometary ices are undoubtedly porous; our work imparts an understanding of how such porosity arises at the mesoscale and so provides a counterpoint to work on producing laboratory analogues of cometary ices [102], in which the effects of porosity are noted but the morphology is unknown. On the other hand, in the context of energetic processing of ice films, it has been suggested that, owing to cosmic ray bombardment, ice on interstellar grain mantles should be compact in structure, and it has been shown by infrared absorption spectroscopy that ice porosity decreases after ion irradiation [103]; in our terms this would correspond to the passage from zone 1 to zone T. A reconsideration in terms of the structure zone model morphologies of what is at present often placed under the catch-all label of porosity is one of the basic proposals we wish to put forward.

Our experiments have been performed with water alone, while astrophysical ice is generally mixed with other volatile solids such as carbon monoxide, carbon dioxide, ammonia, methanol, and methane [85, 86]. We can view the effect of these impurities in terms of the structure zone model by noting that as they have different melting points and sputtering thresholds to water, we may expect them to alter the position of the

deposited material on the structure zone model diagram. Depending on how far the position on the diagram changes, a structure zone boundary may be crossed, in which case the material could possess a different morphology to pure ice deposited at the same temperature and pressure.

An intriguing aspect of this work is the finding that ice on its own can form biomimetic structures under astrophysical conditions. Knowledge of this phenomenon is important for astrobiologists searching for life in similar extreme conditions in space, and is a timely reminder that biomorphic forms, especially at small scales, are not in themselves evidence of life.

Part III

Chemical Gardens

Chapter 7

Chemical Gardens: Introduction

There is a wide variety of mechanisms in nature that produce tubular structures through self-organizing and templating processes. We can find many examples with and without the influence of biological entities, but they are always a consequence of physical and chemical interactions. Examples in biology include mollusk shells, tubular algae, coral exoskeletons, tube worms... The range of geological processes that produce tubular growth is even wider. The most common cases are the speleothem formations found in limestone caves, including stalactites, stalagmites, soda straws and helictites [104]. They are all grown by precipitation of carbonate dissolved in water drops flowing along the cave rocks. But the most spectacular formations are undoubtedly the hydrothermal vents found on the seabed near volcanically active regions, the so-called black smokers [105]. The precipitation in this case occurs at the interface where the hot mineral-rich fluid flowing from the seabed encounters the colder surrounding seawater. In order to study tube formation in a laboratory we use "silicate gardens" or "chemical gardens". These are tree-like tubular formations that are grown when a metallic salt is immersed in a sodium silicate solution [106].

Our interest in this field was triggered by the opportunity to grow chemical gardens in microgravity on the International Space Station. We have studied the formation, structure and composition of gardens grown from different metal salts and in different conditions in order to better understand the physics and chemistry involved.

Speleothems

Speleothems are cave formations that grow by mineral deposition, usually in limestone caves. As water seeps through the cracks in the cave's bedrock it dissolves and carries certain compounds, like calcium carbonate and calcium sulfate. The solubility of these

compounds is increased by carbon dioxide dissolved in the water. When this solution reaches an opening in the cave, it releases the carbon dioxide and the solutes precipitate. Accumulation of these precipitates over the years gives rise to to a variety of different morphologies: stalactites, stalagmites, columns, straws, draperies... There are many factors that influence the shape of the speleothem. Mainly the rate of flowing water, the amount of acid in this water, the temperature and humidity of the cave, and the strength and direction of wind currents. The internal structure and composition of the speleothem can be used, like ice cores, as a way to measure the past climate changes [107].

Stalactites are conical formations that grow from the ceilings of limestone caves (see Figure 7.1a). They are formed by the precipitation of calcium carbonate that is left behind by every drop of water that drips off the cave ceiling. The growth rate can be as fast as a few millimeters per year, depending on the flow of water and its richness in concentration of carbonates and carbon dioxide, and they can grow to a length of several meters. Where the dripping water hits the cave floor, further precipitation of carbonate initiates the growth of a stalagmite (see Figure 7.1b). If a stalactite and a stalagmite grow long enough, they can meet and fuse forming a column.

Soda straws are the precursors of stalactites. They are hollow tubes grown from the ceiling by dripping of mineralized water (see Figure 7.1c). If the hole at the bottom of the straw is blocked, or if the water begins flowing along the outer surface of the tube, the soda straw will become a stalactite.

Helictites are the most delicate of cave formations. They are thin needles of calcium carbonate that shift their growth direction over time. The result is a curved morphology that looks as if they were grown in zero gravity (see Figure 7.1d). The cause of this curving is most likely capillary forces. If the water flows through a very thin central cavity in the helictite, like it happens with straws, capillary forces would be strong enough to transport the mineralized water against gravity.

Biological examples

Many living organisms develop or grow external tubular structures, sometimes templated by their own body. These structures can cover a range of different functions for the organism. Usually they provide protection or shelter from predators, as in the case of shells or exoskeletons, but they can also provide structural stability that enables the organism to out-grow its competitors and reach out for food.

Some bacteria grow a polysaccharide sheath that attracts and bonds metal cations, producing a tubular structure templated by the organism's body [109]. Tubular fossilized structures found on sedimentary layers of banded iron formations have been attributed

FIGURE 7.1: Typical speleothems: a) stalactite, b) stalagmite, c) soda straw, d) helictites [108]. Stalactite and stalagmite in these pictures are about 1 meter long; soda straw and helictites are a a few centimeters long.

to be of biological origin [110]. Mollusk and gastropod shells are grown by the precipitation of calcium carbonate secreted by the animal's mantle [111].

Corals are a particularly interesting example. They were initially believed to be plants, due to their branched morphology (see Figure 7.2a). It wasn't until the 18th century that their cell membranes could be analyzed and they were established to be animals. Corals are colonies of thousands of genetically identical individuals called polyps. Each polyp is only a few millimeters in diameter. They attach to rocks at the bottom of shallow waters and feed on plankton and small fish. The formation of the calcareous exoskeleton involves deposition of the mineral aragonite by the polyps from calcium and carbonate ions they acquire from seawater. Its function is to protect the organism from predators and the elements. The rate of deposition varies greatly across species and environmental conditions, but it takes many generations for polyps to build the coral reefs that are found in tropical oceans and that provide shelter for some of the richest ecosystems found on Earth [112, 113].

Other examples of templated tubular growth in biology are the different species of tube-building annelid worms (see Figure 7.2b). Some of them, like the serpulid family, secrete tubes of calcium carbonate and have an operculum that blocks the entrance of their tubes when they withdraw inside. But the most spectacular of them is undoubtedly the giant tube worm that lives near deep sea hydrothermal vents. These worms attach themselves to the sea floor and start growing a cylindrical shelter around their body. They have a highly vascularized, red plume at the tip of their free end which is an organ for exchanging compounds such as oxygen, carbon dioxide, and hydrogen sulphide with the seawater. Although the worms have no eyes, they can sense movement and vibrations and will retreat into their protective tubes when threatened. These worms

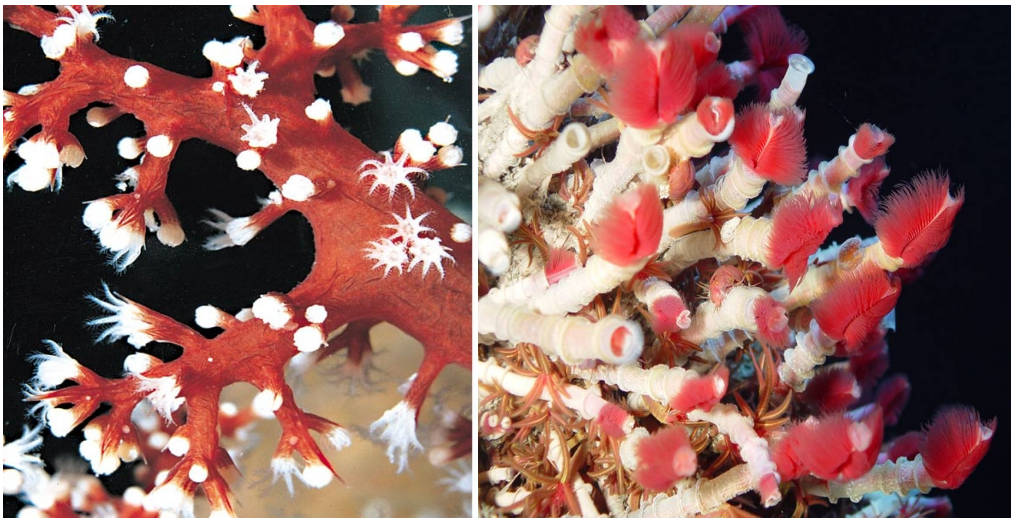

FIGURE 7.2: Examples of biological tubular structures: a) coral reef, each polyp is a few millimeters in diameter; b) giant tube worms, the tubes are 2–3 cm in diameter. [114]

exhibit a surprising growth rate (as fast as 85 centimeters per year) and reach over 2 meters in length [115]. Tubes are white, flexible and tough. They are mostly made of chitin that is secreted from the so-called pyriform glands and is added at the open end of the tube. The tubes are visibly sectorized, indicating a possible seasoning in their growth rate.

Hydrothermal vents

Hydrothermal vents are fissures on the planet's surface from which geothermally heated water flows. This water is rich in dissolved minerals from the crust, most commonly sulfides. They are found in areas where tectonic plates overlap or move apart. When this happens under the sea, the encounter between the superheated mineral-rich water expelled from the vent and the cold high-pressure water at the sea bottom causes iron sulfides to precipitate around the flow, growing chimney-like structures called "black smokers" (see Figure 7.3a). They are named after the dark hue of the particles they emit, mostly sulfur-bearing minerals, or sulfides. The term "white smokers" refers to vents that emit lighter hued minerals, such as those containing barium, calcium or silicon. These vents also have lower temperature plumes (see Figure 7.3b).

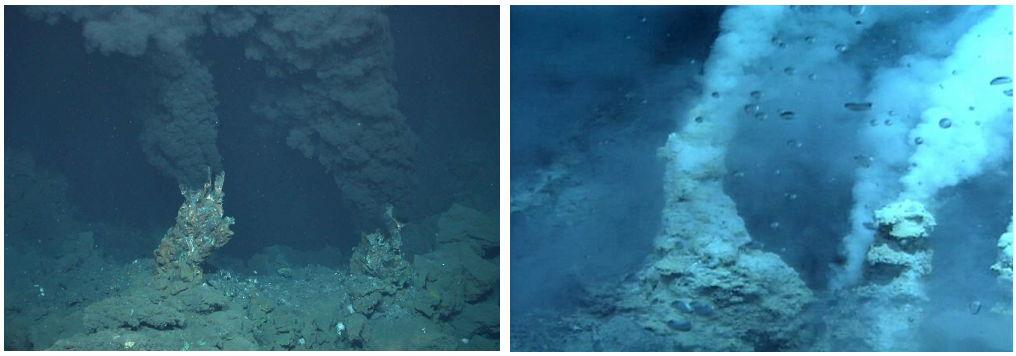

FIGURE 7.3: Examples of deep sea hydrothermal vents: a) black smokers, b) white smokers [116].

The water that flows from the sea-floor hydrothermal vents consists mostly of sea water drawn under the earth through faults and porous sediments, along with some magmatic water released by the upwelling magma. This emerging water can be at a temperature of up to 400^{o}C [117], but does not boil because the water pressure at that depth (about 300 atm) exceeds the vapor pressure of the aqueous solution. It is also extremely acidic, having a pH value as low as 2.8. The initial stages of the chimney formation begin with the deposition of the mineral anhydrite, followed by precipitation of sulfides of copper, iron and zinc, filling in the chimney's gaps and making it denser over the course of time. Some of these chimney structures can grow at a rate of 30 centimeters per day and reach heights of 60 meters [118, 119], but they do not usually remain active for a long period of time.

The first of these underwater chimneys was found in 1977 along the Galapagos Rift. A whole chemosynthetic ecosystem was discovered growing around these deep-sea hydrothermal vents [105]. The biological density of this ecosystem is surprising when compared to the rest of the sea floor, specially considering the absence of photosynthetic activity at this depth. All previously known life forms were dependent on the Sun's energy and organisms living in deep oceanic waters were assumed to be feeding on detritus sinking from upper levels of the ocean. However, this could not account for the number of organisms found living around hydrothermal vents. These large communities are able to sustain such vast amounts of life by feeding on chemosynthetic bacteria. These bacteria can convert methane and hydrogen sulfide (which are toxic for most other known life forms) provided by the black smokers into organic material through the process of chemosynthesis. The whole ecosystem relies on the continued existence of the hydrothermal vent as a source of energy.

The chemosynthetic bacteria grow into a thick mat that covers the outer surface of the chimney. Soon, tiny animals such as amphipods and copepods come to feed on the

bacteria. These are followed by snails, shrimp, crabs, tube worms, fish and octopuses. In their most advanced stages vents are home to mussels, a variety of worms, anemones and a large population of crabs, as well as many of the earlier colonists. The variety of species forms a food chain with grazers, predators and scavengers that will self-sustain as long as the vent remains active.

Over 300 new species of animals have been discovered at vents. Many are found nowhere else on earth and could not exist outside those physical conditions. This emergence of life has driven the proposal of new biological and bio-atmospheric theories, including a possible hydrothermal origin of life based on sulfur metabolism [120, 121]. The convergent evolution of similar species found around geographically distant vents is also a major support for the theory of evolution and a perfect example of natural selection at work in a fairly confined habitat. There is strong evidence that a liquid ocean exists below the icy surface of Jupiter's moon Europa. If this ocean contains hydrothermal vents as well, which could be a consequence of tidal heating, scientists speculate they could be wellsprings of alien life.

Chemical gardens and the origin of life

Chemical gardens are tree-like tubular formations that are grown when we immerse a solid metal salt into an aqueous solution of sodium silicate (otherwise known as waterglass) [106]. The chemical garden reaction was first observed and described by Johann Rudolf Glauber in 1646 [122] when he introduced ferrous chloride crystals into a solution of potassium silicate. When the salt begins to dissolve, it develops a metal silicate coating around itself. This coating acts as a semipermeable membrane which, forced by osmotic pressure, intakes water from the silicate that will continue to dissolve the salt. In this way the membrane increases in volume while isolating the silicate solution outside from the metal solution inside. At some point the membrane will breach and eject a plume of metallic solution. The outer silicate solution lowers the pH of the ejecting fluid and causes it to precipitate, forming a tubular structure composed of metal oxides and silicates. The color will depend on the metal salt used, just as the color of glass depends on the metal added. The material formed from this experiment will grow upwards, since the density of the ejected metal solution is lighter than the water glass, therefore forcing the tubes to grow upwards. The resulting morphology resembles that of a plant or a tree. Hence the name "chemical gardens".

The reaction has historically been a matter of great research interest. Apparently Isaac Newton developed an interest in chemical gardens during his work on the obsolete field of alchemy. He created "magic gardens in oil of sand" (waterglass), the organic appearance of the structures seemed to confirm the alchemical idea that metals had a life of their own and could vegetate.

In 1911 Stéphane Leduc wrote The Mechanism of Life [123]. He was convinced that the morphological similarities between chemical gardens and many organic formations were not a coincidence and that osmotic processes played an important role in the origin of life. He thoroughly experimented with different salts and solutions. He was able to reproduce the morphology of many plants, fungi and even seashells (see Figure 7.4).

FIGURE 7.4: Leduc's osmotic plants [123].

The rise of genetics discredited Leduc's ideas and brought a whole new set of theories on the origin of life. Chemical gardens were then regarded as a scientific curiosity and relegated to children's chemistry sets (see Figure 7.5a). In 1985 four high-school students won a competition organized by the U.S. space shuttle program and adapted this experiment to be performed in Space. The absence of gravity produced chemical gardens that grew out in random directions, tending to be twisted and in some cases forming spiral shapes [124].

The discovery in December 2000 [125] of the Lost City (hydrothermal field) brought new scientific interest on chemical gardens. The vents found in the hydrothermal field differ significantly from the black smoker vents found in the late 1970s. Black smokers are very acidic, with very high temperatures and chemically composed of iron, manganese and sulfur compounds. Fluid coming out of the Lost City vents on the other hand is alkaline (pH 9–11), has a much lower temperature (28–90^{o}C) and precipitates carbonate. The vents pump out water that has been drawn down into cracks in the ocean floor and heated to about 200^{o}C. As the fluids return to the cold ocean, calcium carbonate precipitates from the water. This process has been active for 30 000 years, building underwater towers as high as 60 meters that somehow resemble giant chemical gardens. In 2007 oceanographers reported finding abiotically produced organic compounds, including methane, in the water flowing from the vent [126]. All these conditions together

(alkaline water, not too hot, organic compounds) fit perfectly with current theories regarding the origin of life on our planet [127] and gives astrobiologists new information as to where life could emerge on other planets.

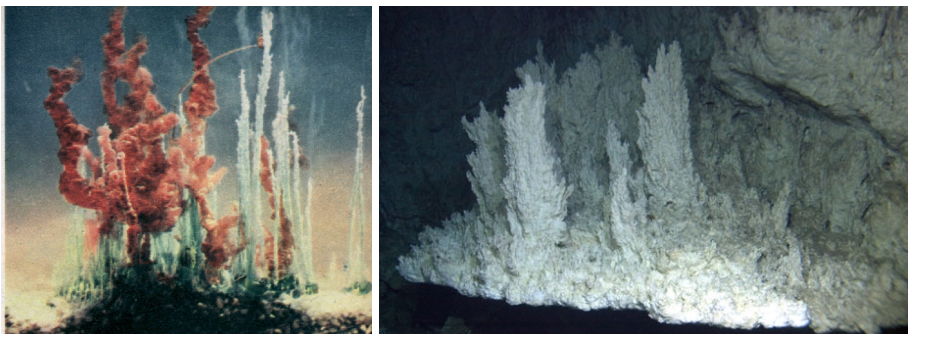

FIGURE 7.5: a)"Magic garden" grown from ferric chloride (brown) and nickel sulphate (green) as published in 1946 by a divulgative magazine [128]. The length of the tubes is ∼10 cm. b) Carbonate towers found in the Lost City hydrothermal field [116]. These are about 1 meter tall.

Chapter 8

Chemical gardens from silicates and cations of group II

8.1 Introduction

As mentioned above, chemical gardens are the plantlike structures produced by a variety of different metallic salts when immersed in a solution of one of a number of anions, the most investigated of which is silicate [129]. When the crystal of the salt begins to dissolve in the silicate it reacts and forms a gel around itself. This gel acts as a semipermeable membrane, inhibiting the outflow of ions from the salt but permitting water from the silicate solution to flow in towards the salt crystal driven by osmotic pressure. As the water flows and the crystal continues to dissolve the pressure inside the membrane rises. At some point, in general, the membrane ruptures and there forms a small hole through which the metal solution inside flows out. This metal solution reacts with the silicate outside; a tube around the flow growing by precipitation. The tube morphology is a product of forced convection driven by osmotic pressure owing to the semipermeable membrane and free convection from buoyancy, since the ejected solution is generally lighter than the external silicate. The final result is a combination of tubes of different sizes and shapes, resembling a tree or a garden.

Although chemical gardens are by no means a newly discovered phenomenon [122], this complex system combining different physical processes with chemical reactions of dissolution, precipitation, nucleation, crystallization and polymerization is not yet well-characterized in terms of understanding the physical and chemical parameters in order to be able to control the morphology, composition and microstructure of these tubes.

The main interest in the chemical-garden system has been for chemical demonstrations — which is somewhat ironic when the phenomenon is not fully understood — but it also

has relevance to processes of industrial importance that involve precipitation across a colloidal gel membrane separating two different aqueous solutions, for example the hydration of Portland cement [130] and the corrosion of metals [131]. It has also been proposed that the membranes of chemical gardens produced in submarine vents may be an ideal site for the origin of life [132].

While recent research has focused on controlling the tube growth itself [133], there is not much work that includes a thorough study of their morphology, chemical composition and microstructure. Traube [134] hypothesized the formation of the semipermeable membrane, which was later experimentally confirmed by Pfeffer [135]; Coatman et al. [106] studied the morphologies and rate of growth at different silicate concentrations; Collins et al. studied in detail the composition and structure of gardens grown from aluminum nitrate [136] and copper salts [137]; and Balköse et al. [138] used a wide variety of techniques to analyze the composition of gardens seeded with several metal salts. The formation mechanism and its relationship with microstructure and chemical composition is not yet well understood.

Thouvenel-Romans et al. [139] identified three different regimes of tube growth when injecting a copper sulfate solution into sodium silicate. At low concentrations of copper sulfate they obtained thin silica tubes growing steadily, which regime they called jetting. At intermediate concentrations the tubes grew wider and in a characteristic pulsating manner in which a droplet periodically forms and detaches at the tip of the tube, a regime they called popping. At higher concentrations they found a third regime, budding, in which the inflating droplet does not detach but instead bursts and nucleates a new droplet at the tube's end. The resulting morphology is of wider, globular and twisted tubes.

The purpose of this article is to study the morphology and composition of tubes grown with alkaline salts using different sodium silicate concentrations. For a more systematic investigation, we center the work on some cations of group II, Ca^{2+}, Sr^{2+}, and Ba^{2+}, which are especially interesting in the study of mineral formation and in the cement industry. The morphologies and microstructures were studied using ESEM and the compositional analysis was performed with energy dispersive X-ray analysis (EDX) and XRD.

8.2 Materials and Methods

To avoid initial conditions of different shapes, crystals of $CaCl_2$, $BaCl_2$ and $SrCl_2$ at analytical purity were generally homogenized with an agate mortar and pressed into 200 mg wafers of 1 cm diameter using a cell at a pressure of 10 bar during 10 minutes. This procedure permits a more uniform shape and a better control of the quantity and reactivity for these salts. In addition, in some cases indicated below, irregular grains were

also used. Sodium silicate solutions were prepared from a commercial concentrated solution composed of 27% SiO_2 and 15% NaOH. They were diluted using bi-distilled water to several concentrations between 6 M and 0.1 M. The growth process at room temperature was followed for at least 24 hours, or as long as necessary for the salt to completely dissolve. The experiments were recorded using standard photographic equipment. Afterwards, the tubes were removed from the solution and were dried in air at 25^oC. Micro-graphs of the samples were obtained using a FEI Quanta 400 Environmental Scanning Electron Microscope (ESEM) operating at high vacuum and room temperature. Chemical analysis of the micromorphology observed with ESEM was performed in-situ in the microscope using EDX analysis. Powder X-ray Diffraction (XRD) analyses were performed in a PANalytical X'Pert PRO diffractometer. The identification of crystallographic phases in the diffractograms was performed with the Xpowder program [140].

8.3 Results and discussion

8.3.1 Calcium Chloride

Initially we studied the growth process of silicate gardens from calcium chloride in different conditions with sodium silicate solutions at several concentrations from 6 M to 0.1 M. The reactivity and the behavior are dependent on the concentration of the silicate solution and the structure of the solid salt. After a short induction period, four kinds of behavior of the $CaCl_2$ salt can be distinguished: i) the formation of a transparent bubble as osmosis occurs, which we name an osmotic envelope; ii) the growth of wide transparent tubes with irregular globular forms from the osmotic envelope; iii) the growth of narrow white tubes from the osmotic envelope or from transparent tubes; and iv) the formation of a spongy mass.

The reactivity is much higher for salts in an irregular and porous grain form than in a compressed wafer. Obviously in the former the reactive surface is much larger; the higher porosity increases the dissolution rate in the grain compared to that in the wafer.

In Figure 8.1 we see the effect of different silicate concentrations on grains of $CaCl_2$. At high silicate concentrations (6 M and 3 M, with densities ρ = 1.39 g/cm^3 and ρ = 1.20 g/cm^3 respectively[141]), a large transparent osmotic envelope is formed during the dissolution of the salt. The internal pressure coming from the osmotic flow produces the expansion of the spherical osmotic envelope by a self-renewal process of the membrane under the stress of the internal pressure. When the osmotic envelope growth is almost finished, some closed-ended fingers grow in all directions (Figure 8.1a). This growth regime seems to be a diffusion-controlled one dominated by plastic deformation and elasticity of the membrane. The fingers are not more likely to grow upwards and the osmotic forces are more important than the buoyancy ones, fingers developing from

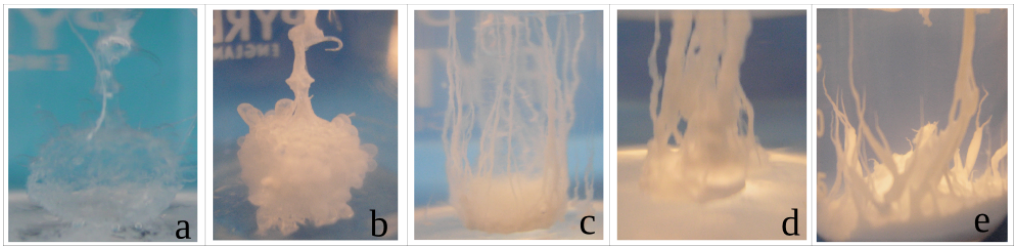

FIGURE 8.1: Chemical gardens from calcium chloride grown at 6 M (a and b), 2 M (c), 1 M (d) and 0.3 M (e) sodium silicate solutions. All pictures are in solution except b, which is without solvent. Picture size is approximately 2cm wide.

a Laplacian instability [142]. These fingers, about 1-2 mm in diameter, are easily observable when we remove the solvent (Figure 8.1b). When occasionally an air bubble appears on the tip of one finger, the buoyancy force of this air bubble facilitates the upwards growth of this finger in a 1 mm wide transparent tube in a popping growth regime [143] (see the central tube in Figure 8.1a). The strength and elasticity of the membrane inhibits the rupture of the osmotic envelope and sometimes when the salt is completely dissolved and the osmotic envelope is accidentally detached from the reactor bottom, the buoyancy forces push up the whole osmotic envelope to the top. We can estimate a concentration of calcium chloride of about 12% in the internal solution corresponding to a density of 1.10 g/cm^3[144], which is lower than the density of the external solution (ρ = 1.39 g/cm^3[141]). The transparency of the osmotic envelope, these fingers and its tubes, as well as its flexibility and elasticity, may be due to its extreme thinness and colloidal nature.

With a lower concentration of silicate, around 1 M (ρ = 1.06 g/cm^3[141]), the salts grow a collection of white narrow tubes (Figure 8.1d). No expansion of a spherical envelope is observed. Possibly the osmotic membrane, formed with lower silicate concentration, might be thinner so that it will break in many places by the buoyancy forces. The inner solution is expelled in a jetting growth regime, precipitating rapidly the silicate and forming the white tubes. Some intermediate behaviors are observed with silicate concentrations in the range 1–3 M where the reactivity seems to reach a maximum, with shorter induction times and longer lengths of tubes than with higher and lower silicate concentrations. In the example in Figure 8.1c, with 2 M silicate, a central wide transparent tube is formed initially and subsequently many white tubes grow out breaching the membrane around it. At silicate concentrations below 1 M, the salt dissolves forming a spongy mass in which no spherical membrane is distinguished. Many white tubes grow out very slowly and lean against the container wall, as seen in Figure 8.1e.

When using pressed wafers the reactivity is drastically lower, but the experiments become more systematic and reproducible. Use of the wafer also helps to avoid salt hydration during handling at ambient humidity. The general behavior starts with the

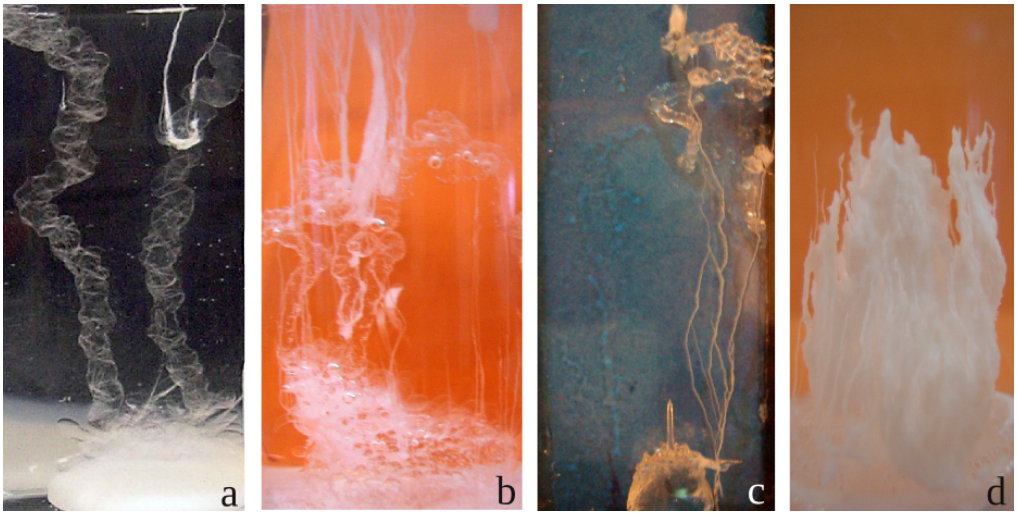

FIGURE 8.2: Chemical gardens grown from calcium chloride wafers in 3 M (a-c) and 1 M (d) sodium silicate. Gardens a) and b) were grown in cylindrical flasks, producing transparent tubes first and white tubes later. The experiment in figure c) was grown in a Hele-Shaw cell of width 5 mm. Picture size is approximately 2 cm wide by 5 cm tall.

formation of a gel membrane around the wafer, which then becomes the transparent osmotic envelope with 3 M silicate seen in Figure 8.2a–c. As the envelope inflates, it may trigger transparent fingers, wide transparent twisted tubes or narrow white tubes. Usually the wider tubes grow first in periodic pulses at about 3 cm/min following a budding growth regime, often changing direction with every burst. The narrow, white tubes do not appear until the wider tubes have stopped growing or when some external excitation (vibrations, shaking) occurs and the membrane breaks.

We propose that the formation mechanism of the transparent tubes is different to that of the white ones. The transparent tubes are not produced by a rapid rupture of the membrane, but by an elongation of the same membrane forming a finger and growing upwards owing to a combination of osmotic and buoyancy forces. This explains also the same transparency of the tube walls and bubble. The width of these tubes helps a slow and regular formation of the tube walls. When the osmotic and buoyancy forces are strong enough, the membrane of finger tip stretches and breaks concurrently with the formation of a new extension of the membrane with the flow of the inner solution. This extension of the walls increases the volume and the internal pressure is released. This produces a cessation of the flow closing the tip of the tube. Again the osmotic flow increases the inner pressure and the freshly formed membrane will be broken following a random direction and forming another segment of the membrane wall as explained

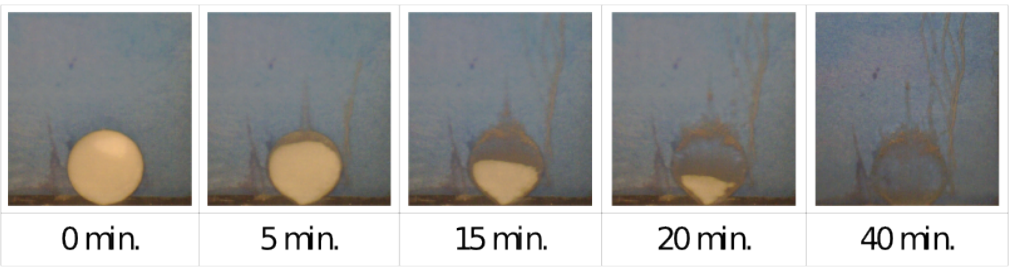

FIGURE 8.3: Calcium chloride wafer immersed in 3 M sodium silicate inside a Hele-Shaw cell of width 5 mm. Buoyancy forces produced by the different solution densities cause the wafer to dissolve from the top. Picture size is approximately 2 cm x 2 cm.

above. The budding growth tends to be periodic yielding bulging but unbranched, hollow tubes. These tubes will be more or less vertical depending the strength of the buoyancy forces.

The white narrow tubes can grow directly from the bubble or from the endings of wider tubes (Figure 8.2b) and always in a rather vertical manner indicating a greater influence of buoyancy forces, as opposed to the forced convection that produced the transparent tubes. After the formation of the spheroidal envelope and the transparent tubes, the concentration of calcium will be lower than in the initial solution owing to the entrance of water and the quantity of calcium used in the membrane wall formation. Hence the density difference between the internal and external solutions will be larger than in the initial situation and so the buoyant forces will be larger. These forces will try to break the colloidal membrane in any instability and the inner solution will exit forming the relatively more straight white tubes of about 0.2 mm in diameter in a jetting growth regime [145]. The color difference between the two types of growth may be explained by their different thickness, and also by the different interstitial water content or colloidal state [142], which would also explain the flexibility of transparent tubes versus the fragility and stiffness of white ones.

The influence of gravity can be observed in the sequence shown in Figure 8.3. In that case a calcium chloride wafer is immersed in 3 M silicate in a 5 mm wide Hele-Shaw cell. The salt does not develop a spherical bubble because of the restriction imposed by the walls, but it still forms a transparent membrane that permits us to see how the salt dissolves from top to bottom. The presence of gravity produces buoyancy forces between the different solutions and the salt wafer, which is still solid inside its osmotic envelope. The water that flows through the membrane is lighter than the inner metal solution which makes it accumulate above, dissolving the wafer from the top.

With 1 M silicate solution and wafers, the osmotic envelope size is much smaller than with 3 M and only white narrow tubes are formed (Figure 8.2d). As seen above, the

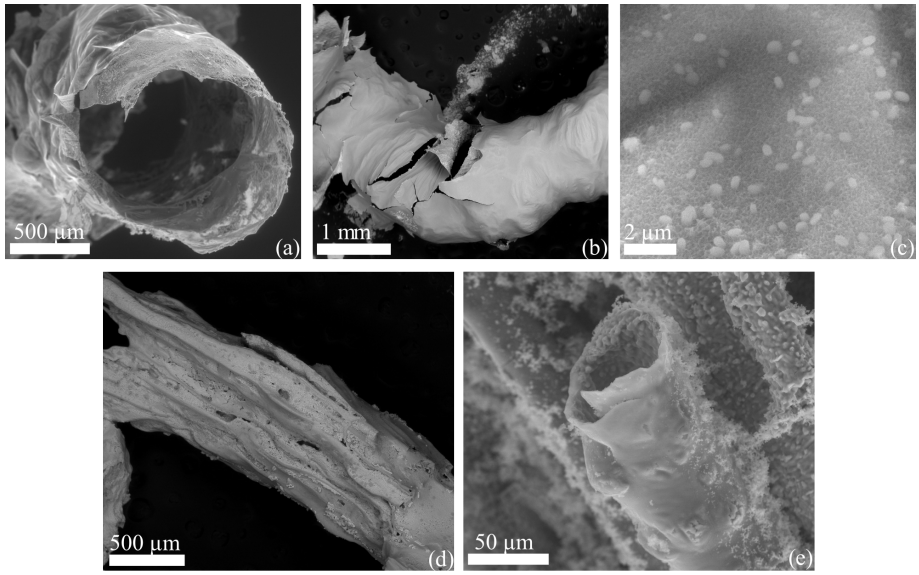

FIGURE 8.4: ESEM micrographs of the calcium chemical gardens grown from various experiments in 3 M sodium silicate. a) and b) are typical wide transparent tubes; c) shows undissolved calcium chloride crystals on the inner surface of a tube; d) cluster of disordered white tubes; e) the multilayer microstructure of a narrow white tube.

membrane formed with 1 M silicate breaks in many places and many jets of inner solution go upwards forming the white tubes. These tubes do not grow alone, but rather as a cluster of many microtubes. Probably the membrane is broken in many sites close to each other and this facilitates the formation of the disordered cluster of tubes. However, the origin of the different morphology of these white tubes with respect with the transparent ones is not well understood yet. Further experiments are necessary to understand properly this phenomenon.

In Figure 8.4a,b we show ESEM images of a typical transparent tube after it has been dried. We see how the surface textures are clearly different for the internal and the external sides of the tubes, smooth on the outside and rough on the inside. The elasticity is highly dependent on the water content, which is lost during drying producing many cracks on the surface (Figure 8.4b). EDX analysis indicates that the outer surface is mainly non-crystalline polymerized silica with calcium sodium silicate. The rough inner surface is composed mainly of calcium oxide with presence of $CaCl_2$ nano-grains in the lower growth zone (Figure 8.4c) and NaCl in the upper. The narrow, white tubes are forming clusters of nanotubes (Figure 8.4d), with multilayer walls (Figure 8.4e) and thicker external walls (>10 μm after drying) than the former transparent tubes (<1 μm after drying). Their composition is mainly calcium silicate on the outside, shifting towards calcium oxide in the inside. In some cases after long reaction times, some amount of calcium carbonate is detected particularly in the upper segments, probably

due to a small amount of carbonate in the medium from atmospheric CO_2 and owing to the low solubility of this carbonate at the high pH of the solution.

8.3.2 Strontium and Barium Chloride

The Sr^{2+} and Ba^{2+} salts were studied exclusively using wafers. In both cases the reactivity is lower than in the Ca^{2+} case at similar conditions, both in the induction time and in the formation of the osmotic envelope and tubes. While with calcium chloride the tubes grew steadily to a length of several centimeters, with strontium or barium salts the tubes grow to less than 1 cm. For strontium chloride with 1 M silicate solution the growth of the osmotic membrane is almost negligible and many short narrow white tubes form (Figure 8.5b). With 3 M silicate, a large transparent bubble is formed and a few wide transparent fingers slowly appear. After the growth of the fingers ceases, the membrane breaks and some white narrow tubes grow from the top surface of the osmotic transparent bubble (Figure 8.5a). When the inner pressure in the bubble decreases, the growth of the white tubes stops by closure of the tube-tops and new white tubes grow when the pressure has recovered in the osmotic envelope. In some essays, the cluster of white tubes can be so large that the osmotic envelope collapses by the weight of the cluster.

Barium chloride reacts more slowly in the formation of the osmotic envelope with 3 M silicate and has a longer induction time than the strontium salt. However, the verticality of the white tubes of Ba^{2+} grown with 1 M silicate is greater than in the strontium cases (Figure 8.5b,d). With 3 M silicate a cluster of short white tubes grows on the top-surface of the bubble, similarly to in the strontium case.

In the case of the white strontium tubes, their micromorphology shows a rough external surface covered by amorphous silicate aggregates and a smooth internal surface (Figure 8.6a). This is completely different than that found in the transparent tubes of the calcium case. EDX chemical analysis of the inner surface shows that it is composed of strontium oxide, while the outer surface is made of strontium silicate. In the course of this particular experiment we removed the osmotic envelope from the silicate while it still contained some undissolved salt inside. Analyzing the remains of the wafer (Figure 8.6b) by EDX and backscattering detector, the brightest regions are the original $SrCl_2$, but the darker ones are made of NaCl, proving the sodium cation may cross the semipermeable membrane. We also separated a piece of osmotic envelope and imaged it using a backscattered electron solid state detector (Figure 8.6c). EDX analysis of the outer surface of this membrane shows that it is formed mainly of strontium silicate (darkest areas), whereas the inner surface corresponds to the initial strontium chloride (brightest areas). Many nanospheres of silicate are observed in the inner surface of the envelope (Figure 8.7d,e). This microstructure is different to that of the external surfaces.

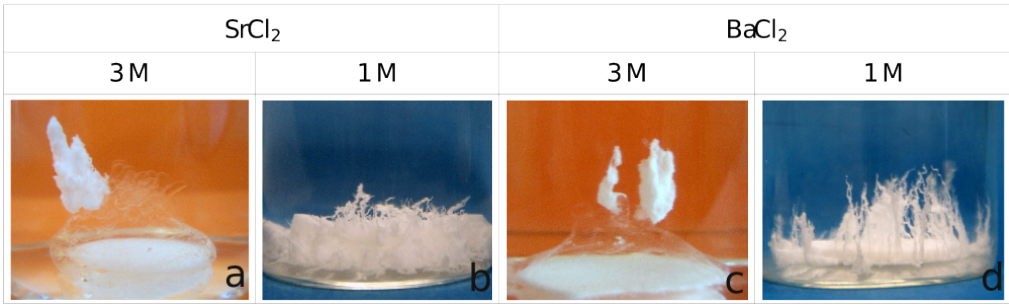

FIGURE 8.5: Chemical gardens of $SrCl_2$ and $BaCl_2$, at the indicated sodium silicate concentrations. Picture size is approximately 2 cm wide.

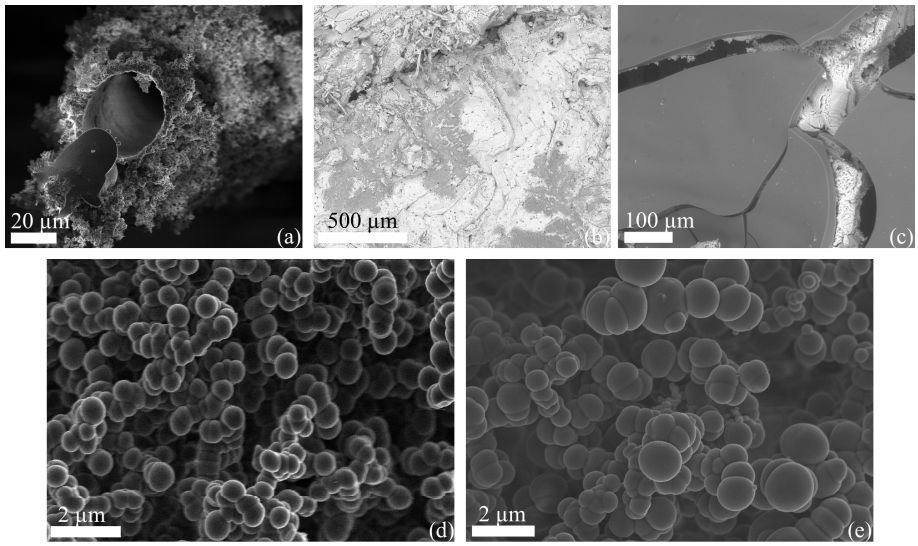

FIGURE 8.6: ESEM micrographs of a $SrCl_2$ garden grown in 1 M sodium silicate: (a) tube opening, showing the different morphology in the inner and outer sides; (b) piece of undissolved $SrCl_2$ wafer; (c) outer side of the osmotic membrane; inner surface of bubble in (d) $SrCl_2$ and (e) $BaCl_2$. The b and c pictures were taken by a backscattering solid state detector.

8.3.3 X-ray Analysis

In order to perform X-ray powder diffraction of the chemical garden, the tubes were separated from the rest of the sample to explore differences in the crystallinity and chemical composition between the various morphologies of different parts of the chemical garden. Calcium tubes did not show a high crystallinity except for NaCl crystals whose reflection peaks were the most intense and the only ones clearly observed at

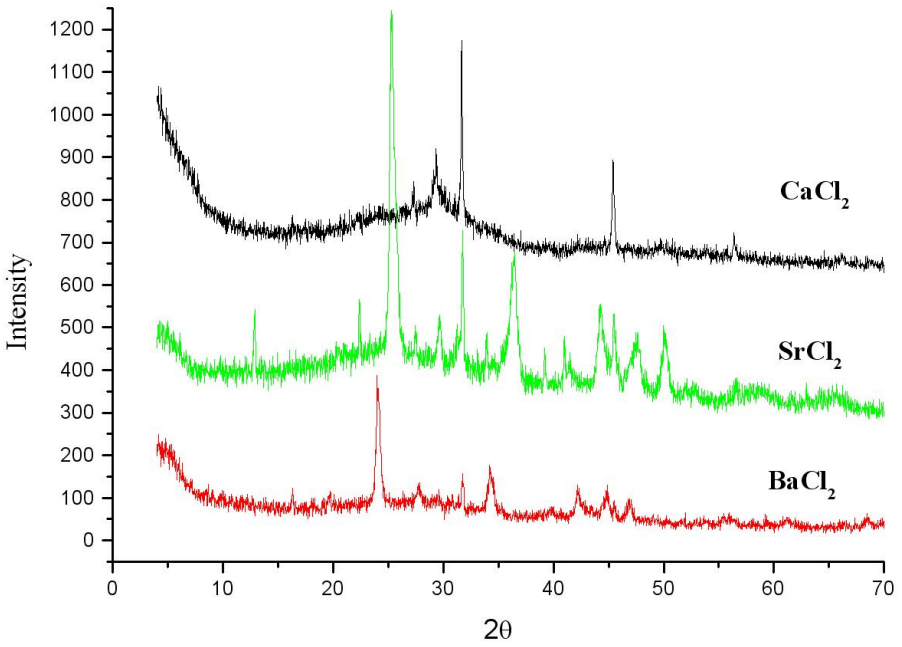

FIGURE 8.7: X-ray powder diffraction patterns of tubes grown from $CaCl_2$, $BaCl_2$ and $SrCl_2$. The different spectra were shifted up by 300 counts of intensity for clarity.

27.8^o, 31.8^o, 45.4^o and 56.5^o (2θ values) (Figure 8.7). Barium and strontium tubes, however, showed clear reflection peaks belonging to carbonates (Figure 8.7). In the barium spectrum, the peaks at 24.06^o, 34.18^o, 42.17^o, and 44.86^o (2θ values) belong to $BaCO_3$, there being observed also reflection peaks of NaCl. In the strontium spectrum, the peaks at 29.68^o, 36.46^o, and 47.71^o belong to $SrCO_3$, while those at 12.90^o, 22.38^o, 25.23^o, 33.91^o and 40.97^o belong to undissolved $SrCl_2{\cdot}6H_2O$, and peaks of NaCl are also observed.

This indicates that the only highly crystalline phases in these silicate gardens are NaCl and carbonates. The main phases are mostly silica and silicates in an amorphous or disordered state, which is well known in the formation of calcium silicate in Portland cements [130]. The formation of NaCl occurs mainly in the inner surface of the membrane and tubes and it is clear evidence that the Na^+ cations cross the osmotic membrane and form halite crystals with the chloride anion of the seed. The crystallization of carbonates is owing to their low solubility at the basic pH of the silicate solutions and to the presence of CO_2 in the atmosphere absorbed in the silicate solutions. The formation

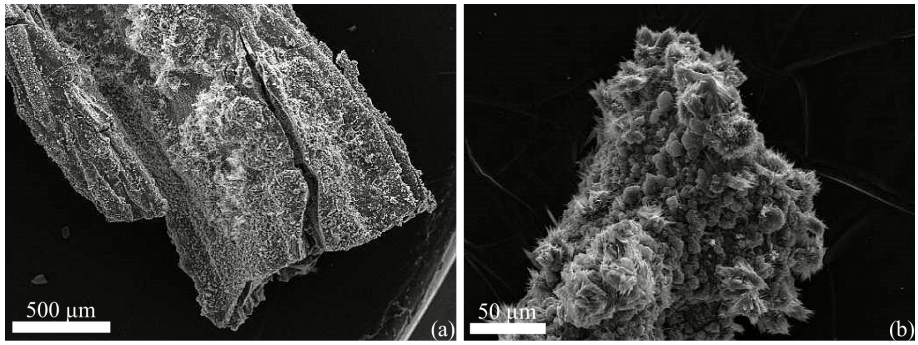

FIGURE 8.8: ESEM micrographs showing the formation of carbonate crystals on the surface of chemical gardens of (a) calcium and (b) barium. The clear spots are composed of carbonates and the darker zones are silicates.

of carbonates is more likely to be observed in the strontium and barium cases owing to their lower solubility. Some small needles of carbonates are observed by ESEM-EDX in the outer surface of the upper part of some white tubes in the calcium (Figure 8.8a) and barium (Figure 8.8b) cases.

8.4 Conclusions

We found $CaCl_2$ to be more reactive than the other salts of group II in terms of tube length, diameter and growth speed. Calcium tends to produce long, wide and flexible tubes, while strontium and barium produce short, narrow tubes that sometimes grow as clusters. The strontium salt is slightly more reactive than the barium one. This is consistent with the sequence of the relative solubility of these salts: $CaCl_2 > SrCl_2 > BaCl_2$. The optimal concentration for the sodium silicate solution in chemical garden growth with these salts is around 3 M, in good agreement with the findings of Coatman et al. [106]; higher and lower concentrations reduced the reactivity. The concentration of the solution affects the shape and rate of the formation of the tubes, in part presumably through its viscosity. With a higher viscosity (higher silicate concentration) the reaction is slower and the viscosity of the external solution allows only a few slow-growing tubes to emerge. At the other extreme, very dilute concentrations fail to produce a coherent colloidal membrane and the precipitated material forms a spongy mass. The reason is that at higher concentrations the thickness and elasticity of the membrane is great enough to allow it to expand and inflate without breaking. On the other hand, at lower concentrations with less silicate in the solution, the membrane formed bursts sooner ejecting the internal solution promptly and forming multiple white tubes instead of maintaining or expanding the transparent membrane.

Electron microscope imaging shows that tube walls are not homogeneous across their section. There is both a morphological and a compositional difference between the inner and outer surfaces. The different morphologies indicate that the tubes are formed by two separate layers, metal oxide on the inside and metal silicate on the outside. However, the separation between the layers is not clear and EDX analysis does not have enough resolution to verify this discontinuity. Probably the kinetics in the fast precipitation in the tube wall formation does not allow the formation of a clear interface, especially in the formation of white narrow tubes.

X-ray diffraction shows the tubes have low crystallinity and the amorphous components hide the highly ordered phases, nevertheless the highest crystallinity phase comes from the formation of NaCl. The presence of NaCl crystals in the inner surface of the tubes indicates that the Na^+ ions can cross the semipermeable membrane.

In some cases, we observe pulsating growth of wide transparent tubes producing irregular morphologies which are clearly influenced by the thickness and mechanical properties of the membrane. When the membrane first breaks, a jet of the internal solution flows out. The contact of this flow with the external solution produces the precipitation of the silicate of the group II cation, forming the walls of the tube. As the flow of metal solution loses its initial injection pressure the precipitation of silicate will close the tip of the tube, interrupting its growth. The osmotic membrane will then need some time to regain enough pressure to reopen the closed tube and continue its growth. In this way we have a relaxation-oscillation process, as described by Thouvenel-Romans et al.[139], with random changes of orientations at the top of the tube developing the twisted, globular shapes seen in the experiments. When the strength and elasticity of the membrane is sufficient, it does not break rapidly but it becomes deformed and the tubes can be considered as elongations of the own membrane preserving the same transparency. This behavior is only seen in the wider tubes formed with higher silicate concentrations, where we have stronger membranes that can accumulate higher pressures before bursting and hence produce greater flows of metallic solution. Thouvenel-Romans et al.[146] proved that there is a relation between the injection rate and the radius of the tubes, which explains why we do not see the wider pulsating tubes at silicate concentrations below 1 M.

Fine control of the fluid dynamics, the relative densities between the different solutions and the osmotic pressure could provide tools to engineer microtubes with desired morphology and thickness.

Chapter 9

Effect of the nature of the cations

9.1 Introduction

The purpose of this chapter is to study the formation, morphology and composition of tubes grown with various metallic salts ($CaCl_2$, $MnCl_2$, $CoCl_2$ and $NiSO_4$) using different sodium silicate concentrations. The morphologies were studied using SEM imaging and the compositional analysis was performed with EDX and XRD. An interesting difference in the behavior between the cations of the salts is noted. A better understanding of the physics and chemistry of these processes can improve the control of the relative solution densities, osmosis, and diffusion to obtain tubes with a desired morphology.

9.2 Materials and Methods

Crystals of $CaCl_2$, $MnCl_2{\cdot}4H_2O$, $CoCl_2{\cdot}6H_2O$ and $NiSO_4{\cdot}7H_2O$ at analytical purity and homogenized with an agate mortar were used for our experiments. They were pressed into 200 mg wafers of 1 cm diameter using a cell at 10 bars pressure during 10 minutes. The use of the wafer permits more systematic and reproducible experiments, avoiding different shape initial conditions and, in the case of $CaCl_2$, it helps to inhibit salt hydration during handling at ambient humidity. Nevertheless, irregular grains of these salts were also used in some cases. The sodium silicate solutions were prepared from a commercial concentrated solution composed of 27% SiO_2 and 15% NaOH. They were diluted using bi-distilled water to several concentrations between 6 M and 0.3 M. The growth process was followed for at least 24 hours at room temperature, or as long as necessary for the salt to completely dissolve. The experiments were recorded using standard photographic equipment. After that, the tubes were removed from the solution and were dried in air at 25°C.

The micrographs of the samples were obtained using a FEI Quanta 400 environmental scanning electron microscope (ESEM) at high vacuum and room temperature and a LEO GEMINI-1530 field emission scanning electron microscope (FESEM). Chemical analysis of the solids was performed in-situ in the microscope using EDX analysis. Powder X-ray diffraction (XRD) analyses were performed in a PANalytical X'Pert PRO diffractometer with a wavelength of 1.5418 Å. Single crystal X-ray diffraction analyses were performed in a SIEMENS P4 diffractometer with a wavelength of 0.7107 Å. In order to perform X-ray powder diffraction, the tubes were separated from the rest of the garden to avoid the amorphous pattern given by the remains of the osmotic membrane. The identification of crystallographic phases in the diffractograms was performed with the Xpowder code [140]. The treatment of data from single crystal XRD was performed with XRD2DScan code [147].

9.3 Results

We studied the growth process for all four salts at different silicate concentrations. In this series we explore cations with different electronic properties. All these cations belong to the same period of the periodic table: one of the group II and several transition cations with different electron population in the valence shell following the sequence: Ca $<$ Mn $<$ Co $<$ Ni. We found a similar tendency but different behavior for the four salts with respect to the change of silicate concentration. At high concentrations, higher than 2 M and 3 M, just one or two tubes grow. Depending on the seeding salts, these tubes may grow steadily or in a pulsating manner to a length of several centimeters. At lower concentrations, around 1 M, the salts grew a collection of multiple narrower tubes. We also found lower reactivity at these low concentrations, so the tubes showed a longer induction time to start growing and did not grow for so long. This difference could be due to the mechanical properties of the silicate membrane formed around the crystal salt in the first place: more concentrated silicate solutions produce more resistant membranes, and so they hold more water inside and at higher pressures before rupturing.

Calcium Chloride

Gardens grown from calcium chloride show two very distinct growth regimes at high and low silicate concentrations. The general behavior starts with the formation of a gel membrane around the wafer, which then becomes the transparent osmotic envelope. At highest concentrations of silicate (6 M), the high density of the outer solution produces a weak osmotic pressure and a low reactivity, so usually only one transparent wide tube grows out of the membrane. With 3 M silicate, the salt grain is more reactive and the transparent membrane inflates by intaking water from the silicate under osmotic

pressure until it becomes a transparent elastic spherical envelope. The envelope's walls can be as thick as 1 μm and it may take from 5 to 15 minutes to burst open and for the first tube to grow. As the envelope inflates, it may trigger the growth of transparent fingers, wide transparent twisted tubes or narrow white tubes. Usually the wider tubes grow first, with a diameter of 1 to 3 mm. They grow in periodic pulses induced by the pressure oscillations in the osmotic envelope, with a period that can range from under one second up to one minute, following what Thouvenal-Romans et al. designate the budding regime [146], often changing direction with every pulse. This regime only allows one or two tubes to grow, the tubes being the widest of all salts studied here and growing rather fast, around 3 mm per minute. When the growth of these tubes is finished, narrow white tubes start growing from these transparent tubes (Fig. 9.1a). In general, all transparent forms turn white after one day or more; probably layers of silicate are depositing slowly during the aging time. At lower concentrations, around 1 M, the seeding salt fails to develop an observable osmotic envelope as it does at higher concentrations. Instead, multiple narrow tubes grow straight out from the initial salt. These tubes are all narrower than 1 mm and grow together by the hundreds in a tightly bound opaque cluster. As the silicate is more diluted, the growth rate of these narrow tubes is much slower, about 1 mm per minute. The fact that these tubes appear white – instead of transparent – may be a consequence of their narrow diameter, thicker wall and multiple clustering of tubes. There is no compositional difference with those from more concentrated silicate, as we shall see below (Fig. 9.1b).

We used electron microscopy at low vacuum to analyze the morphological differences between the regimes of jetting and budding. In the case of 3 M silicate, we measured diameters from 500 μm to 1 mm, with wall thicknesses from 1 to 10 μm (Fig. 9.1a) for the transparent budding tubes. The appearance of the external surface under SEM microscopy presented evidence of the tube flexibility during growth. The surface textures were clearly different for the internal and the external sides of the tube, being smooth on the outside and rough on the inside (Fig. 9.1d). EDX analysis on both sides shows a much higher proportion of oxygen on the inside, indicating the presence of CaO along with $CaSiO_3$. Analysis of the external side shows more Si, indicating that the external wall-surface is composed mainly of $CaSiO_3$. We also found crystals of NaCl ($\sim 1\mu$m), especially on the inside surface of the tube walls, which implies that Na^+ ions can also cross the osmotic membrane. We detected the presence of small crystals of $NaSiO_3$ on the external surface arising from the evaporation of the external solution (Fig. 9.2a) and the presence of SiO_2 attached to the external surface of the tubes after aging (Fig. 9.2b).

X-ray diffraction analysis of calcium tubes did not show any significant crystallinity except for NaCl reflections, indicating according to our previous work [148] that the microstructure is mainly disordered.

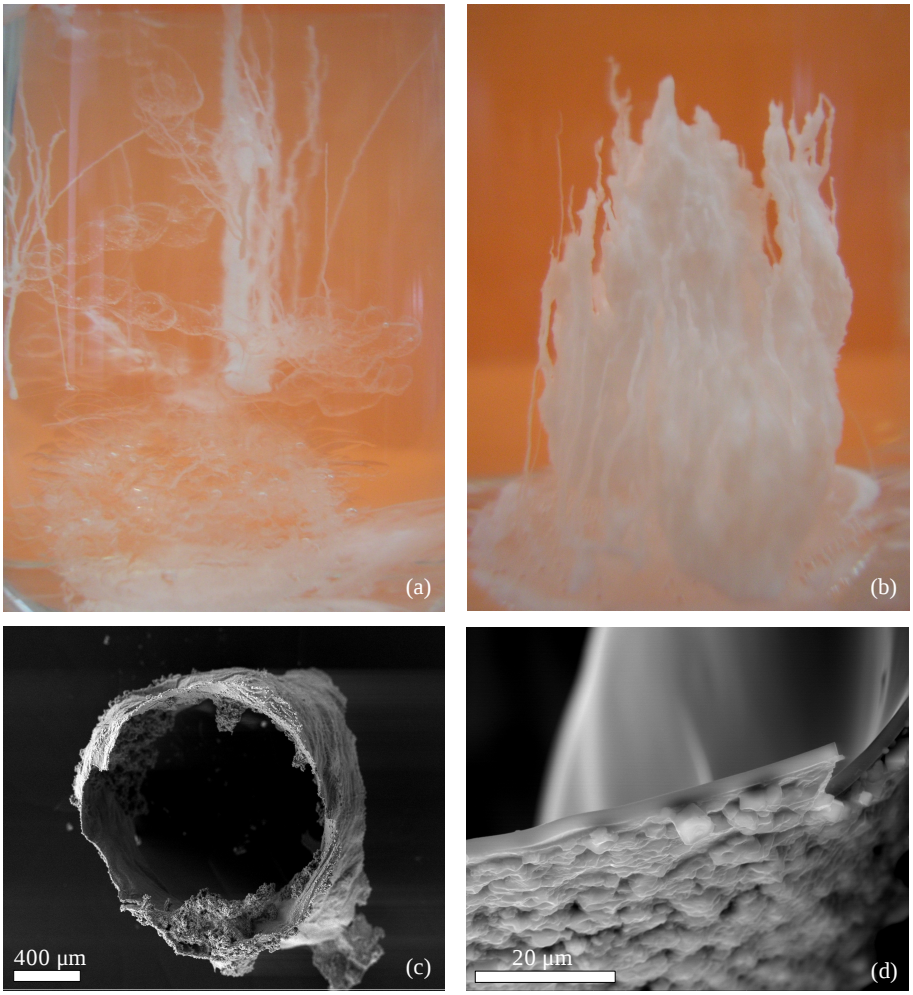

FIGURE 9.1: Growth of calcium chloride gardens with (a) 3 M and (b) 1 M silicate. Pictures are approximately 3 cm wide. c) SEM image of a $CaCl_2$ tube grown in 3 M sodium silicate, with a wide section and thin flexible walls. d) External (smooth) and internal (rough) surfaces of the tube wall; NaCl crystals are observed at the internal surface.

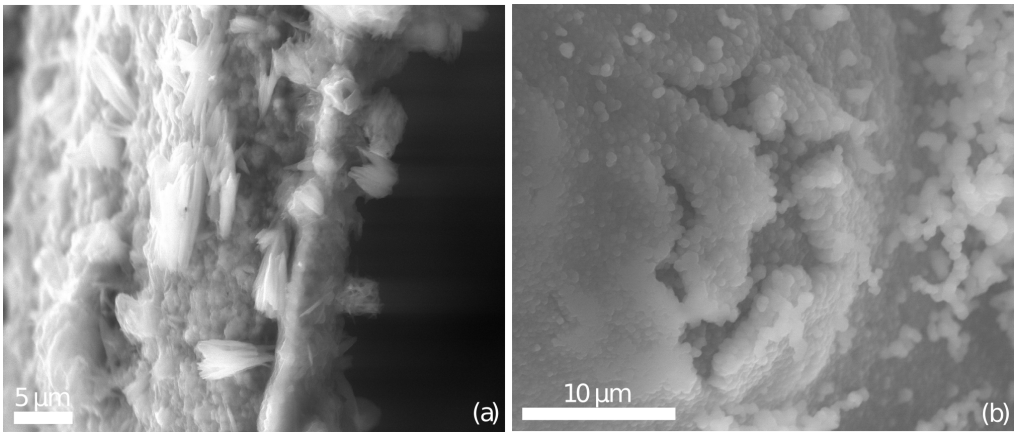

FIGURE 9.2: SEM images of external surface of $CaCl_2$ tubes grown in 3 M silicate. The external surface sometimes presents crystal flakes of sodium silicate (a) grown during the drying process or some SiO_2 particles (b) attached during the aging time.

Manganese Chloride

Manganese chloride has generally a slightly greater reactivity than calcium chloride with some differences. With 6 M silicate the reactivity is much lower than in the calcium case. Nevertheless, the presence of an air bubble enhances this reactivity. The buoyancy forces push up the air bubble and the surface tension of the water facilitates the contact of the membrane with the air bubble. Hence a wide translucent straight tube is formed following the trajectory of the air bubble through the high-viscosity silicate solution. With 3 M silicate only one or two wide tubes are formed following a budding regime [146]. In this case, the osmotic envelope is very small, the wide tubes are translucent with an ivory color instead of transparent and they are less wide than in the calcium case. When the growth of these budding tubes is interrupted (Fig. 9.3a,b) the osmotic envelope continues growing and later new narrow opaque tubes begin growing from the previous ones. Some fingers growing directly from the osmotic envelope were also observed (Fig. 9.3c,d).

With 2 M silicate, wide budding tubes also grow and the reactivity is higher than in the above case (Fig. 9.3e). When immersed in 1 M silicate, the reactivity is the highest for the Mn series and narrow opaque tubes grow grouped in clusters (Fig. 9.3f). They grow more vertically than the above budding tubes and with a faster rate, approximately 5-6 mm per minute. No osmotic envelope is observed, though the wafer seems to swell slightly and the wafer is empty inside at the end of reaction. This enhancement of reactivity is also observed when the wafer contacts with the reactor walls and a group of tubes grow faster attached to the reactor wall. With 0.6 M silicate, the morphology is similar to that at 1 M but with a lower reactivity.

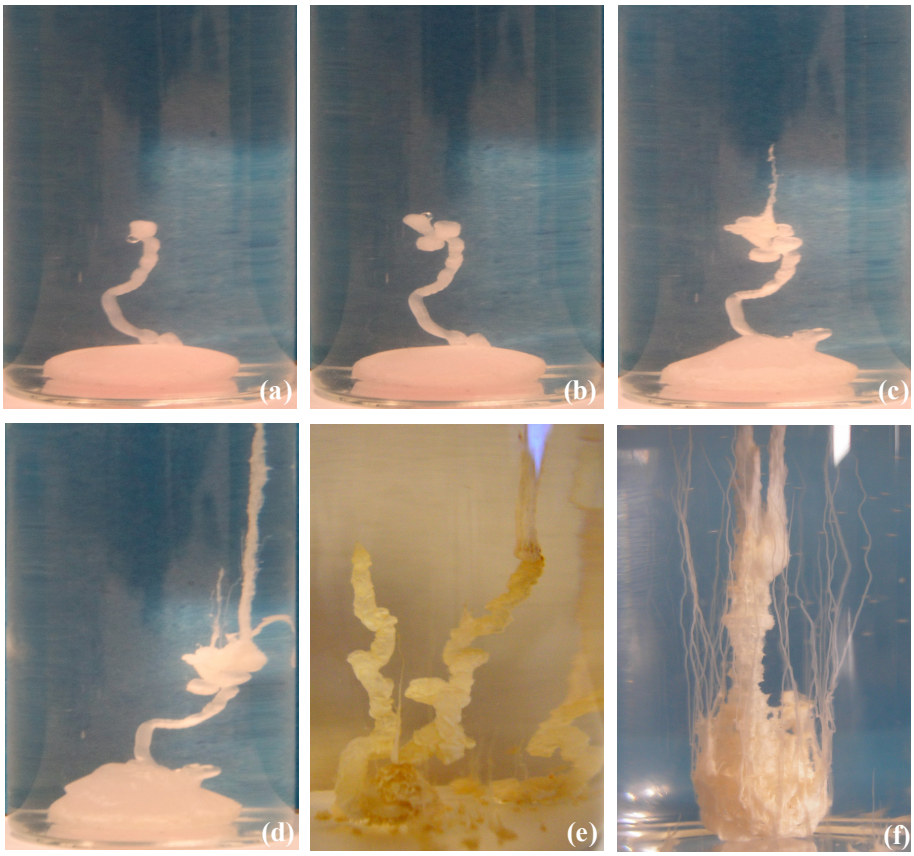

FIGURE 9.3: Manganese chloride gardens growth in sodium 3 M (a–d), 2 M (e) and 1 M (f) silicate concentrations. Pictures are approximately 3 cm wide.

In all manganese series, the initial pale-rose color of the wafer turns to a white-ivory color in the osmotic envelope and the tubes and after one day these solids turn brown. At the end of the garden formation the interior of the wafer is dissolved, the wafer becomes empty and only the external surface is maintained. For both salts, calcium and manganese, the budding regime of tube growth is observed with high concentration of silicate dissolution ($>$2 M) and the narrow opaque tubes grow with more dilute silicate. However, the behavior is different for each salt. The highest reactivity is in 3 M silicate for calcium whereas it is in 1 M silicate for manganese. The osmotic envelope is larger for calcium than for manganese with concentrated silicate ($>$2 M) with more water entering the inner solution. On the contrary, the mechanical stability of the gardens is higher for manganese than for calcium with dilute silicate ($<$1 M).

In figure 9.4a we show the micromorphology of the budding tubes grown in 3 M silicate.

Like in the calcium case, the outer texture of the budding tubes is smooth showing evidence of their flexibility when fresh whereas the inner surface is rough. EDX analysis indicates the presence of manganese silicate on the outer side and manganese oxide-hydroxide on the inner. In the inner surface of the tubes which are close to the bottom near the osmotic envelope a significant amount of manganese chloride is detected. Typical tube diameter is $\sim$1 mm, with wall thickness of $\sim$10 μm. The micromorphology and chemical composition is similar for the budding tubes grown in 2 M silicate. In figure 9.4b we can observe the irregular morphology of a budding tube, which presents a rough inner surface and a smooth outer surface. The texture of the narrow opaque white tubes grown in 0.6 M is different to the previous budding translucent tubes. The walls of the isolated opaque narrow tubes are thicker (40–60 μm) than the budding ones (Fig. 9.4c,d). In these opaque narrow tubes the interfaces between layers with different chemical composition are sharper than in the tubes with a budding regime. By means of a backscattering detector, we can distinguish the brighter zones of manganese oxide-hydroxide and the external dark zone of silicate (sodium and manganese) and silica (Fig. 9.4c). These layers are not chemically joined to one other and they separate from each other after drying (Fig. 9.4d). The wall thickness is greater in the tube clusters than in the isolated tubes. EDX chemical analysis indicates that the interstitial zone between tubes in the clusters is formed mainly by sodium silicate.

The manganese series produces higher crystallinity than the calcium gardens. We identified manganese hydroxide crystals in most experiments (Fig. 9.5). In the budding tubes the main crystalline component is $MnO \cdot H_2O$ with peaks at 18.7^o (001), 31.1^o (100), 36.6^o (101), 49.9^o (102), 55.4^o (110) and 58.9^o (111) (2θ units) (Fig. 9.5a), whereas in the opaque clusters of narrow tubes we detected crystals of NaCl (reflections at 31.8^o (200), 45.6^o (220), 56.4^o (222) and 66.3^o (400), hydrated $MnCl_2$ (reflections at 15.5^o (011), 16.5^o (110), 30.1^o (112), 32.1^o (031), 37.6^o (040), 51.4^o (223), 54.2^o (114)) (Fig. 9.5b,c) and a small proportion of $MnO{\cdot}H_2O$ (Fig. 9.5b).

In order to explore the crystallinity and ordering of the crystals in the tubes, we analysed an opaque cluster of tubes with a length of 3 cm directly by single-crystal-XRD. Two zones were analyzed, the center and the border of the cluster. The two-dimensional patterns of both zones show uniform distribution of the reflections indicating the small size and random orientation of the crystals. In the border of the cluster, some big bright spots are observed indicating the existence of bigger crystals in this zone. The analyses of both zones show similar composition being mainly manganese oxide-hydroxide and MnCl(OH)*n* (Fig. 9.6).

Cobalt Chloride

Cobalt chloride shows a similar dependence with silicate concentrations: wide tubes at high silicate concentrations and narrow tubes at lower silicate concentration. In general, the cobalt salt is much more reactive than the calcium and manganese ones.

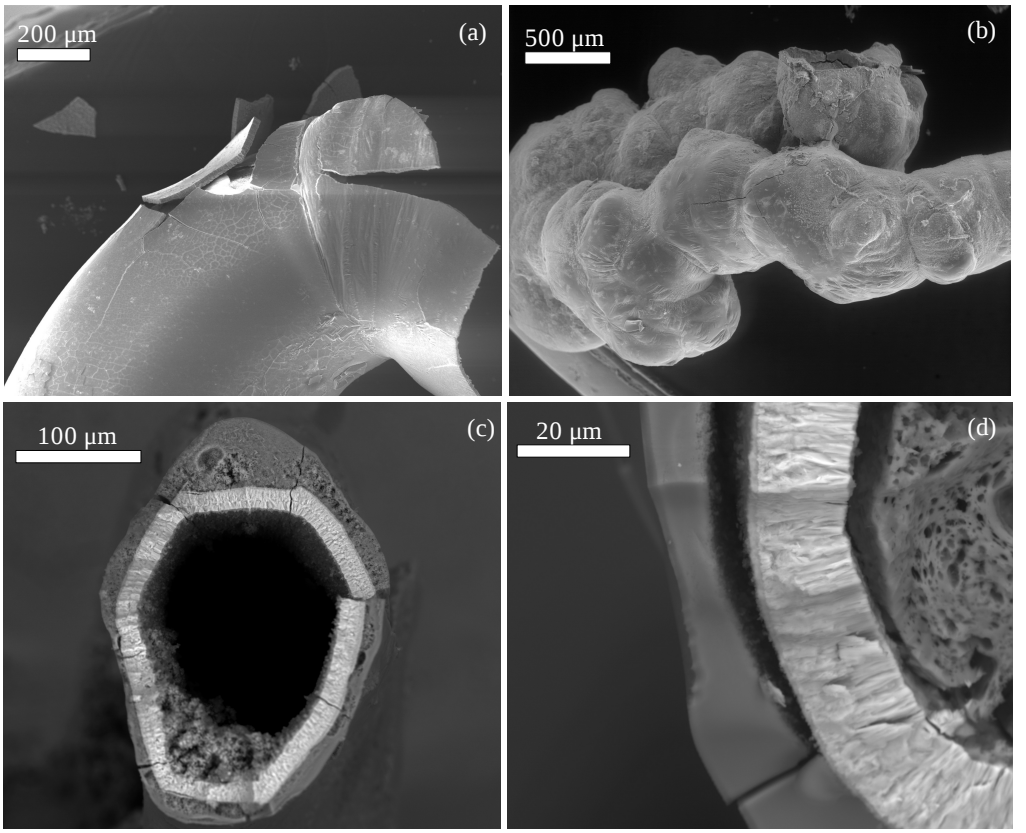

FIGURE 9.4: Budding tube grown from $MnCl_2$ in 3 M (a) and 2 M (b) sodium silicate. Straight narrow tube grown from $MnCl_2$ in 0.6 M sodium silicate. Pictures (c) and (d) were taken using a backscattering solid state detector.

In Fig. 9.7 we follow in detail the growth sequence of one particular cobalt tube in 3 M silicate. We cannot observe the formation of a clear osmotic envelope around the wafer at the beginning, although at the end the wafer is hollow. The presence of an air bubble facilitates the generation of a straight wide tube at a rate of 1 cm/min since buoyancy forces are important [143]. The wafer and the initial part of the tube is purple but the top of the tube becomes green. After a while the air bubble disappears, the growth stops and later the tube continues growing with a blue color. The growth stops again and a small envelope is formed on the top of the tube, from which clusters of narrow blue tubes grow together. As the cluster continues growing, the accumulated weight bends the original tube until it leans against the flask. When this fiber reaches the top surface, small green budding tubes grow along the top surface of the wafer and a plume of clusters of blue narrow tubes starts growing from these budding tubes and from the rim of the wafer.

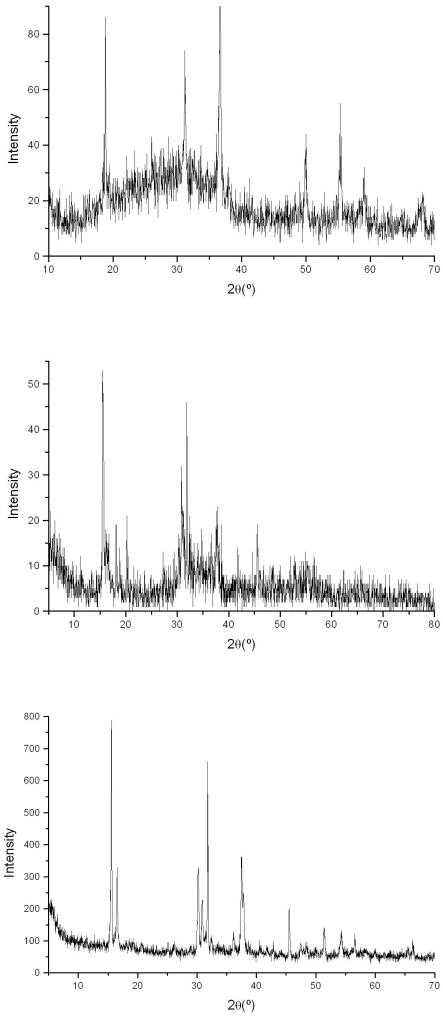

FIGURE 9.5: X-ray powder diffraction patterns of tubes grown from $MnCl_2$. Budding tubes (a), cluster of straight narrow tubes (b) in 2 M silicate. Tubes grown from wafers in 3 M (c).

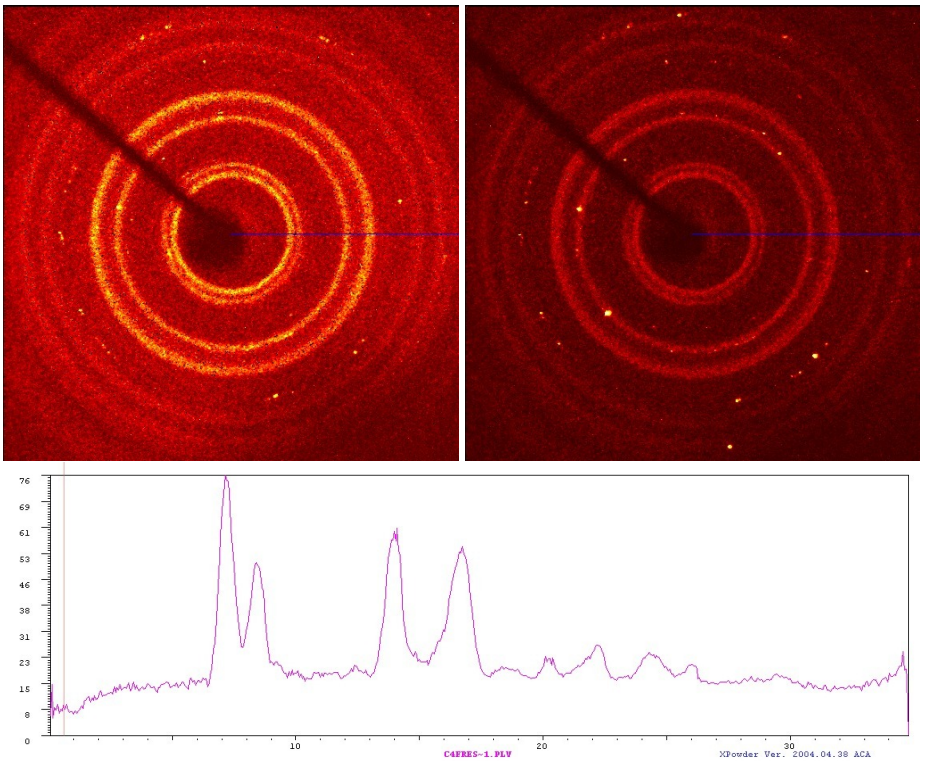

FIGURE 9.6: X-ray diffraction of one tube grown from $MnCl_2$ in 2 M silicate. Two-dimensional XRD pattern in the center (a) and in the border (b) of the tube. 2-θ scan integrated from the 2D pattern of the center of the tube (c). (λ(Mo) = 0.7107 Å)

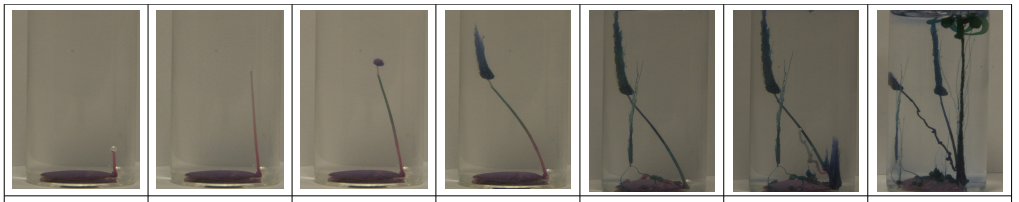

3 min.	4 min.	6 min.	8 min.	10 min.	25 min.	40 min.

FIGURE 9.7: $CoCl_2$ garden grown in 3 M sodium silicate. Pictures are approximately 3 cm wide.

In all wafers the tubes start growing at the rim of the wafer, where probably the instabilities are more frequent. Starting from irregular grains, the reactivity is higher than with the pressed wafers. At high concentrations of silicate (6 M and 3 M) the growth of tubes with budding regime is observed at the first stage of the reaction. At lower concentrations of silicate (1 M and 0.6 M), clusters of narrow tubes are formed. Notice that with very diluted silicate solution (0.3 M), the reactivity is lower and individual narrow tubes are formed with a budding regime (see Fig. 9.8).

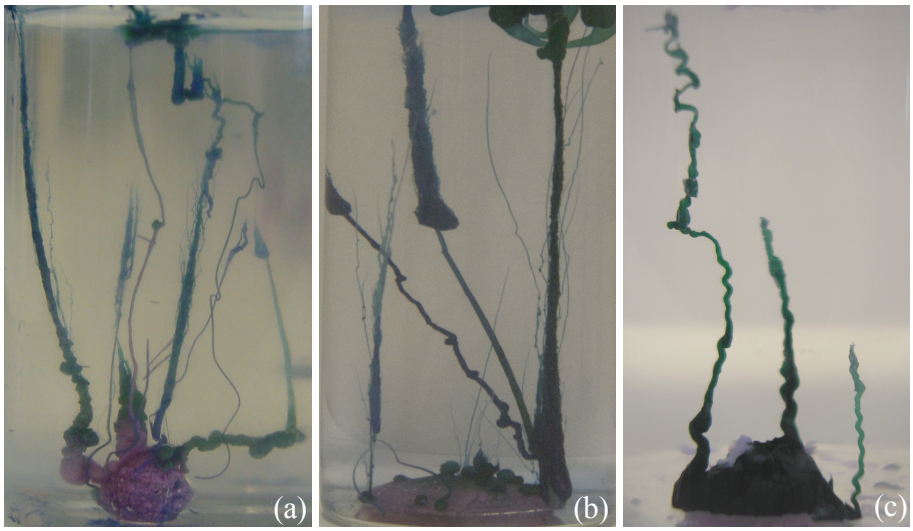

FIGURE 9.8: Comparison of different growths of $CoCl_2$ gardens in 6 M (a), 3 M (b), and 0.3 M (c) silicate. Pictures are approximately 3 cm wide.

In Fig. 9.9a we can see SEM imaging for the cluster of tubes explained above. It is composed mainly of dozens of tubes with individual diameters under 100 μm. In figure 9.9b we observe tubes growing from spheres formed on the top of the wafer surface at the first stage of growth forming a cluster of many tubes growing up. The tubes grow along the surface of the neighboring tubes, probably capillarity favors this kind of growth instead of the formation of isolated tubes. The texture is different in the outer and inner part of the tubes, being smooth outside and rough in the inner surface (Fig. 9.9c). The chemical composition is different being mainly cobalt silicate in the outer layer and cobalt oxide-hydroxide in the rough inner layer. In this inner surface many spheroidal rosettes of crystals are observed being formed of cobalt oxide-hydroxide and chloride (Fig. 9.9d). This morphology has been also detected in other cobalt oxides [149].

X-ray diffraction showed that these tubes are mostly disordered in their microstructure. Only in some cases we found cobalt hydroxide crystals (Fig. 9.10); with reflections at 19.0^o (001), 32.4^o (100), 37.9^o (101), 38.6^o, 51.3^o, 57.8^o (110), 61.4^o, 69.4^o, and 71.2^o

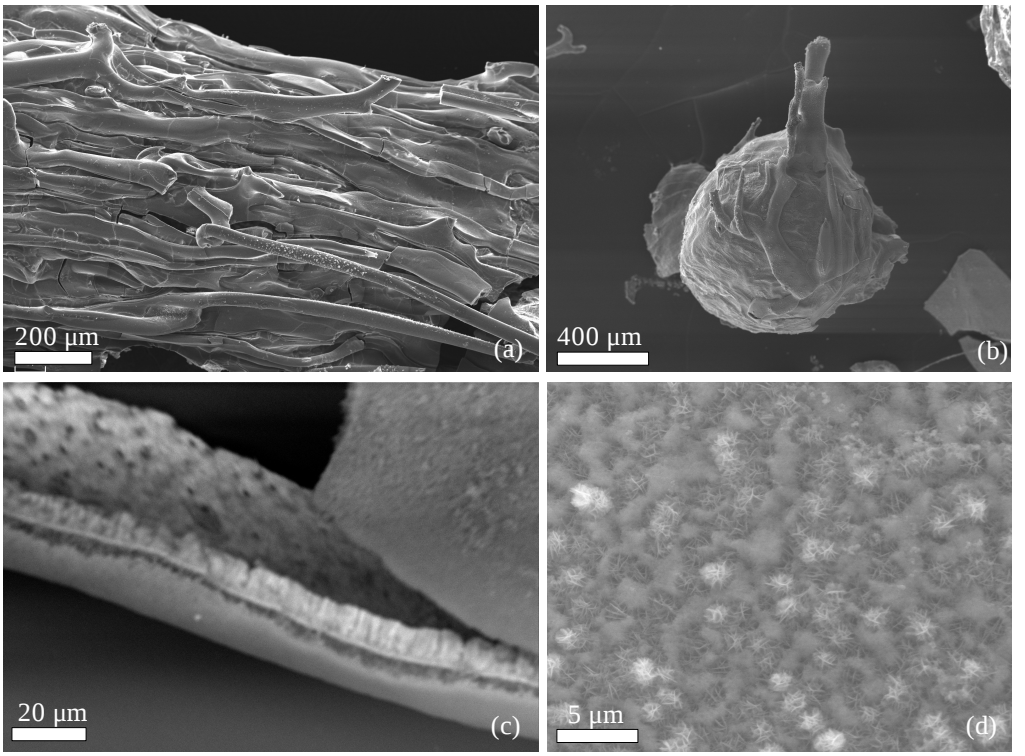

FIGURE 9.9: Cluster of narrow tubes grown from $CoCl_2$ in 3 M sodium silicate (a). Tubes growing from spheres on the wafer surface in 3 M silicate in a starting stage (b). Tube wall grown from $CoCl_2$ in 1 M silicate (c) and a detail of the inner surface of tube (d).

(2 θ units) (Fig. 9.10b). In some tubes, crystals of NaCl can be detected with reflections at 27.5^o, 31.8^o, 45.4^o (Fig. 9.10a). This band is not observed in the other salts.

Infrared analysis of cobalt tubes grown in 1 M silicate shows an intense narrow peak at 3551 cm^{-1} characteristic of ν(OH) of CoOH groups [150] indicating the presence of $Co(OH)_2$ (Fig. 9.11).

Nickel Sulfate

Nickel sulfate displays the lowest reactivity of all the studied salts, but produces the most robust tubes with the thickest walls. The behavior does not vary much with silicate concentrations. With highly concentrated silicate, narrow isolated straight tubes grow vertically upwards. Some of these tubes show a capsule at the top, probably covering an air bubble that facilitates the growth (Fig. 9.12a). With 3 M silicate, these

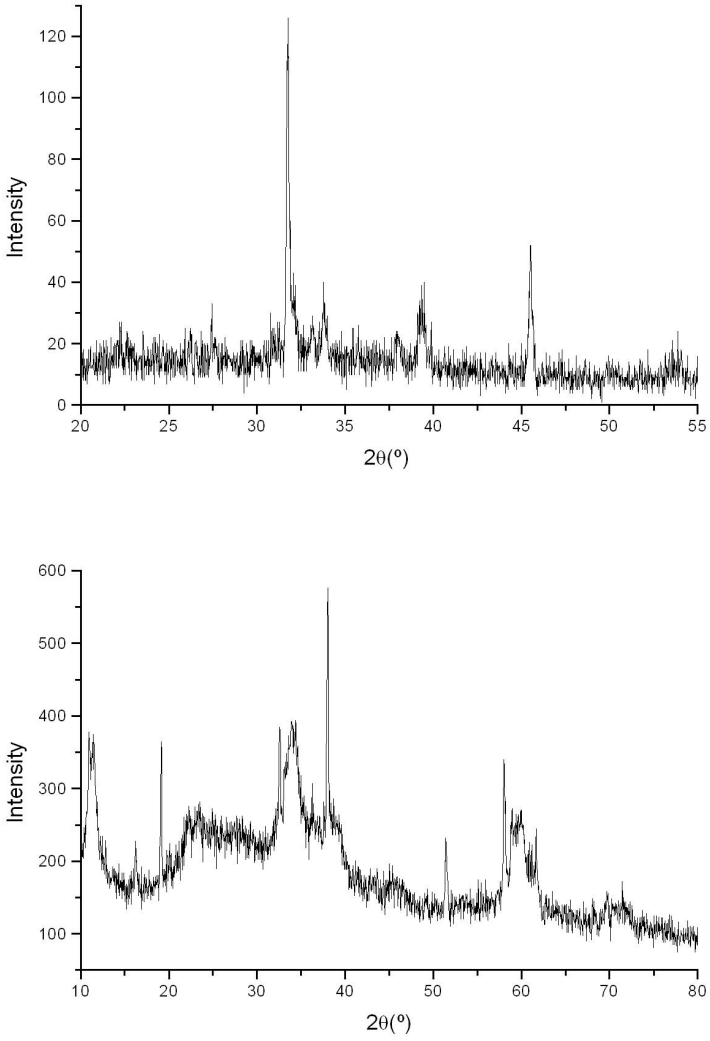

FIGURE 9.10: XRD analysis of cobalt tubes grown in 1 M (a) and 0.6 M (b) silicate.

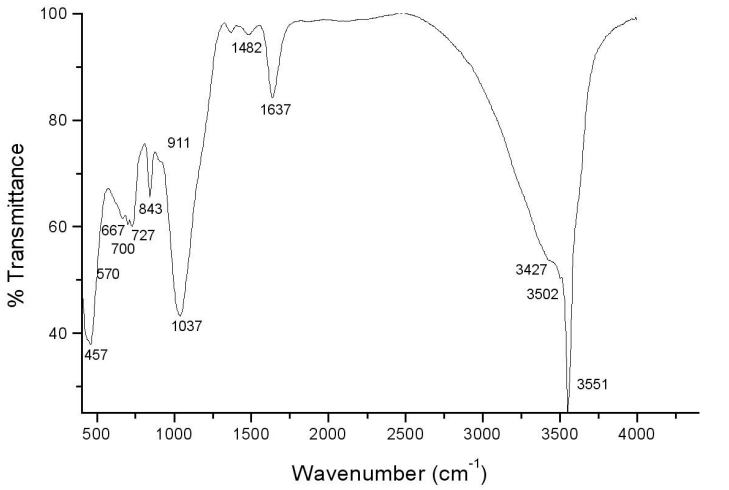

FIGURE 9.11: Infrared spectrum of cobalt tubes grown in 1 M silicate.

narrow isolated tubes grow but forming a curve starting upwards and later bending to a horizontal direction; probably the buoyancy forces are not strong enough for a vertical up-growing (Fig. 9.12b). With more dilute silicate (<2 M), these isolated tubes are not formed, but instead an irregular cluster of tubes (Fig. 9.12c). As in the previous series, pressed wafers are less reactive than irregular grains of the salt. In wafers, we observe that the borders are more reactive than the other zones of the wafer. The osmotic envelope is not observed and the increase in volume of the wafer is smaller than in the previous series. Initially a short and relatively wide budding tube grows with light-green color that later continues growing as a possible jetting regime forming an isolated tube that does not grow vertically but curves probably because the buoyancy forces are not strong enough (maybe owing to a lower density difference) for straight vertical growth. Later some wide tubes grow along the surface of the wafer from the borders to the center from where a wide cluster of tubes grows straight upwards. Capillary forces facilitate the growth of tubes attached to the external wafer surface. When the amount of water increases in the inner solution, the density of this inner solution will be lower and the buoyancy forces will be enough for the up-growth of the tubes attached to each other by capillary forces. When this tube reaches the top surface of dissolution, additional similar tubes start growing from the wafer.

In highly concentrated silicate, small budding tubes are formed in the initial state, whose micromorphology shows that they are highly twisted (Fig. 9.13a). The narrow isolated tubes grown at 6–3 M silicate can be of 200 μm diameter and show a smooth outer surface (Fig. 9.13b). In figure 9.13c we can see the remains of the osmotic membrane.

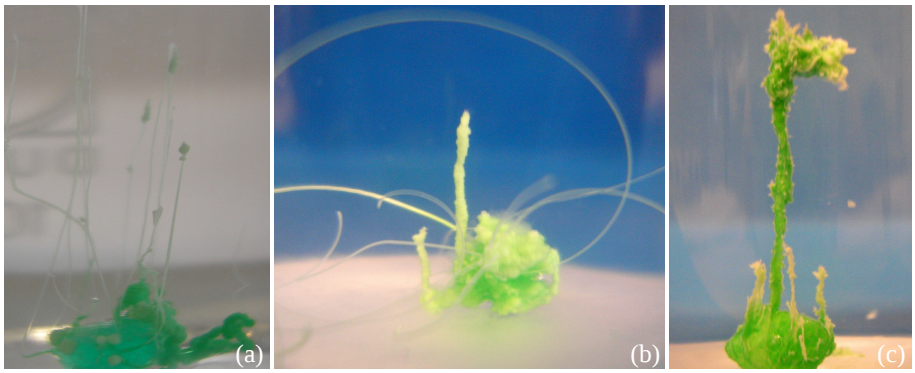

FIGURE 9.12: Nickel sulfate gardens growing in 6 M silicate (a), 3 M silicate (b) and 1 M silicate (c). Picture size is approximately 3 cm wide.

It is ∼50 μm thick and is still covered with a layer of silica on the outside. Its inner surface is scattered with hollow spheres of 20–120 μm diameter and thin walls (approx. 1–5 μm) that can be broken during the drying process or under the high vacuum of the microscope. These hollow microspheres appear also on the inner surface of some tubes (Fig. 9.13d) and are composed of nickel silicate with a high content of nickel that we can associate with nickel hydrosilicate, like $Ni_3Si_2O_5(OH)_4$, according to other hollow microspheres obtained with nickel [151]. These spheres were not detected in the other salts.

In figure 9.14a we see a fiber grown from $NiSO_4$ in 1 M sodium silicate. This is a highly disordered cluster of microtubes that can be observed in a section of these tubes (Fig. 9.14b) where the thickness of the wall is about 100 μm. We can see that the thickness of its walls are the highest among all studied salts. This morphology is completely different to that seen in all other salts. EDX analysis on the walls shows higher silicon content towards the exterior and higher nickel and oxygen content towards the interior, indicating $NiSiO_3$ outside and nickel oxide-hydroxide inside. Pictures taken with the backscattering detector show zones with different brightness in this tube section. A dark external layer of sodium silicate, a bright zone of nickel silicate and the internal zone with medium brightness with a higher amount of nickel oxide (Fig. 9.14b). Crystals of sodium sulfate in form of flakes are observed on the inner surface of the osmotic envelope and the lower part of tubes (Fig. 9.14c), indicating that sodium ions can also cross the osmotic membrane.

The better crystallized phases found in chemical gardens grown from nickel were sodium sulfates with reflections at 18.9^o, 23.1^o, 28.1^o, 29.0^o, 32.0^o, 33.9^o, 38.5^o, 40.7^o, 48.8^o, 54.5^o, 55.1^o and 59.5^o (in 2θ units), which again proves that sodium ions do cross the osmotic membrane and participate in the building of the tube walls (Fig. 9.15). Poorly crystallized hydrated nickel hydroxide can be identified according to previous XRD

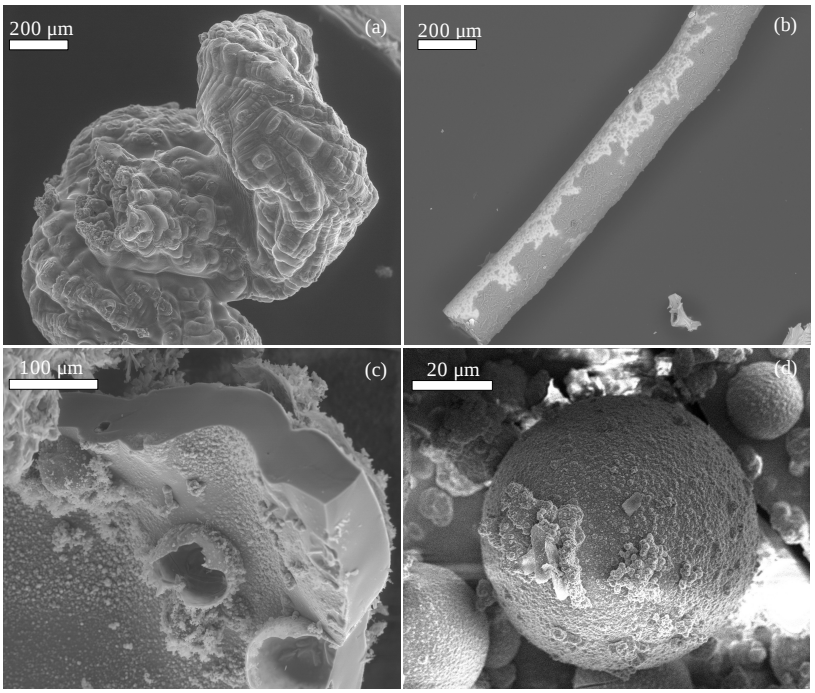

FIGURE 9.13: a) Nickel budding tube grown from grains in 6 M silicate. b) Nickel tube grown from grains in 3 M silicate. The white stains are remains of sodium silicate. c) Section of the osmotic envelope of a nickel tube grown from grains in 1 M silicate. The internal surface is covered with spheres. d) Microsphere formed on the inner surface of a tube.

studies [151]. However, the reflections at 9.5^o, 34^o, 35.6^o and 60.9^o (2θ units) can be assigned to nickel hydrosilicate, $Ni_3Si_2O_5(OH)_4$ [152]. A similar composition was detected in gardens grown with 3 M and 1 M silicate and in gardens grown from grains and from pressed wafers.

9.4 Conclusions

We found different growth regimes in different sodium silicate solutions. Lower concentrations produce clusters of narrow tubes, while higher concentrations produce single tubes. This is a general behavior for all studied salts, but with some differences. Calcium chloride has the highest reactivity, growing wider tubes with flexible thin walls at a fast rate. Nickel sulfate on the other hand has the lowest reactivity, with slow growth rate, producing very robust tubes with the thickest walls of all studied salts, probably

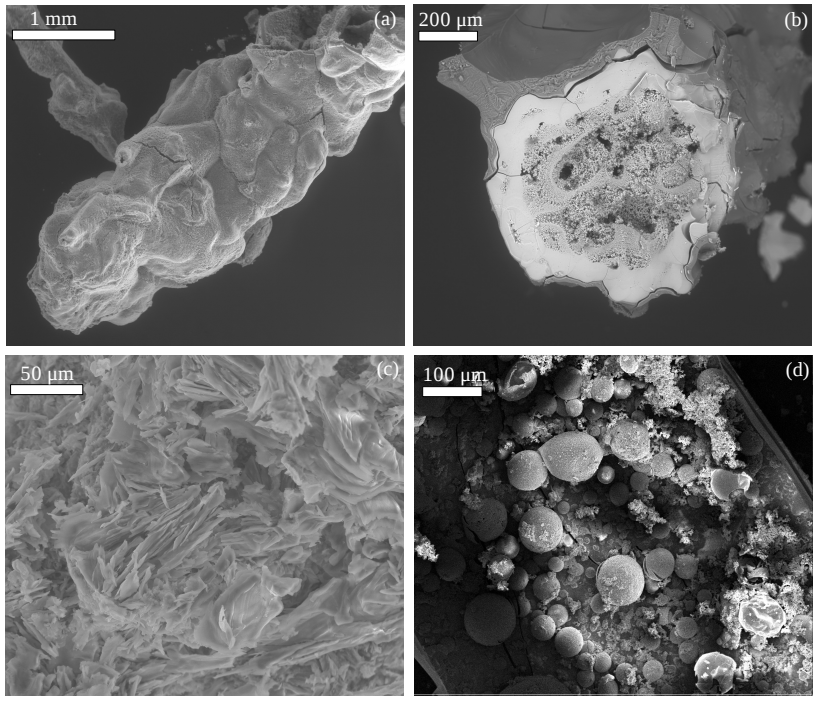

FIGURE 9.14: SEM pictures of nickel sulphate gardens in 1 M sodium silicate. a) External shape of a cluster of tubes. The irregular shape and texture is probably related with the slow growth rate. b) Section of another tube visualized by backscattering solid state detector. We can see how the internal space is highly compartmented, forming a network of conducts within the main tube. c) Crystals of Na sulphate grown on the external surface of a nickel garden tube. d) Several microspheres with different sizes formed in the inner surface of a tube.

owing to a lower solubility of the nickel species. Manganese and cobalt chloride have an intermediate behavior.

The swelling of the initial osmotic envelope decreases following the sequence: Ca $>$ Mn $>$ Co $>$ Ni. The permeability of these membranes could be related with the d(M-O) bond length that follows the same sequence: Ca $>$ Mn $>$ Co $>$ Ni.

Electron microscope imaging showed that tube walls are not homogeneous across their section. There is both a morphological and a compositional difference between the inner and outer surfaces. The different morphologies indicate that the tubes are formed by two layers, metal oxide on the inside and metal silicate on the outside. EDX analysis, however, does not have enough resolution to verify this discontinuity.

X-ray diffraction shows the tubes are mostly amorphous, but there are some crystals

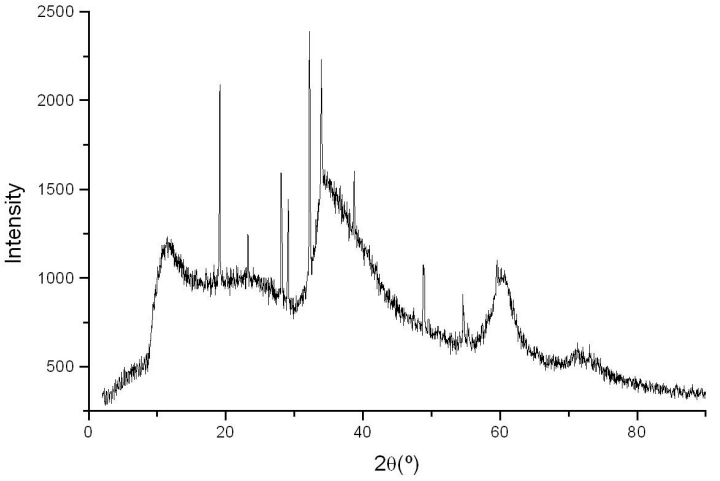

FIGURE 9.15: XRD analysis of nickel tubes grown in 1 M silicate.

present. In the case of calcium tubes we only found sodium chloride crystals, proving that sodium cations can also cross the osmotic membrane. In some manganese, cobalt and nickel experiments we found traces of metal hydroxides, which are known to participate in the wall structure.

Chapter 10

Chemical gardens in microgravity

10.1 Introduction

Buoyancy forces giving rise to convection are proportional to gravity. When chemical gardens are grown in microgravity the buoyancy effect is diminished correspondingly and the tubes, driven by forced convection alone, would be expected to grow in arbitrary directions. A unique experiment on chemical-garden growth in microgravity has been reported by Jones and Walter [142], which flew aboard the shuttle mission STS-55 in 1993.

There was an earlier experiment than Jones and Walter's flown on STS-47 in 1992, but inexplicably the researchers reported only on the details of the hardware flown, and not on the experimental results they obtained, although they mentioned twisted tube growth in random directions and in some cases 'spiral growth' [124].

Subsequent to Jones and Walter, the experimental setup reported on here was first flown aboard STS-107 in 2003. That experiment was lost when the shuttle Columbia broke up on reentry, as we recall in the dedication of this article to the astronauts who lost their lives.

Jones and Walter showed some unexpected results like reduced reactivity and plastic growth. However, questions remain on the physical aspects of this phenomenon.

In this work we present experiments, conducted on the International Space Station, with some differences compared to the experimental set up of Jones and Walter [142] and a different range of salts and silicate solution concentrations with two main aims: i) to explore further the effect of microgravity on reactivity and morphology, and ii) to setup an approach for teaching high school and university students multidisciplinary science combining space science, engineering technology, chemistry and fluid dynamics.

10.2 Materials and Methods

The experimental apparatus, the Silicate Garden Habitat or SGHab (figure 10.1), was developed by BioServe Space Technologies and flown to the International Space Station (ISS) on the space shuttle Endeavour. Two SGHabs were flown on separate missions, one in August 2007 (STS-118, ISS mission 13A.1) and a second in March 2008 (STS-123, ISS mission 1J/A). The SGHab was configured with eight chambers (four chambers per side) with transparent polycarbonate walls pre-filled with a given sodium silicate solution. Individual chambers were cuboidal in shape (2.2cm x 5.9cm x 1.8cm deep) each with a total volume of 23 ml. During installation on the ISS, the experiment was assembled such that the four chambers on Side A could be viewed by the automated imaging system.

FIGURE 10.1: The experimental apparatus, the Silicate Garden Habitat (SGHab). Developed by BioServe Space Technologies and flown to the International Space Station (ISS) on the space shuttle Endeavour. Dimensions are approximately 10cm width and 20cm height.

Approximately 1g of each of the different metal salts (0.5–0.75 mm individual crystals) were mixed with a small amount of epoxy glue and molded into a cylinder of about 5 mm in radius and 5 mm in height. The molded salts were attached to stainless steel rods and held in place separated from the silicate solution chamber. When the reactor was activated the rods pushed the salts through a foil burst disk and a duckbill valve into the silicate chamber. An automated camera and frame capture system recorded the evolution of the reaction for several days and sent the resulting images back to Earth for analysis.

The silicate concentrations were chosen to maximize the reaction velocity. Solutions were prepared from a commercial concentrated solution composed of 27% SiO_2 and 15% NaOH by dilution with ultrapure water to concentrations varying from 0.625 M to 6.25 M. The studied salts were $CaCl_2$, $CoCl_2$, $MnCl_2$ and $NiSO_4$. Table 10.1 summarizes all the performed experiments. The salt-epoxy mixture was chosen instead of pure crystals to avoid anisotropy and to fix strongly the salt to the insertion rod.

TABLE 10.1: Summary of all experiments performed on ground and microgravity at the specified silicate concentrations

Seed salt	Ground	Microgravity
$CaCl_2$	0.6 M, 2 M, 3 M, 6 M	0.6 M, 2 M, 3 M, 6 M
$CoCl_2$	0.6 M, 1 M, 2 M, 6 M	0.6 M, 1 M, 2 M, 6 M
$MnCl_2$	0.6 M, 2 M, 6 M	0.6 M, 2 M, 3 M, 6 M
$NiSO_4$	0.6 M, 1 M, 2 M, 6 M	1 M, 2 M, 6 M

The SGHabs were returned on the space shuttle and the silicate garden structures were recovered from the reaction chambers. Samples were extracted from the chambers and dried in air at 25^oC. Morphology was studied using a FEI Quanta 400 environmental scanning electron microscope (ESEM) at high vacuum and room temperature. Chemical analysis of the different sections of the samples was performed in situ in the microscope using EDAX spectroscopy.

10.3 Results

10.3.1 Buoyant Plume vs. Forced Convection

When chemical gardens are grown on Earth, a semipermeable membrane is formed enveloping the seed salt as soon as it is immersed in the silicate solution. This membrane is inflated with water from the silicate solution forced into the interior of the membrane by osmotic pressure. As the membrane increases in volume its walls become thinner, until a hole is formed through which a jet of metal salt solution is expelled. The membrane may initially burst in any part of its surface, so the initial jet and the resulting tubes may start growing in any given direction. Since the ejected metallic solution is

lighter than the surrounding silicate, after the initial jet of fluid loses some pressure, buoyancy forces become predominant and the tubes will turn and grow towards the surface. The combination of both growth regimes is a complex one.

When we repeated the same experiments in space — in microgravity — we were removing gravitational force from the equation and hence eliminating buoyancy. Under this condition, the reaction proceeded with forced convection driven by osmotic pressure alone and in general tubes were observed to grow out of the membrane in straight, random directions. In figure 10.2 we compare results from experiments performed on Earth and in microgravity with the four studied salts: $CaCl_2$, $MnCl_2$, $CoCl_2$ and $NiSO_4$. Silicate concentrations were selected to maximize the reactivity, based on the report by Jones & Walter that silicate garden reactions in space would be much slower than on Earth [142].

In experiments performed with 2 M silicate, we could clearly see the difference in growth directions, being always vertical in the presence of gravity and random in its absence (Fig. 10.2). This same behavior also applies to the case of microscopic tubes, as we see in SEM imaging of calcium gardens grown in 3 M silicate (figure 10.3). In the case of $CaCl_2$ in 2M silicate, we also observed how the main tube in the flight experiment turned at a point where the growth stopped and then resumed in a different direction, probably due to a decrease in the metal salt solution flow after the initial jet was extinguished. The same salt immersed in 0.6 M silicate in space did not grow any tubes after 5 days, whereas it took less than 8 hours for the tubes to reach the top of the chamber in the ground experiment. This lack of tube formation was observed in every experiment with lower silicate concentrations for all of the studied salts and is discussed in Section 10.3.2.

In our experience $MnCl_2$ is the most reactive salt for growing chemical gardens. When manganese gardens are grown on Earth, they usually develop the thick, twisted tubes that we can see in the 2 M example in figure 10.2. We did not observe this type of tube formation in microgravity, but did find signs of a higher reactivity for this particular salt. In the 2 M experiment, the manganese salt started to dissolve as soon as it was introduced into the chamber, producing microscopic tubes growing in all directions (Fig. 10.2). The main tube grew faster than in the case of the other salts, at approximately 1 cm per minute, even after bouncing off the chamber wall. Tubes failed to grow initially in the 0.6 M silicate solution, as was the case with other salts, but after 4 days a very thin tube appeared growing at approximately 0.5 mm per hour (Fig. 10.2).

As expected, $CoCl_2$ and $NiSO_4$ gardens exhibited lower growth velocities than the other salts (0.3 and 0.1 cm per minute respectively). In the case of nickel almost no growth was observed in microgravity, but it also displays little growth on Earth.

Figure 10.4 shows the beginning of tube growth on the surface of the osmotic bubble for an experiment with $CoCl_2$ in 2 M silicate in microgravity. We can see that direction of those tubes is random instead growing only upwards.

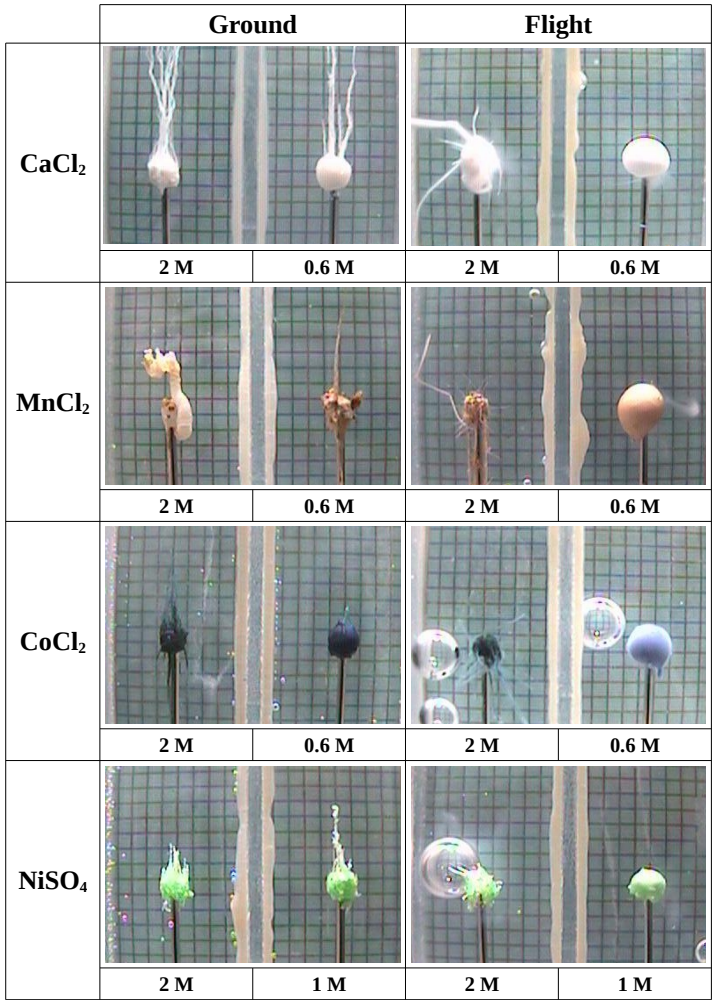

FIGURE 10.2: Comparison of similar experiments performed with and without gravity, at different sodium silicate concentrations. In ground experiments tubes grow upwards regardless of the location where the semipermeable membrane initially bursts. Flight experiments exhibit tubes that grow in straight, random directions. Images from the Earth controls were taken after 8 hours of growth, when the metal salts were completely depleted. Images from the flight experiments were obtained 5 days after initiation, after which the SGHab had to be removed from the imaging unit owing to time limitations on the International Space Station. The lines are 2 mm apart.

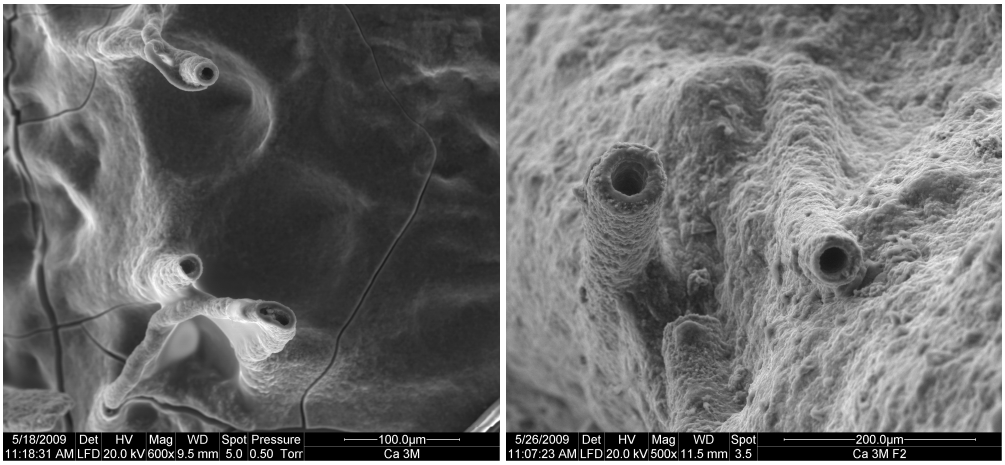

FIGURE 10.3: Micrographs of calcium tubes grown in 3 M sodium silicate on Earth (left) and in space (right). In the presence of gravity all tubes grow upwards driven by buoyancy. In the absence of gravity we see tubes growing at angles from each other.

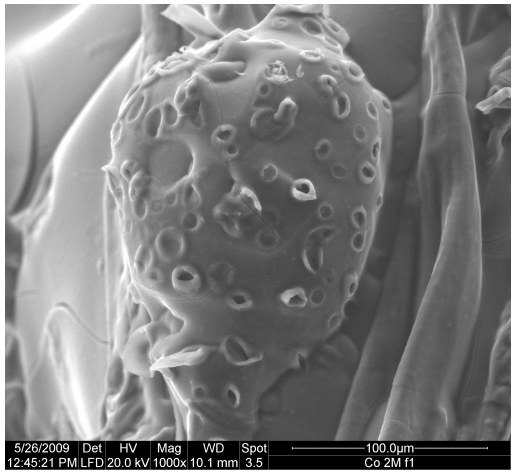

FIGURE 10.4: Micrograph of $CoCl_2$ growing in 2 M silicate in microgravity. The beginning of several tubes from the osmotic envelope follow random directions.

Other experiments not shown here did not produce positive results due to several apparatus failures, like having air bubbles trapped in the reactor chamber or the jamming of the pushing rods. Some experiments did not have enough time to complete due to time limitations in the International Space Station and the lowered reactivity in microgravity.

Besides the different growth orientation behavior, the most evident difference between the two sets of experiments was the reactivity, it taking several days to accomplish in space what it only takes an hour to do on Earth.

10.3.2 Growth Rate

Chemical gardens grow by precipitation of silica on the outer side of the tube and metal oxide on the inner side [106]. The precipitation involves depletion of reactive molecules around the growth area, creating a concentration gradient. In the presence of gravity this gradient is automatically and rapidly reduced by convection. In space however, the depletion of reactants reduces the growth rate, reaction becoming diffusion-limited. In this manner, a reaction that takes a few minutes to complete in Earth gravity, can last for several days in space. In the calcium chloride example shown in figure 10.2, the Earth experiment grew at 20 mm per second, while the space tubes grew at less than a millimeter per hour. Other salts exhibited similarly large differences in growth rates. In some extreme cases, where the silicate concentration was not optimized for reactivity, no tubes at all appeared. Instead, the initial salt would inflate absorbing the silicate solution up to several times the initial volume, but never bursting nor growing any tubes. Upon examination of these inflated salts, we found no discernible morphology differences across their section and the chemical composition was essentially metal silicate, with increasing metal concentration toward the interior of the sphere. Metal oxide predominantly made up the composition of the interior of tubes (see figure 10.5).

10.3.3 Plastic Deformation

The low reactivity in the absence of gravity also accounted for a different type of growth that Jones and Walter named “plastic deformation” [142], as opposed to “open–ended tubes”. The shortage of precipitant reactants due to the absence of density-driven convection resulted in the initial semipermeable membrane remaining fluid for a relatively long time. Any excess of pressure in some region of the membrane would be expected to make it bulge outwards, forming a hump on the membrane surface. We have an example of just this situation in a manganese garden grown in 6 M silicate (figure 10.6a), where the surface of the membrane has bulged by inner pressure without bursting. The brighter region is rich in MnO and the darker in $MnSiO_3$. The cracks on the surface appeared during the drying of the sample. As the membrane continued to push outwards, its walls would become thinner and more flexible, presenting less resistance to

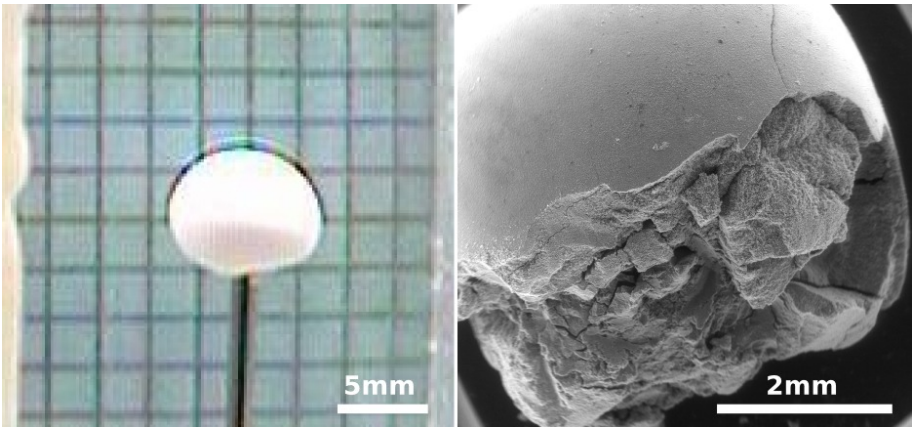

FIGURE 10.5: (a) Photograph of $CaCl_2$ experiment performed in space with the less reactive 0.6 M sodium silicate. Instead of forming a membrane and tubes, the initially cylinder–shaped salt inflated into a sphere. (b) Examination with SEM and EDX showed that the whole sphere was composed of calcium silicate.

the pressure inside and forming an elongated shape like a plastic finger. This can be described as a Laplacian growth instability, as was noted by Mullins and Sekerka [153]. We can see examples in a nickel garden grown in 2 M silicate, shown in figures 10.6b,c. Eventually, silicate precipitates from the outside and metal oxide from the inside, hardening and preserving the structure. This is a growth mechanism not observed in Earth experiments, which produce very irregular shapes, not always straight and not always cylindrical in cross section.

In figure 10.7 we show an SEM image of a $MnCl_2$ garden grown in 2 M sodium silicate in microgravity. This particular experiment has instances of the classic, chemical garden tubular growth and the microgravity exclusive plastic growth.

10.3.4 Oscillatory Growth

Chemical gardens on Earth have been reported to grow by pulses due to relaxation oscillations of the silicate membrane [139, 143, 146]. The resulting tubes look sectorized or periodically strangulated. This growth regime can be provoked by injecting the metal salt already dissolved at a specific concentration and pressure. Thouvenel-Romans et al. [139] found that tubes could switch from steady to pulsating growth modes by changing the concentration of the the injected metal salt solution. The same research group proved that tube growth can be templated by buoyant gas bubbles [143] at the tip of the growing tubes and, in these cases, that the external surface of the tubes is patterned with silicate rings, a phenomenon that we have also observed even in the absence of gravity.

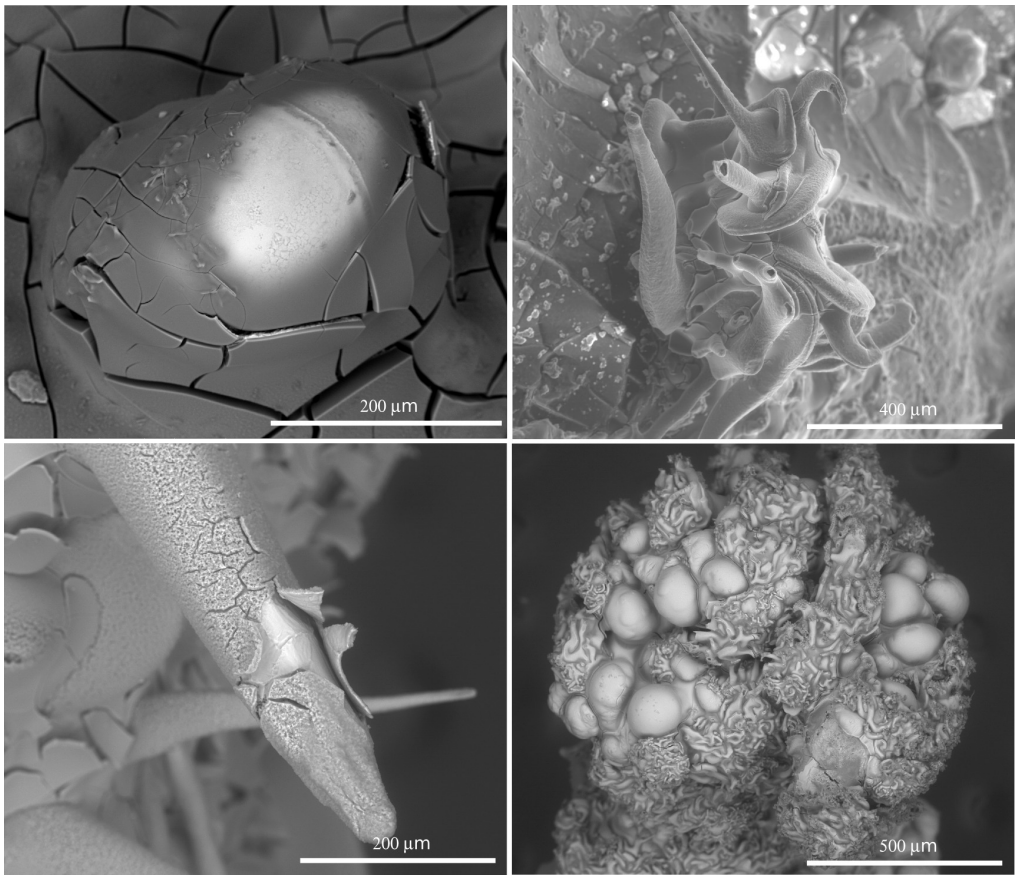

FIGURE 10.6: Examples of plastic deformation in microgravity: a) $MnCl_2$ in 6 M silicate. The surface of the membrane has bulged by inner pressure but without bursting. This image was taken with backscattered electrons, the brighter region is rich in MnO and the darker in $MnSiO_3$. The cracks on the surface appeared during the drying of the sample; b) $NiSO_4$ in 2 M silicate. Several twisted fingers grown by plastic deformation; c) $NiSO_4$ in 2 M silicate. The surface of this finger has peeled off revealing the hardened NiO interior. d) $NiSO_4$ in 1 M silicate grown on Earth. In the presence of gravity we did not see plastic deformation, but we found other rare morphologies like those we display here.

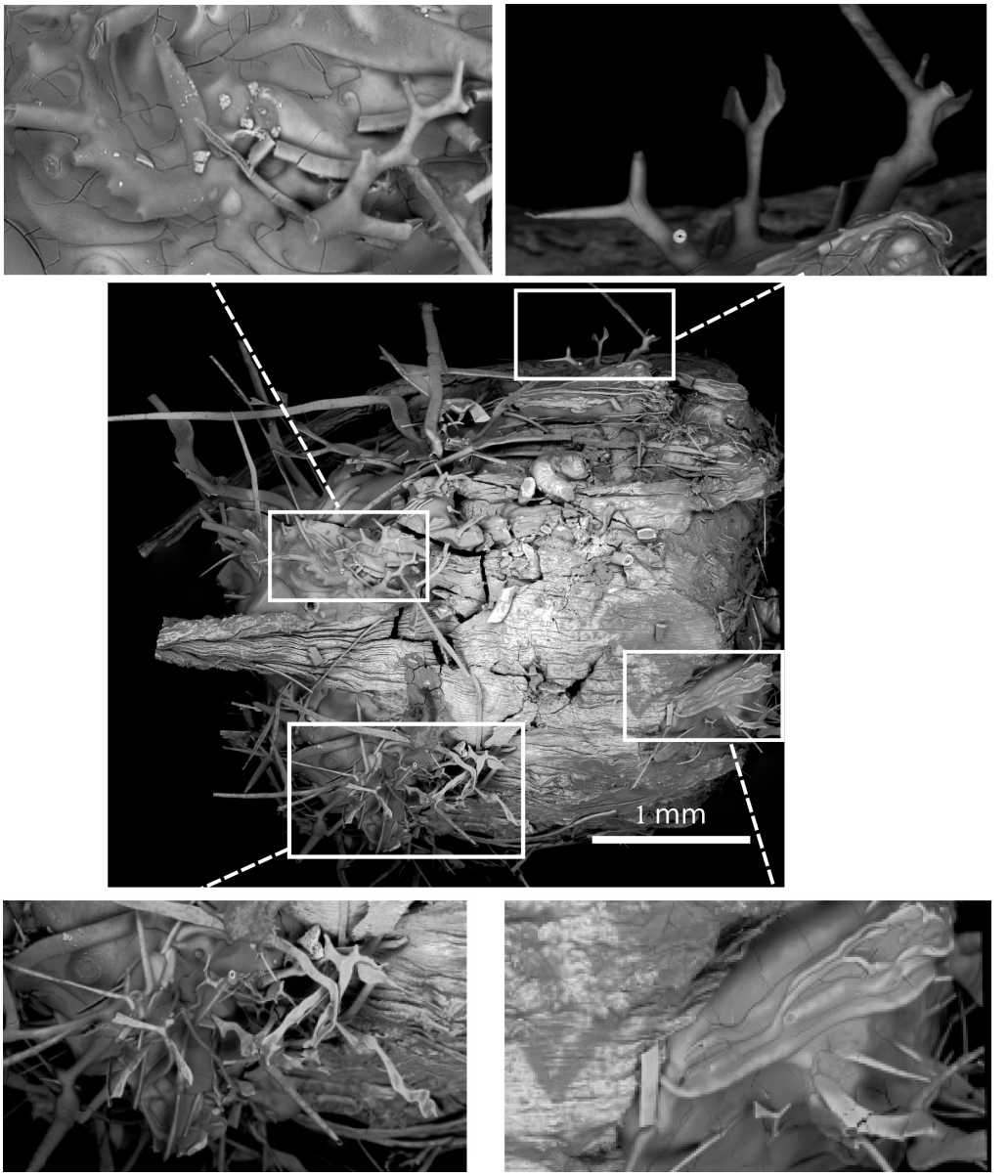

FIGURE 10.7: General view of a garden grown from $MnCl_2$ in 2 M sodium silicate in microgravity. In this image we see different shapes and textures corresponding to the different growth modes. Most of the longer tubes were broken during transportation. Insets show close-ups on plastic and branched growth.

The bubble at the tube tip dictates the tube's radius and also influences the growth rate by volume conservation of the injected solution. We observed this oscillatory form of tube both on Earth and in space, but in microgravity the effect seemed to be more accentuated and more frequent. The reason for this increased frequency is unclear but may be related to the lower reactivity in space producing lower pressures inside the osmotic pump. In figure 10.8 we show examples of oscillatory growth of a cobalt garden in 2 M silicate on Earth (a,b) and in space (c,d).

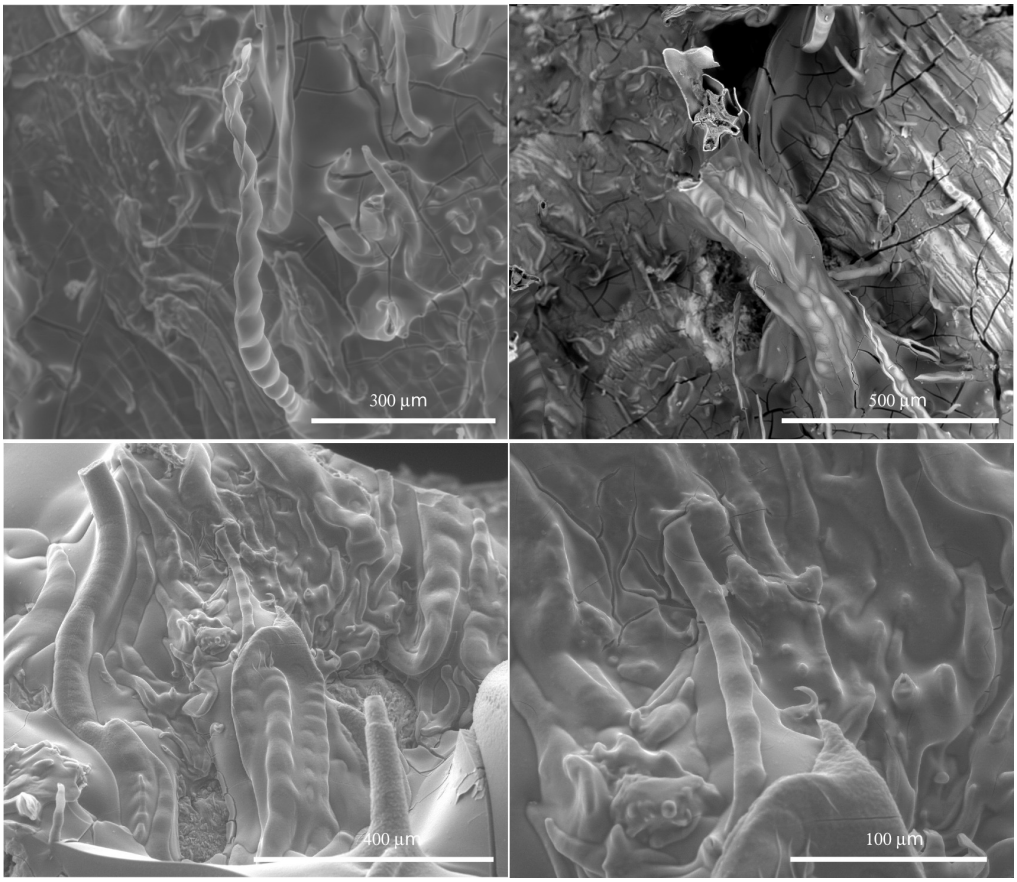

FIGURE 10.8: Examples of oscillatory growth for similar experiments performed on Earth (first row) and microgravity (second row). The experimental conditions were $CoCl_2$ in 2 M silicate.

10.4 Conclusions

The purpose of these experiments was to remove the influence of buoyancy during the formation of chemical gardens to focus on the forced convection part of the phenomenon. We expected to obtain straight tubes emanating from the initial salts and, indeed, in some cases such tubes were observed. When the silicate membrane does break, it does so in any given direction and forms a tube that will grow along that initial direction until the metal solution is depleted or until it reaches the chamber wall, where it may even reflect off the wall and continue to grow in a new direction.

We did not however expect that the reduced reactivity would have such a strong influence, something reported as well by Jones and Walter in their space experiments [142]. The absence of gravity means there is no convection due to buoyancy. A diffusive zone of reagent depletion becomes then an important factor, slowing down the reaction from hours to days and establishing a diffusion-limited environment. The duration of this lengthened process was not adequately taken into account in scheduling the experiment on the International Space Station.

The reduced reactivity also had an apparent secondary effect, the appearance of a totally different growth regime. Plastic deformation by the swelling of the membrane produces morphologies that are not seen on Earth, introducing new questions about the malleability of these materials and their hardening process. We also found a remarkable abundance of pulsating or strangulated tubes, which was surprising but may be attributed to the diffusion limited convection, that reduces the flow of the metal salt solution.

The chemical composition analysis of silicate gardens grown in space did not differ from those grown under gravity. We still found metal oxides on the inside of tubes and metal silicates on the outside. Powder diffraction did not show any effects on crystallizing in space either. Only a few crystalline phases could be identified, similar to what other studies on Earth have demonstrated.

Part IV

Nacre

Chapter 11

Nacre: Introduction

Nacre is the iridescent layer that composes the inner layer of some molluscs shells. It is exclusively present in gastropods, bivalves and cephalopods. It is also the material of which pearls are made of, grown by multilayering coating of a foreign body when it is trapped inside a bivalve shell [154]. It is a composite biomaterial formed mainly of crystalline calcium carbonate in the aragonite polymorph (95%), the polysaccharide chitin and proteins (5%). It is an interesting material not only for its aesthetic qualities, but also for its mechanical properties, much stronger and resilient than its separate components by themselves [155]. It is also a biocompatible material, which makes it a perfect candidate to apply in medicine as a substitute for bone tissue.

There is still much to be known about the formation mechanisms and about the microstructure of nacre. Cartwright and Checa have proposed a model based on liquid crystal self-organization of chitin in the interlamellar layers [156]. A better understanding of nacre's formation could allow the possibility of growing artificial nacre and would open a great diversity of applications. This problem is a clear example of self-organized pattern formation in bio-mineralization.

Structure

Nacre is composed of hexagonal tablets of aragonite, 5–10 μm wide and 0.5 μm thick, arranged by layers in the case of bivalves and forming towers in the case of gastropods, with the crystallographic c-axis perpendicular to the shell[157] (see Figure 11.1). Between each layer of tablets there are sheets of an organic matrix of elastic biopolymers, called the interlamellar membrane. If we look at the nanoscale, we see that each tablet incorporates organic fibers within the aragonite mineral, while the interlamellar membrane is composed of chitin crystals embedded in a protein matrix. The mixture of

brittle aragonite platelets and the layers of elastic polymers is what makes nacre so strong and resilient, with a Young modulus of 70 GPa [155].

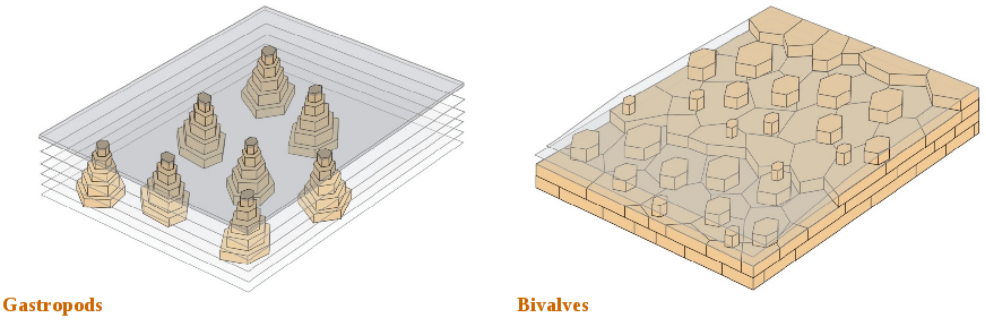

FIGURE 11.1: Growth models for gastropods (towered growth) and bivalves (terraced growth).

The iridescent appearance of nacre is also a consequence of its structure. The thickness of the aragonite tablets is close to the wavelength of visible light, producing constructive and destructive interferences that reflect the different colors of light with different angles.

Formation sequence

The formation of nacre is a self-assembly process in which all the chemical compounds are secreted together into the extrapallial space, a liquid filled cavity between the mollusc's body and its shell, where they are organized exclusively through chemical and physical mechanisms without any cellular intervention.

The sequence begins with the secretion of the polysaccharide chitin from the mollusc's mantle into the extrapallial space. Chitin is one of nature's most abundant biopolymers. The α-Chitin polymorph, with an orthorhombic crystal structure and anti-parallel polymer chains, is the most commonly found and is part of the exoskeleton of insects and crustacei. But molluscs produce the rarer β polymorph instead [158], with a monoclinic crystal structure and parallel polymer chains. β-chitin polymer chains are extruded from the cellular membrane and immediately crystallize by hydrogen bonding into long thin crystallites [159].

These crystallites, 20–30 nm in diameter and hundreds of nanometers in length, are suspended in the extrapallial space in the form of a liquid crystal, as proposed by Cartwright and Checa [156]. In this state, the particles possess a certain amount of

order, as in a crystal, but still have some freedom to move, as in a liquid. Given enough time, these crystallites would self-organize forming a cholesteric liquid crystalline phase [160], in which the crystallites are parallel to the plane of the layers but are twisted with respect to those in the neighboring layers. But molluscs lay a fresh layer of nacre every 24 hours [161], so the chitin crystallites do not have enough time to achieve this configuration and the liquid-crystalline ordering is only partial. The crystallites are organized in parallel layers but are disordered within each layer, forming a felt-like mesh (see Figure 11.2). The liquid-crystal layer of chitin crystallites does not have great stability by itself, and it is covered by a coating of proteins that are present in the extrapallial fluid. It is this coating that binds together and stabilizes the crystallites, forming a strong composite material that composes the interlamellar membrane. The separation between two consecutive layers of liquid-crystal is determined at first by the physical interactions between the crystallites, resulting in approximately 60–120 nm separation. However, after the protein coating, this distance can increase to about 500 nm between interlamellar membranes [162].

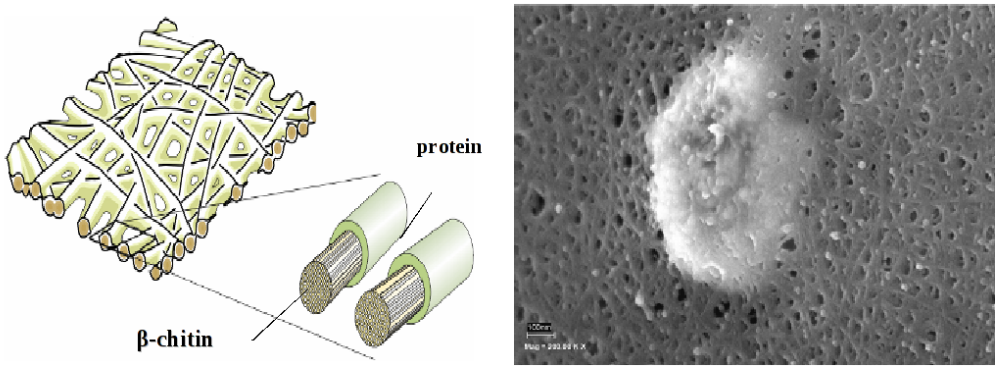

FIGURE 11.2: Sketch and micrograph of the interlamellar membrane.

In the case of bivalves, the chitin crystallites self-organize to form a fresh layer of interlamellar membrane, which aligns itself with the membranes laid down earlier. In gastropods, there is another membrane that separates the mantle of the animal from the growing surface of nacre. It is termed the surface membrane and was discovered by Nakahara in 1991 [163]. Its function is probably to protect the growing nacre from the exterior seawater when the animal retracts into its shell, which would not be necessary for bivalves as the growing surface never comes in contact with the exterior. The surface membrane appears to have a dynamic structure, with new material continuously being added at the mantle side and fresh interlamellar membranes being periodically detached at the shell side. The surface membrane also appears to serve as a template for the crystal growth, which explains why there are fewer defects in gastropods than in bivalves. The two different growth processes produce totally different surface patterns on

the nacre surface of bivalves and gastropods at the microscopic scale: bivalves exhibit a terraced surface growth, in contrast with the towered growth found in gastropods, as can be seen in Figure 11.3.

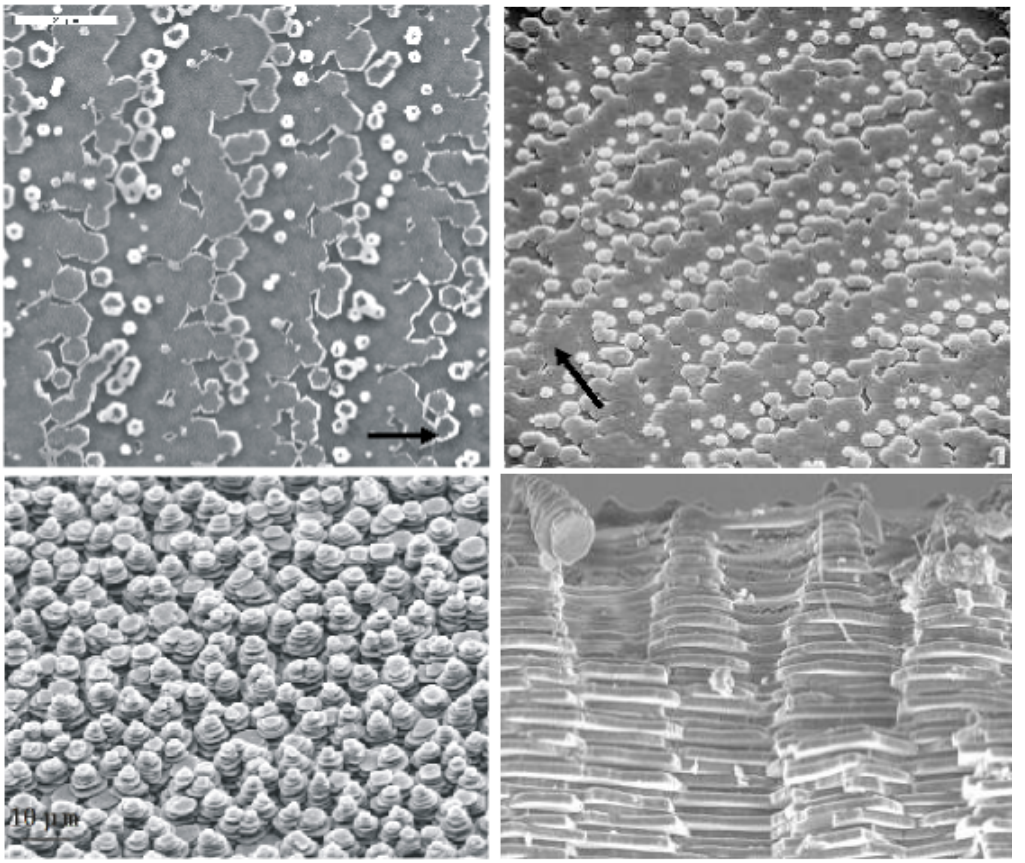

FIGURE 11.3: Surface morphology of bivalve nacre (upper row, arrows indicate terrace growth directions) and gastropod nacre (lower row).

So far we have described how chitin and proteins assemble to form interlamellar membranes. Even if this constitutes only 5% of nacre's final mass, it defines the structure and the surface morphology. Now it only remains to fill in the spaces with the mineral aragonite, which will give the final product its unique mechanical properties. The mineralization process of nacre proceeds with calcium carbonate occupying the space between the interlamellar membranes. Calcium carbonate may crystallize in various different polymorphs (i.e. calcite), but it is only the less thermodynamically stable aragonite polymorph that is found in nacre. Thus, there must be some control from the system to select what polymorph is deposited. Belcher et al.[164] found that certain proteins present in nacre may cause calcium carbonate to crystallize as aragonite instead

of calcite, which is a weaker material. The mineralization may take place simultaneously in several adjacent membranes, with the calcium carbonate being secreted by the mantle and filtered through pores in the membranes. In this way, aragonite hexagonal tablets continue to grow in between the spaces left by the membranes, starting at the membrane pores and expanding until they meet the neighboring tablets. In gastropods, tablets on upper layers are aligned with those in lower layers because the surface membrane templates the pore distribution[165]. This produces a columnar morphology that resembles a stack of coins. On the other hand, membrane pores in bivalves are randomly distributed, the tablets of a fresh layer will begin to grow at the edges of tablets in the layer below, like in a brick wall.

Pattern formation

When the surface of gastropod nacre is examined at the microscale, we find it formed by stacks of aragonite tablets piled like a pile of coins. This is a consequence of 2D nucleation and growth templated by the gastropod's surface membrane. It is this membrane that will start the growth of a new layer always at the same spot, nucleating a new island only when the surface below is flat enough, otherwise the precipitating material will only attach to the edges of said islands. It is a process where the growth rate is determined by the supersaturation of precipitating materials in the solution and the nucleation probability depends on surface diffusion. The gastropod surface membrane avoids the formation of defects, so only some edge dislocations may be found in gastropod nacre.

Bivalve nacre follows the same principles but lacks the templating effect of a surface membrane. In this case the surface morphology is usually governed by spiral patterns, which are a consequence of screw dislocations. In any two-dimensional crystal, when two growth fronts collide, there are three possible outcomes: they may annihilate each other ending the growth; they may overlap so one of them continues growing over the other; or just partially overlap, so part of one front continues its growth over the other, revolving around the dislocation center. In this last case we have a screw dislocation, which will continue growing developing a spiral pattern (see Figure 11.4).

In this work we have developed a simple mathematical model, based on the most basic physical interactions between chitin crystallites, to reproduce the patterns forming on the nacre surface and to investigate how such patterns may be templated by the interlamellar membranes.

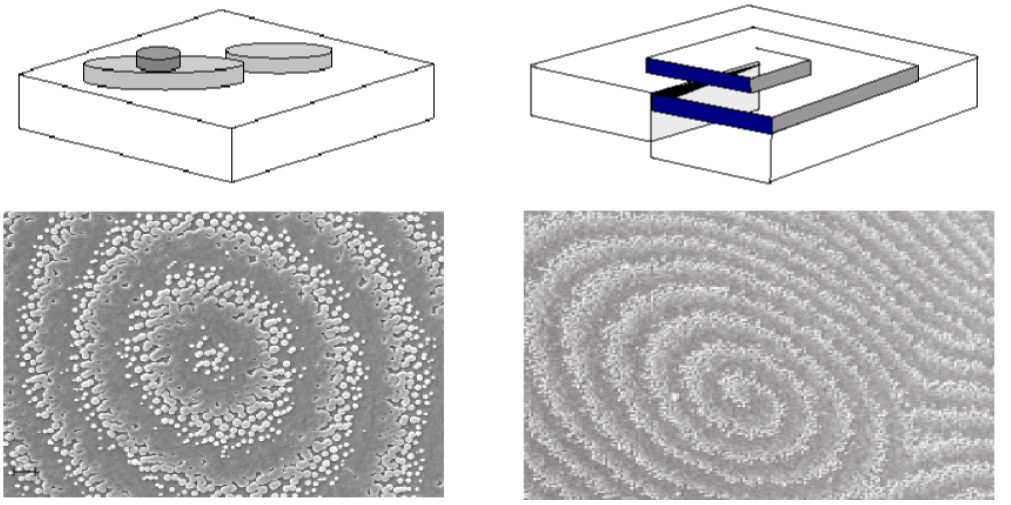

FIGURE 11.4: Target pattern in bivalves (left) as a consequence of templated 2D nucleation and growth. Spiral pattern in bivalves (right) as a consequence of screw dislocations in terraced growth.

Chapter 12

Spiral and target patterns in bivalve nacre

12.1 Introduction

The splendor of a pearl extends even to under a microscope; with magnification one can see that the nacreous surfaces of bivalve molluscs — clams, mussels, oysters, scallops, and so on — are made up of a striking arrangement of spiral, target and labyrinthine patterns [166]; see Figure 12.1. Nacre, or mother of pearl, is the iridescent material that forms an inner layer of the shells of numerous species of molluscs, as well as the pearls that many of those same species produce. The structure of nacre is often likened to a brick wall, and indeed it is composed of bricks of aragonite tablets (approximately 95%) and mortar of organic so-called interlamellar membranes (polysaccharide and protein, $\sim$5%), but it is a brick wall built in a peculiar fashion, as first the mortar is put in place, and then the bricks grow within it. (See Figure 12.2 for a sketch of bivalve molluscan anatomy and nacre structure.) From an examination of the extrapallial space of the bivalve mollusc, the narrow liquid-filled cavity between the soft tissues and the shell of the organism, it is seen that the first visible feature in nacre growth is the formation of a new interlamellar membrane in the fluid [156, 162, 163]. In Figure 12.3A we show this process occurring in a transmission electron micrograph section through the growth front of bivalve nacre that displays the hard shell below, and the soft body of the organism, the mantle, above the liquid-filled extrapallial space. The membrane in its moment of formation is spaced some 100 nm above an earlier-formed one below it; there is not space between the membrane and the microvilli of the mantle cells above for any additional membrane to form. We must follow it back some 20 μm to find the front where the process of mineralization is seen to commence, and by this stage its spacing from the membrane beneath has increased to approximately 500 nm. The core of these membranes is composed of rod-shaped crystallites of the polysaccharide chitin

in its β polymorph [158]. This must be secreted into the extrapallial liquid together with the mineral and protein components of nacre; it is thought — although not yet confirmed — that similar mechanisms are responsible for chitin as for cellulose crystallite formation, wherein rosette structures in the cellular membrane extrude polymer chains from closely packed pores, whence they immediately crystallize by interchain hydrogen bonding into long thin needle crystallites [159]. In the case of nacre these crystallites of β chitin are known to be some 20–30 nm in diameter and up to hundreds of nanometers in length, consisting of hundreds of chitin polymers [167].

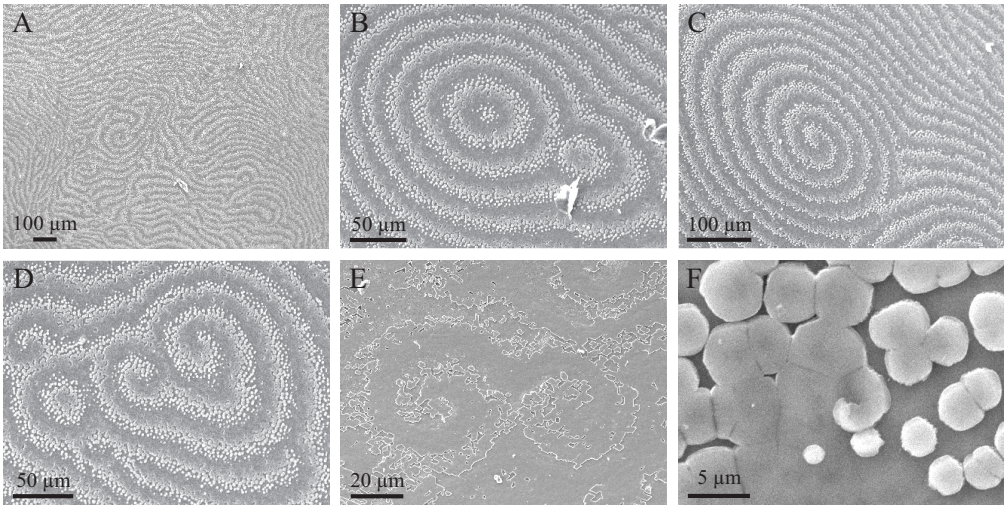

FIGURE 12.1: Scanning electron micrographs of the growth surface of bivalve nacre: (A) General view of labyrinthine patterning; (B) Target patterns; (C) Colliding growth fronts and spiral; (D, E) Paired spirals; (F) The aragonite tablet at the center of a spiral follows its structure. (A–D) are *Pteria avicula*, (E, F) *Pteria hirundo*. In all these images we see only the mineralized portion of the nacre, consisting of aragonite tablets. The interlamellar membranes atop the uppermost mineral layer are generally lost as the soft tissue is removed, unless the sample is especially prepared to preserve soft tissue as well as biomineral, as in Figure 12.3A.

Interlamellar membrane formation is then necessarily a process of self-assembly within the extrapallial fluid; to use our brick-wall analogy, it is as if one empties clay, lime, sand and water into a tub, and finds that sheets of mortar form spontaneously within it. What prompts chitin crystallites to self-assemble into sheets? α-chitin crystallites of similar dimensions to the β-chitin crystallites of molluscs have been studied *in vitro*. When dispersed in a colloidal aqueous suspension they form a so-called cholesteric liquid-crystalline phase, in which the crystallites are parallel to the plane of the layers, and the crystallites in each layer are twisted with respect to those in the neighboring layers, with an interlayer spacing of 60–120 nm [160], comparable with the 100 nm seen here. Similar preparations using β-chitin crystallites from a cephalopod mollusc

(*Todarodes pacificus* squid pen) [168] and from a vestimentiferan tube worm (*Riftia pachyptila* tubes) [169] indicate that these too form a liquid-crystal phase in aqueous suspension. Birefringence was observed at rest between cross polarizers for dispersions of more than 0.1% β chitin and at 0.3% consistency they formed hard gels [168]. (Note that we are concerned not with a molecular liquid crystal of chitin polymers, but with a colloidal or supramolecular one of chitin crystallites.) In laboratory experiments, the liquid crystalline structure is allowed to come to equilibrium by waiting from a few days up to a year [160]. In the mollusc *in vivo*, on the other hand, a fresh layer of nacre is laid down every 1–24 hours, so the system does not have time to arrive at equilibrium, and the liquid-crystalline ordering of β-chitin is only partial. It comprises a lamellar structure, but within the layers there is disorder, with the crystallites forming a feltlike mesh, like a logjam on a lake, as seen in the plan view of Figure 12.3B. Simulations of the dynamics of the formation of a cholesteric phase of a liquid crystal confirm that there is an initial orientation of the material into layers followed by its alignment within and between layers [170]. The evidence leads us to conclude that in Figure 12.3 we are observing the rod-shaped crystallites of β-chitin, being compelled by their mutual interactions, self-organizing in the extrapallial space into a liquid crystal.

Artificial liquid crystals are formed by altering a global variable — be it temperature, concentration, electric field, etc — that causes the whole of a domain to crystallize, forming many layers at once. We perceive from Figure 12.3 that molluscs, on the other hand, perform liquid crystallization in quite a different manner: layer by layer. The narrowness of the molluscan extrapallial space implies that as chitin crystallites are secreted into the extrapallial fluid they can only self-assemble through their mutual interactions into one new liquid-crystal layer. The continual secretion of material from the mantle cells maintains the extrapallial space approximately constant in depth, so that at any time one fresh layer of the liquid crystal is being deposited, and in this way in time the mollusc builds a liquid crystal within an expanding domain. This is concurrently transformed with the addition of proteins and aragonite into the solid biocomposite that is nacre; a process that we analyze in depth elsewhere [156]. Here we concentrate on understanding the mode of liquid-crystal construction employed by the mollusc, in which it is built up layer by layer. This method is novel in terms of artificial liquid crystals, but is the manner in which solid crystals generally grow, and this connection allows us to comprehend the spiral and target patterns on the surface of nacre.

12.2 A liquid-crystal layer growth model of nacre

Layer or tangential growth of a solid crystal, analyzed by Burton, Cabrera, and Frank [171], involves two processes: on one hand the addition of material at the edges of two-dimensional islands on the surface of the crystal together with the occasional nucleation of a fresh island atop an earlier one, and on the other the continual accretion of material

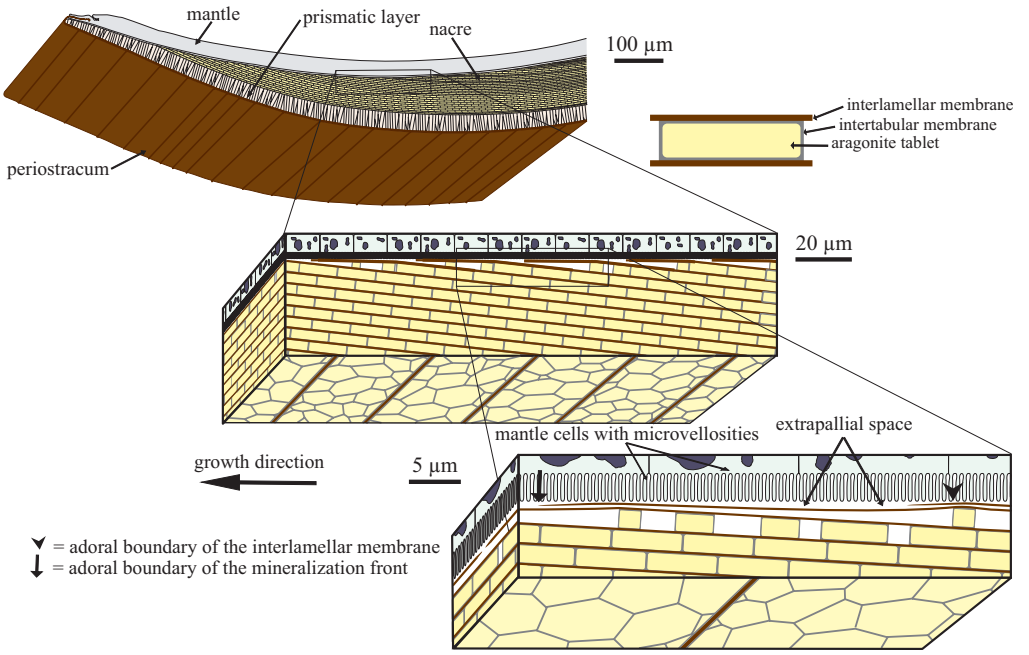

FIGURE 12.2: Sketch of bivalve mollusc anatomy indicates the position of the liquid-filled interlamellar space between the mineralized shell and the mantle part of the soft body of the organism, and illustrates with successive amplifications the brick and mortar structure of nacre. The growth surface, on which the patterns in Figure 12.1 are observed, is between the mantle and the shell; i.e., into the page.

at the edges of a helical ramp on the surface of the crystal, termed a screw dislocation [172]. (Tangential growth as a whole was examined by Burton, Cabrera, and Frank [171]; Frank's contribution was the analysis of screw dislocations [173]). These two processes produce characteristic target and spiral patterns seen at the molecular scale in solid crystals [174]. These same patterns are visible in the conspicuous features of the surface of nacre at the mesoscale in Figure 12.1. In that figure the patterns are arrangements of aragonite tablets in mineralized nacre. However, as we see in Figure 12.3A, in growing nacre interlamellar membranes extend ahead of these mineralization fronts; the latter follow the geometry laid down by the former. This is evidenced by the forms of tablets that grow at the centers of the screw dislocations in the membranes, which mould themselves to the spiral, as shown in Figure 12.1F. Thus the spirals and target patterns are in fact laid down in the interlamellar membranes, and we must establish that growth of an interlamellar membrane as a liquid crystal layer by layer can give rise to this geometry of spirals and target patterns.

We formulate a minimal model containing the fundamental physics of the liquid crystallization. Growth proceeds by the incorporation of individual growth units, which are

the chitin crystallites that compose the liquid crystal. As this is an essentially discrete process we employ a discrete coupled map lattice, or lattice Boltzmann model, with a square lattice of discrete space and time but continuous state variables, that puts nucleation and growth on an equal footing. The surface is divided up into a randomized grid of cells, as introduced by Markus & Hess [175], to avoid anisotropic growth. Each cell has a growth height $H(i,j)$, initially zero, updated at the end of each iteration of the growth. The surface is scanned on each iteration and in each cell there may occur either nucleation, growth, or neither, as a function of the relative height of the nearest neighbors. The neighbors to each cell are assigned by proximity, defining a circle of radius R around the cell.

The essential physics we wish to capture in our model is that a fresh growth unit is incorporated into the growing surface most probably at a site where it is more strongly bound by virtue of having most neighbors. Such sites are so-called kinks: concavities at the base of steps on the surface. Thus there is no probability of a growth unit settling above a step, as it will slide down to occupy a more favorable site below; there is a rather low probability of a growth unit settling on a flat surface; and a very high probability of it occupying a site at the base of a step. This physics we can model by setting a low probability of addition of material, which is termed nucleation, at any point over the surface that is not elevated above its neighbors, together with a certainty of the addition of material, which is termed growth, at the kinks of steps.

The condition for nucleation is that the cell should not stick out far above its neighbors; that the surface be sufficiently smooth. The cell in question should have height comparable to that of its neighbors with a difference not more than Δh_N. If so, there is a small probability P_N of nucleating a fresh growth surface. Nucleation is a fundamentally stochastic process, and this is reflected in the model. If nucleation takes place, and a new growth unit is incorporated, the growth surface increases in height by one plus or minus a small random factor α:

$$H(i,j) \rightarrow H(i,j) + 1 \pm \alpha.$$

The condition for growth is that the cell must be at the edge of a growth front; i.e., must have neighbors higher by at least Δh_G. If so a growth unit is incorporated: the growth height is increased by the mean of the higher neighbors plus or minus α, and a growth front extends:

$$H(i,j) \rightarrow H(i,j) + \sum_{(k,l)} \frac{H(k,l) - H(i,j)}{n} \pm \alpha,$$

where (k,l) are the coordinates for each higher neighbor and n is the total number of higher neighbors, which depends on R. This part of the model is deterministic but for the parameter α, which adds a certain amount of noise so that the growth surfaces are not completely flat and defect-free.

In this way, as a growth front grows out its height may vary and if it encounters another front of different height, following the rules above, defects may be spontaneously incorporated into the growth. Two growth fronts that meet may join seamlessly with each other, terminating growth; they may completely overlap each other, forming an edge dislocation; or they may overlap along part of the edge and join along the rest, nucleating a spiral defect as growth continues. All of these behaviors are comparable in the model — Figure 12.4 — with nacre itself, Figure 12.1.

In our model the set of parameters comprises:

α Stochastic term, typically ± 0.05 to 0.1, that varies the height of the growth cell on nucleation and growth, otherwise renormalized to be unity. This term is responsible for defects. Physically this growth-height variation is related to the fact that the growth units in the case of nacre are non-identical; they are rods of differing lengths. An additional factor in the appearance of height variations leading to defects in all layer growth is the presence of impurities.

Δh_N Threshold of elevation with respect to the neighbors below which a cell's neighborhood is considered sufficiently flat for nucleation of a fresh layer to occur. A larger value of Δh_N implies that more nucleation will take place. Typically set similar in magnitude to α.

P_N Probability of nucleation occurring in a given cell in which according to Δh_N it may occur; typical value 10^{-3} to 10^{-6}. P_N in combination with Δh_N together determine the frequency of nucleation. If P_N is zero, screw dislocations leading to spiral growth are the only growth mechanism; if P_N is large, the surface is rough.

Δh_G Threshold of difference in height with the neighbors for there to be an active neighbor. There must be at least one active neighbor for a site to be a kink and so to have growth in a cell. Physically, this parameter in combination with α determines the frequency of screw dislocations. Typical values to produce spiral growth are 0.4 to 0.8. If Δh_G is large, spiral growth is suppressed and growth proceeds by layers. If Δh_G is small, growth fronts that encounter one another cross to produce edge dislocations.

R Radius of the circle of neighbors, typically set to between 3 and 10. The model begins with a randomized grid [175]: A point is set at random within each cell at the beginning of the simulation. Subsequently the neighbors of the cell are sought by tracing a circle of radius R about this point. Owing to the initial random positioning of the center of the circle, this procedure produces a varying number of neighbors per cell. As with α, the randomization introduced with the grid here is related to the non-identical nature of the chitin crystallites which are the growth units for the nacre. A larger radius R implies wider terraces between growth steps. This is physically related to the surface diffusion of the growth units. If we look

at nacre from different species, we indeed find that some have steeper, narrower terraces, and others shallower, wider ones.

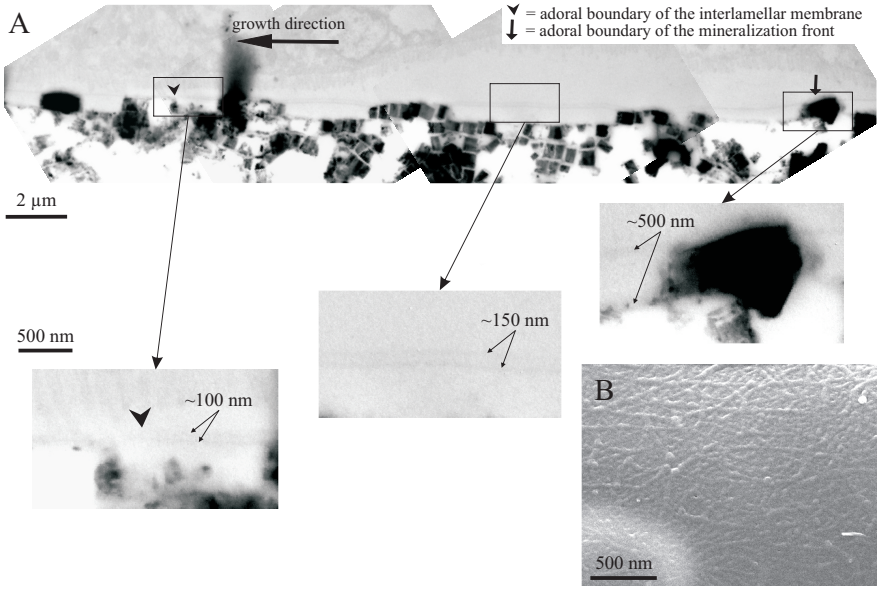

FIGURE 12.3: (A) Transmission electron micrographs show the interlamellar membranes being laid down prior to mineralization in *Pinctada radiata*; the orientation of the sample is as in Figure 12.2. The blowups provide more detail of the membranes and show that the initial spacing of $\sim$100 nm when a fresh layer is laid down gradually increases to $\sim$500 nm in mineralized nacre over a distance of some 20 μm. We have surmised elsewhere that this increase in layer spacing accompanies the coating of the chitin liquid-crystal layers with proteins prior to mineralization and is likely caused by an additional repulsion term in the force balance between membranes introduced by the electrostatic charges on the amphiphilic structure of the mature membrane. This change in the force balance from the original cholesteric liquid crystal to the mature membrane covered with protein would serve to repel the membrane from its neighboring interlamellar membrane [156]. (B) Scanning electron micrograph of the interlamellar membrane of *Anodonta cygnea* shows its logjam structure when viewed from above. When interpreting this image one must bear in mind various points. This is a completed interlamellar membrane seen in plan view; we are not just looking at chitin, but at the result of a later stage of nacre formation in which the chitin has become coated with protein. This stabilizes the layer, which is why we are able to see it in this micrograph, for which the sample has inevitably been subjected to drying, which must disintegrate the uncoated initial state of the chitin layer.

In Figure 12.4 we display the evolution in time of three different scenarios in our model, to be compared to the various phenomena in nacre of Figure 12.1. In each case the simulation began at time zero with a flat surface of zero height. In Figure 12.4A we show the evolution of target patterns; we see the system after 87 and 93 iterations respectively. Each terrace expands laterally and once the uppermost terrace has expanded sufficiently a fresh terrace nucleates on it. This is similar to what is seen in Figure 12.1B in nacre and corresponds to island growth, the first process of Burton–Cabrera–Frank. In Figure 12.4B we show after 300 and 310 iterations colliding growth fronts and an evolving spiral similar to those seen in nacre in Figure 12.1C. As the spiral rotates and grows out it meets other growth fronts coming from top right. The fronts of the same height annihilate each other by joining seamlessly as they meet. Lastly in Figure 12.4C we show after 230 and 250 iterations paired spirals similar to those in the nacre of Figs 12.1D and E. Figures 12.4B and C correspond to spiral growth;, which is the second process of Burton–Cabrera–Frank. Those in B are single screw dislocations, while the paired spirals in C are Frank–Read sources.

These time evolutions can be seen in nacre samples by looking down through the nacre layers, as the third dimension of space — into the material — is equivalent to time. But although that procedure takes us back in time, it does not indicates which events are coeval, as the model does. From our model we can see that Wada was correct in noting the parallel between nacre growth and the Burton–Cabrera–Frank dynamics (in fact Wada [166] singled out the spiral growth mechanism that was Frank's contribution [173]) of layer growth, albeit for a liquid crystal rather than the solid crystal he had envisaged.

12.3 Discussion

From our model of layer growth we can comprehend why these spiral and target patterns, familiar from such diverse instances as the Belousov-Zhabotinsky reaction in chemistry and ventricular fibrillation of the heart in biology, appear in nacre: All of these systems are describable in physical terms as excitable media [176]. Excitable media form a rather general class of systems in which there are elements that are quiescent until excited into an active state by some stimulus, after which they are unresponsive to further stimuli during some refractory period before returning to their initial quiescent, excitable state. This very simple physics is sufficient to produce complex spatiotemporal patterns of targets and spirals, which is why these patterns are observed so generally in many different fields. Here, the excitable paradigm holds too, and we can describe the growth of nacre as an excitable medium: A point on the surface of the last-formed layer is quiescent, but receptive to the nucleation of a new layer above it given a large enough perturbation, that is to say a fluctuation that concentrates sufficient material nearby to nucleate a new surface. The edges of layers, the kinks of steps, where new material is incorporated, are active, while just after a new layer has formed there is a

refractory period in which another new layer cannot be formed at that point, because material is preferentially incorporated at the growing edge of the layer nearby. Thus the growth dynamics of our model of the formation of interlamellar membranes of nacre corresponds to an excitable medium.

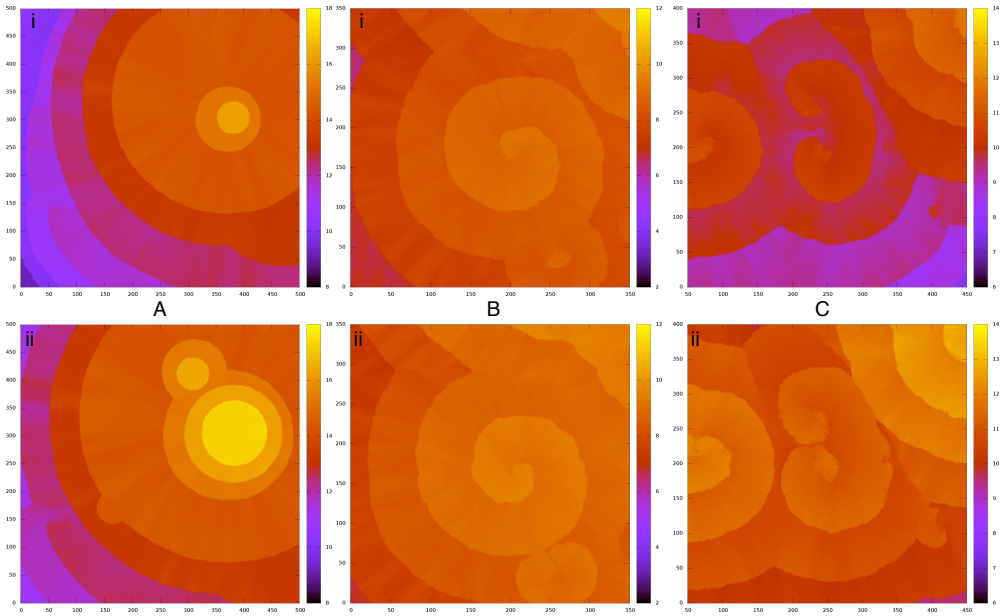

FIGURE 12.4: Our model of liquid-crystal layer growth reproduces the features seen in micrographs of nacre growth and shows — what cannot be seen in nacre samples — how they evolve in time: (A) Target patterns — cf. Fig. 12.1B — after (i) 87 and (ii) 93 iterations; parameters $\alpha = 0.08$, $\Delta h_N = 0.1$, $P_N = 10^{-3}$, $\Delta h_G = 0.8$, $R = 10$. (B) Colliding growth fronts and spiral — cf. Fig. 12.1C — after (i) 300 and (ii) 310 iterations; parameters $\alpha = 0.06$, $\Delta h_N = 0.06$, $P_N = 5 \times 10^{-6}$, $\Delta h_G = 0.6$, $R = 4$. (C) Paired spirals — cf. Figs. 12.1D & E — after (i) 230 and (ii) 250 iterations; parameters $\alpha = 0.08$, $\Delta h_N = 0.09$, $P_N = 10^{-4}$, $\Delta h_G = 0.8$, $R = 5$. The color scheme is shown alongside each subfigure; lighter is higher. Movies of these three cases can be found in the supplementary information.

The growth model we put forward here is for the formation of a liquid crystal of chitin that is the first component of nacre to be laid down. But nacre — by which we mean the completed product: mother of pearl, or a pearl itself — is no longer a liquid crystal but a complex solid. The problem of supramolecular assembly in biology — how does an organism assemble itself: after the cells make the molecules that are to form part of the structure, how do they form into tissue; flesh and bone? — is as yet in general unsolved. Nacre is of particular interest and is by far the most intensively studied non-human organo-mineral biocomposite. It lies at the intersection of two groups of

supramolecular biological structures: fibrous composites and biominerals. It is of interest not just because it is beautiful, but also because it is strong: with just five percent polysaccharide and protein, its work of fracture is up to 3 000 times higher than that of inorganic aragonite [155]. The importance of fluid dynamics in the organization of supramolecular biological structures, both in transporting materials and in their self-assembly, is beginning to be recognized [177]. Such is the case with biomineralization processes such as bone and fish otolith formation, and it is likely that further examples will come to light as our knowledge of the so-called 'soft chemistry' involved in biological mineral deposition improves. The extrapallial liquid is fundamental in the formation of nacre and it is probable that we shall in future find that there are active fluid dynamical processes involved in the transport of chitin crystallites, proteins and mineral to produce nacre.

Nacre is secreted by some species of four classes in the phylum Mollusca: Bivalvia, Gastropoda, Cephalopoda, and, to a minor extent, Tryblidiida. Although the material has many points in common between the classes — hence its general classification as nacre — at the level of details there are important differences. In the present case we have concentrated on bivalve nacre. The other large class of nacre secreting molluscs, the gastropods, possesses an additional feature not present in bivalves, the surface membrane, interposed between the mantle and the shell. This organizes the mineralization of gastropod nacre so that it grows in towers, rather than in the fronts of bivalve nacre [178]. Nonetheless gastropod interlamellar membranes have a similar geometry to those in the bivalves, and screw and edge dislocations are noted in gastropod nacre [156]; they are simply not so clearly visible at the growth surface as in bivalves, on account of gastropod mineralization being in towers rather than fronts that follow the leading edges of the membranes as in bivalves. It seems likely that our liquid-crystal growth model, possibly with some variations, should be applicable in gastropods too.

Today layer-by-layer growth of materials is of great technological interest; but the synthetic process employed is often a rather primitive one consisting of building up layers by dipping the material into first one component then another to produce a corresponding layering of so-called artificial nacre [179]. Nature, on the other hand, is more sophisticated in using a self-organized system of liquid crystallization to assemble nacre layer by layer. Liquid crystals have long been surmised to play an important role in the organization of biological tissues [180–182], yet without a model for their formation a key section of the argument that biological systems make use of liquid crystals for the self-organization of supramolecular structure has been lacking [183]. Here we have shown how such a biological liquid crystal may be constructed, and that this self-assembly is occurring through a novel process — novel, that is, to humans, as molluscs have been using it since the Cambrian — of liquid crystallization layer by layer. It may be of advantage in many technological applications to follow nature's way.

Chapter 13

Summary and Conclusions

This thesis presents several works related to non-linear dynamics pattern formation and morphology in nature. Due to the multidisciplinarity of the issues, I have separated the thesis in four independent parts. The link between them is non-linear dynamics, and the order chosen is from simplest to most complex.

The first part describes the synchronization effects generated by tidal interactions between planets and satellites as a phenomenon of non-linear dynamics. I study the synchronization between rotation and planetary orbit and its influence on the orbital parameters. I use a dynamic system, reducing the problem to their most basic physical principles and trying to reproduce the effects of tidal forces with numerical simulations based on a simplistic model.

Despite its simplicity, our model can reproduce most of the tidal effects present in our solar system without resorting to continuous bodies, which greatly simplifies the equations and makes them more intuitive. Thus, I can reproduce the spin-orbit synchronization between Earth and Moon as well as other known phenomena, such as the circularization of the orbits, the apasis precession and the synchronization into metastable orbits. Extensions of the model could eventually include more complexity in the secondary body or the tilt of its axis of rotation, which could have other synchronization effects not considered in this work.

The second part describes our experiments aimed at investigating the different morphologies in ice films at the mesoscopic scale. These experiments are relevant for the study of the astrophysical properties of ice, as porosity, which are a consequence of not only the interactions at the molecular level but also of the morphology at a mesoscopic level. More generally, this study examines the understanding of the fundamental physics involved in pattern formation in thin layers following non-linear dynamics. Originally our interest in this field came from the ability to grow and study amorphous ice films in an environmental scanning electron microscope. I are interested in studying

the dynamics involved in the formation of ice at extreme conditions and in finding evidence of the disputed phase transition between amorphous ice of low and high density.

As a result of our work I showed that the morphology of ice films grown by vapor deposition varies strongly with the surface temperature and vapor pressure. I apply the structure zone model to water ice, a material very different from those that inspired the model, confirming that this model is independent of the chemical nature of the compound. I obtained the first electron microscopy images of amorphous ice. The phase transition between amorphous ice low and high density did not show the expected change of morphology, but I did detect a large increase in pressure within the chamber at the proposed transition temperature. Finally, I found that the ice can form biomimetic structures in extreme conditions, which may be an important warning for astrobiologists looking for life in space under similar conditions.

In the third part of the thesis I extend the study of phenomena of nonlinear dynamics to more complex systems that combine physical and chemical processes, as is the case of chemical gardens. Despite these curiosities of science are not a recent phenomenon and usually are relegated to divulgative demonstrations, the complexity of the system combines various physical processes and chemical reactions of dissolution, precipitation and nucleation, which complicates their understanding globally. Our interest in this field came when I were presented with the opportunity of growing chemical gardens in microgravity aboard the International Space Station. To better understand the physical and chemical processes responsible for the morphology of these biomimetic patterns, I studied the formation, structure and composition of chemical gardens grown from different metal salts in different growing conditions and using a variety of experimental techniques.

Among the conclusions reached, it is noteworthy that the relationship between osmosis and buoyancy depends strongly on the salt used as seed and the concentration of the silicate solution, which defines the patterns and morphologies formed during growth. The mechanical properties of the osmotic membrane also depend heavily on the chemical composition. The viscosity of the solution affects the shape and growth rate of the tubes. Higher viscosity means less reaction time, but too dilute solutions produce weak membranes and unstable tubes. The reactivity and morphology change in microgravity, but not the osmotic pressure. Better control of fluid dynamics, relative densities between the solutions and osmotic pressure could lead to the production of microtube design with controlled morphology and thickness.

In the last part of the thesis I present our work on pattern formation in the surface of nacre as a process of non-linear dynamics. Much remains to be understood in terms of the mechanisms involved in the formation of the microstructure of nacre. A better understanding of this process could allow the possibility of artificial nacre growth with a wide range of applications. The problem arises as a clear example of pattern formation in self-organized bio-mineralization.

This work proposes and validates a model of growth of liquid crystals in two dimensions by self-organization. Using cellular automata, I developed a simple mathematical model based on the most basic physical interactions between chitin crystals. The model can reproduce the patterns formed on the surface of nacre and helps to demonstrate that such patterns can be defined by the interlamellar membranes. Among other things, I found that the laminar organization of the membranes can be explained as a process of deposition of a cholesteric liquid crystal phase without enough time to reach its equilibrium. I also showed that the patterns observed in bivalve nacre are similar to those found in solid crystals in two dimensions, and that they can be explained using the theories of Burton-Cabrera-Frank.

Chapter 14

Resumen y Conclusiones

En esta tesis se presentan varios trabajos relacionados con la dinámica no-lineal en la formación de patrones y morfologías en la naturaleza. Debido a la multidisciplinariedad de los temas tratados, hemos separado la tesis en cuatro partes independientes. El nexo de unión entre ellos es la dinámica no-lineal y el orden elegido es de más sencillo a más complejo.

La primera parte describe los efectos de sincronización generados por interacciones mareales entre planetas y satélites como fenómeno de dinámica no-lineal. Estudiamos la sincronización entre rotación y órbita planetaria y su influencia en los parámetros orbitales. Para ello utilizamos un sistema dinámico, reduciendo el problema a sus más básicos principios físicos e intentando reproducir los efectos de las fuerzas mareales con simulaciones numéricas basadas en un modelo simplista.

A pesar de su sencillez, nuestro modelo consigue reproducir la mayor parte de los efectos mareales presentes en nuestro sistema solar sin recurrir a cuerpos continuos, lo cual simplifica mucho las ecuaciones y las hace más intuitivas. De este modo, conseguimos reproducir la sincronización spin-órbita entre la Tierra y la Luna, así como otros fenómenos conocidos, como por ejemplo la circularización de las órbitas, la precesión del apáside o la sincronización en órbitas metaestables. Extensiones del modelo eventualmente podrían incluir mayor complejidad en el cuerpo secundario o la inclinación de su eje de rotación, lo cual podría presentar otros efectos de sincronización no considerados en este trabajo.

La segunda parte describe nuestros experimentos dirigidos a investigar las distintas morfologías en láminas de hielo a escala mesoscópica. Estos experimentos son relevantes para estudiar las propiedades astrofísicas del hielo, como la porosidad, que es consecuencia no sólo de las interacciones a nivel molecular sino también de la morfología a nivel mesoscópico. De manera más general, este trabajo profundiza en el entendimiento de la física fundamental involucrada en la formación de patrones en láminas delgadas

siguiendo una dinámica no-lineal. Originalmente nuestro interés en este campo surgió de la posibilidad de crecer y estudiar láminas de hielo amorfo dentro de un microscopio electrónico ambiental. Estabamos interesados en estudiar la dinámica involucrada en la formación de hielo en condiciones extremas y en encontrar una evidencia de la discutida transición de fase entre el hielo amorfo de alta y de baja densidad.

Como resultado de nuestro trabajo demostramos que la morfología de películas de hielo crecidas por deposición de vapor varía fuertemente con la temperatura de la superficie y la presión del vapor depositado. Aplicamos el modelo de zonas de estructura por primera vez al hielo, un material muy diferente de aquellos que inspiraron el modelo, corroborando que dicho modelo es independiente de la naturaleza química del compuesto. Obtuvimos las primeras primeras imágenes de microscopía electrónica del hielo amorfo. La transición de fase entre el hielo amorfo de baja y alta densidad no mostró el cambio de morfología esperado, pero sí se observó un gran incremento de la presión dentro de la cámara a la temperatura de la transición. Por último, encontramos que el hielo puede formar estructuras biomiméticas en condiciones extremas, lo cual puede ser un aviso importante para astrobiólogos buscando vida en el espacio en condiciones similares.

En la tercera parte de la tesis extendemos el estudio de fenómenos de dinámica no-lineal en sistemas más complejos donde se combinan procesos químicos y físicos, como es el caso de los jardines químicos. A pesar de que estas curiosidades de la ciencia no son un fenómeno reciente y normalmente quedan relegadas a las demostraciones divulgativas, la complejidad del sistema combina diferentes procesos físicos y reacciones químicas de disolución, precipitación y nucleación, lo cual complica su entendimiento de forma global. Nuestro interés en este campo surgió cuando se nos presentó la oportunidad de realizar experimentos de crecimiento de jardines químicos en microgravedad a bordo de la Estación Espacial Internacional. Para mejor entender los procesos físicos y químicos responsables de la morfología de estos patrones biomiméticos, hemos estudiado el proceso de formación, la estructura y la composición de jardines químicos crecidos a partir de diferentes sales metálicas, en diferentes condiciones de crecimiento y utilizando una gran variedad de técnicas experimentales.

Entre las conclusiones alcanzadas, cabe destacar que la relación entre ósmosis y flotabilidad depende fuertemente de la sal utilizada como semilla y de la concentración de la disolución de silicato, lo cual define los patrones y morfologías formadas durante el crecimiento. Las propiedades mecánicas de la membrana osmótica también dependen en gran medida de la composicón química. La viscosidad de la disolución afecta a la forma y velocidad de crecimiento de los tubos. Mayor viscosidad implica menor velocidad de reacción, pero disoluciones demasiado diluídas producen membranas débiles y tubos inestables. La reactividad y la morfología cambian en microgravedad, aunque no la presión osmótica. Un mejor control de la dinámica de fluídos, de las densidades relativas entre las disoluciones y de la presión osmótica podrían llevar a la producción de microtubos de diseño, con morfología y grosor controlados.

En la última parte de la tesis presentamos nuestro trabajo sobre la formación de patrones en el nácar dentro de un proceso de dinámica no-lineal. Este último caso es más complejo que los anteriores porque involucra la química, física y biología de los procesos de biomineralización. Todavía queda mucho por entender en cuanto a los mecanismos que intervienen en la formación de la microestructura del nácar. Un mejor entendimiento de este proceso podría permitir la posibilidad de crecer nácar artificial con una gran diversidad de aplicaciones. El problema se plantea como un claro ejemplo de formación de patrones auto-organizados en biomineralización.

En este trabajo se propone y valida un modelo de crecimiento de cristales líquidos en dos dimensiones por auto-organización. Usando autómatas celulares, desarrollamos un simple modelo matemático basado en las interacciones físicas más básicas entre cristales de quitina. El modelo consigue reproducir los patrones formados en la superficie del nácar y ayuda a demostrar que dichos patrones pueden ser definidos por las membranas interlamelares. Entre otras cosas, encontramos que la organización laminar de las membranas se puede explicar como un proceso de deposición de una fase colestérica de cristal líquido que no tiene tiempo para alcanzar el equilibrio. También demostramos que los patrones observados en el nácar de bivalvos son semejantes a los encontrados en cristales sólidos en dos dimensiones, y que se pueden explicar utilizando las teorías de Burton-Cabrera-Frank.

Bibliography

[1] Martin Chaplin. Water structure and science. `http://www1.lsbu.ac.uk/water`.

[2] Creation of molecules. `http://mbscientific.org`.

[3] A. M. Turing. The chemical basis of morphogenesis. *Phil. Trans. Roy. Soc. Lond. B*, 237:37–72, 1952.

[4] H. Meinhardt. *The Algorithmic Beauty of Sea Shells*. Springer, New York, 1995.

[5] Department of Physics Faculty of Science and Engineering. Chuo University. `http://www.phys.chuo-u.ac.jp`.

[6] Maine Natural Areas Program. `http://www.maine.gov/doc/nrimc/mnap`.

[7] Department of Atmospheric and Environmental Sciences. University of Albany. `http://www.atmos.albany.edu/`.

[8] T. A. Witten Jr. and L. M. Sander. Diffusion-limited aggregation, a kinetic critical phenomenon. *Phys. Rev. Lett.*, 47:1400, 1981.

[9] Brian Romans. Clastic detritus. `http://clasticdetritus.com`.

[10] Stanford university. `http://www.stanford.edu`.

[11] R. A. Bagnold. *The Physics of Blown Sand and Desert Dunes*. Methuen, London, 1941.

[12] J. P. Grotzinger and D. H. Rothman. An abiotic model for stromalite morphogenesis. *Nature*, 383:423, 1996.

[13] D. S. McKay, E. K. Gibson, K. L. Thomas-Keprta, L. H. Vali, C. S. Romanek, S. J. Clemett, Z. D. F. Chillier, C. R. Maechling, and R.N. Zare. Search for past life on Mars: possible relic biogenic activity in Martian meteorite ALH84001. *Science*, 273:924–926, 1996.

[14] C. D. Murray and S. F. Dermott. *Solar system dynamics*. 1999.

[15] E. Roche. La figure d'une masse fluide soumise l'attraction d'un point loign. *Acad. des sciences de Montpellier*, 1:243, 1848.

[16] W. Munk and M. Dziechiuch. Millennial Climate Variability: Is There a Tidal Connection? *Journal of Climate*, 15:370–385, 2002.

[17] J. O. Dickey *et al.* Lunar Laser ranging: a continuing legacy of the Apollo program. *Science*, 265:482–490, 1994.

[18] Nasa Astrobiology Institute. `http://astrobiology.nasa.gov`.

[19] I. Dobbs-Dixon, D. N. C. Lin, and R. A. Mardling. Spin-Orbit Evolution of Short-Period Planets. *Astrophys. J.*, 610:464–476, 2004.

[20] R. A. Mardling. The Role of Chaos in the Circularization of Tidal Capture Binaries. I. The Chaos Boundary. *Astrophys. J.*, 450:722–+, September 1995. doi: 10.1086/176178.

[21] G. J. F. MacDonald. Tidal Friction. *Reviews of Geophysics*, 2:467–541, 1964. doi: 10.1029/RG002i003p00467.

[22] P. Goldreich and S. Soter. Q in the Solar System. *Icarus*, 5:375–389, 1966. doi: 10.1016/0019-1035(66)90051-0.

[23] B. Gladman, D. Dane Quinn, P. Nicholson, and R. Rand. Synchronous Locking of Tidally Evolving Satellites. *Icarus*, 122:166–192, July 1996. doi: 10.1006/icar.1996.0117.

[24] A. Celletti and L. Chierchia. Hamiltonian Stability of Spin Orbit Resonances in Celestial Mechanics. *Celestial Mechanics and Dynamical Astronomy*, 76:229–240, May 2000. doi: 10.1023/A:1008341317257.

[25] A. C. M. Correia and J. Laskar. Mercury's capture into the 3/2 spin-orbit resonance as a result of its chaotic dynamics. *Nature*, 429:848–850, June 2004. doi: 10.1038/nature02609.

[26] A. Celletti, C. Froeschlé, and E. Lega. Dynamics of the conservative and dissipative spin orbit problem. *Planet. Space Sci.*, 55:889–899, May 2007. doi: 10.1016/j.pss.2006.11.023.

[27] F. A. Rasio, C. A. Tout, S. H. Lubow, and M. Livio. Tidal Decay of Close Planetary Orbits. *Astrophys. J.*, 470:1187–+, October 1996. doi: 10.1086/177941.

[28] A. Babiano, J. H. E. Cartwright, O. Piro, and A. Provenzale. Dynamics of a small neutrally buoyant sphere in a fluid and targeting in Hamiltonian systems. *Phys. Rev. Lett.*, 84:5764–5767, 2000.

[29] J. H. E. Cartwright, M. O. Magnasco, O. Piro, and I. Tuval. Bailout Embeddings and Neutrally Buoyant Particles in Three-Dimensional Flows. *Physical Review Letters*, 89(26):264501–+, December 2002. doi: 10.1103/PhysRevLett.89.264501.

[30] J. H. E. Cartwright, M. O. Magnasco, O. Piro, and I. Tuval. Noise-induced order out of chaos by bailout embedding. *Fluct. Noise Lett.*, 2:161–174, 2002.

[31] J. V. Jose and E. J. Saletan. *Classical dynamics : a contemporary approach*. 1998.

[32] G. H. Darwin. *Tidal Friction and Cosmogony*. Cambridge University Press, 1908.

[33] J. D. Murray. *Mathematical Biology*. Springer, 1989.

[34] B. Escribano, J. Vanyo, I. Tuval, J. H. E. Cartwright, D. L. González, O. Piro, and T. Tél. Dynamics of tidal synchronization and orbit circularization of celestial bodies. *Phys. Rev. E*, 78:036216, 2008.

[35] P. Hut. Tidal evolution in close binary systems. *Astron. Astrophys.*, 99:126–140, 1981.

[36] T. A. Hurford and R. Greenberd. Tidal evolution by elongated primaries: Implications for the ida/dactyl system. *Geophys. Res. Letters*, 27:1595–1598, 2000.

[37] R. A. Mardling. The Role of Chaos in the Circularization of Tidal Capture Binaries. II. Long-Time Evolution. *Astrophys. J.*, 450:732–+, September 1995. doi: 10.1086/176179.

[38] M.G. Witte and G. J. Savonije. Orbital evolution by dynamical tides in the solar type stars. *Astron. Astrophys.*, 386:222–236, 2002.

[39] W. H. Munk and G. J. F. MacDonald. *The Rotation of the Earth: A Geophysical Discussion*. Cambridge University Press, 1975.

[40] E. Ott. *Chaos in Dynamical Systems*. Cambridge University Press, 2002.

[41] T. Tél and M. Gruiz. *Chaotic Dynamics, An introduction based on classical mechanics*. Cambridge University Press, 2006.

[42] L. D. Landau and E. M. Lifshitz. *Course of Theoretical Physics — Mechanics*, volume 1. Pergamon Press, 1981.

[43] S. A. Levin and L. A. Segal. Hypothesis for the origin of plankton patchiness. *Nature*, 259:659, 1976.

[44] C. Sarasola, A. d'Anjou, F. J. Torrealdea, and A. Moujahid. Energy-like functions for some dissipative chaotic systems. *Int. J. Bifurcation and Chaos*, 15: 2507–2521, 2005.

[45] C. G. Salzmann, P. G. Radaelli, E. Mayer, and J. L. Finney. Ice xv: A new thermodynamically stable phase of ice. *Phys. Rev. Lett.*, 103:105701, 2009.

[46] P. Jenniskens and D. F. Blake. Structural transitions in amorphous water ice and astrophysical implications. *Science*, 265:753–756, 1994.

[47] P. G. Debenedetti. Supercooled and glassy water. *J. Phys. Condens. Matter*, 15: 1669–1726, 2003.

[48] J. Kepler. *Strena, Seu, de Nive Sexangula*. 1611. Translation: The Six-Cornered Snowflake, (Oxford University Press, 1966).

[49] F. C. Frank. Snow Crystals. *Contemporary Physics*, 23:3–+, January 1982.

[50] B. J. Mason. Snow crystals, natural and man made. *Contemporary Physics*, 33: 227–+, July 1992.

[51] U. Nakaya. Snow Crystals. *American Journal of Physics*, 22:573–573, November 1954. doi: 10.1119/1.1933845.

[52] Yoshinori Furukawa. Fascination of snow crystals. `http://www.lowtem.hokudai.ac.jp/ptdice/english/aletter.html`.

[53] H. E. Stanley, S. V. Buldyrev, M. Canpolat, M. Meyer, O. Mishima, M. R. Sadr-Lahijany, A. Scala, and F. W. Starr. The puzzling statistical physics of liquid water. *Physica A*, 257:213–232, 1998.

[54] P. G. Debenedetti and H. E. Stanley. Supercooled and glassy water. *Phys. Today*, 56:40–46, 2003.

[55] P. Brüggeller and E. Mayer. Complete vitrification in pure liquid water and dilute aqueous solutions. *Nature*, 288:569–571, 1980.

[56] E. Mayer and P. Brüggeller. Vitrification of pure liquid water by high pressure jet freezing. *Nature*, 298:715–718, 1982.

[57] E. F. Burton and W. F. Oliver. The crystal structure of ice at low temperatures. *Proc. Roy. Soc. Lond. A*, 153:166–172, 1935.

[58] A. H. Narten, C. G. Venkatesh, and S. A. Rice. Diffraction pattern and structure of amorphous solid water at 10 and 77 K. *J. Chem. Phys.*, 64:1106–1121, 1976.

[59] D. E. Brown, S. M. George, C. Huang, E. K. L. Wong, K. B. Rider, R. S. Smith, and B. D. Kay. H_2O condensation coefficient and refractive index for vapor-deposited ice from molecular beam and optical interference measurements. *J. Phys. Chem.*, 100:4988–4995, 1996.

[60] National Institute for Materials Science (NIMS). Water polyamorphism. `http://www.nims.go.jp/water/top.html`.

[61] O. Mishima, L. D. Calvert, and E. Whalley. 'Melting ice' I at 77 K and 10 kbar: A new method of making amorphous solids. *Nature*, 310:393–395, 1984.

[62] O. Mishima, L. D. Calvert, and E. Whalley. An apparently first-order transition between two amorphous phases of ice induced by pressure. *Nature*, 314:76–78, 1985.

[63] A. Bizid, L. Bosio, A. Defrain, and M. Oumezzine. Structure of high-density amorphous water. I. X-ray diffraction study. *J. Chem. Phys.*, 87:2225–2230, August 1987.

[64] D. D. Klug, C. A. Tulk, E. C. Svensson, and C.-K. Loong. Dynamics and Structural Details of Amorphous Phases of Ice Determined by Incoherent Inelastic Neutron Scattering. *Physical Review Letters*, 83:2584–2587, September 1999. doi: 10.1103/PhysRevLett.83.2584.

[65] J. L. Finney, A. Hallbrucker, I. Kohl, A. K. Soper, and D. T. Bowron. Structures of High and Low Density Amorphous Ice by Neutron Diffraction. *Physical Review Letters*, 88(22):225503–+, June 2002. doi: 10.1103/PhysRevLett.88.225503.

[66] M. A. Floriano, E. Whalley, E. C. Svensson, and V. F. Sears. Structure of high-density amorphous ice by neutron diffraction. *Physical Review Letters*, 57:3062–3064, December 1986. doi: 10.1103/PhysRevLett.57.3062.

[67] M.-C. Bellissent-Funel, J. Teixeira, and L. Bosio. Structure of high-density amorphous water. II. Neutron scattering study. *J. Chem. Phys.*, 87:2231–2235, August 1987.

[68] P. Jenniskens, D. F. Blake, M. A. Wilson, and A. Pohorille. High-density amorphous ice, the frost on interstellar grains. *Astrophys. J.*, 455:389–401, 1995.

[69] O. Mishima and H. E. Stanley. The relationship between liquid, supercooled and glassy water. *Nature*, 396:329–335, 1998.

[70] G. P. Johari, A. Hallbrucker, and E. Mayer. Two calorimetrically distinct states of liquid water below 150 Kelvin. *Science.*, 273:90–92, 1996.

[71] O. Mishima. Reversible first-order transition between two H_2O amorphs at $\sim$0.2 GPa and $\sim$135 K. *J. Chem. Phys.*, 100:5910–5912, 1994.

[72] O. Mishima, K. Takemura, and K. Aoki. Visual Observations of the Amorphous-Amorphous Transition in H_2O Under Pressure. *Science*, 254:406–408, October 1991.

[73] O. Mishima and Y. Suzuki. Propagation of the polyamorphic transition of ice and the liquid–liquid critical point. *Nature*, 419:599–603, 2002.

[74] M. M. Koza, H. Schober, H. E. Fischer, T. Hansen, and F. Fujara. Kinetics of the high- to low-density amorphous water transition. *Journal of Physics Condensed Matter*, 15:321–332, January 2003. doi: 10.1088/0953-8984/15/3/301.

[75] C. A. Tulk, C. J. Benmore, J. Urquidi, D. D. Klug, J. Neuefeind, B. Tomberli, and P. A. Egelstaff. Structural studies of several distinct metastable forms of amorphous ice. *Science*, 297:1320–1323, 2002.

[76] T. Loerting, C. Salzmann, I. Kohl, E. Mayer, and A. Hallbrucker. A second distinct structural state of high-density amorphous ice at 77 K and 1 bar. *Phys. Chem. Chem. Phys.*, 3:5355–5357, 2001.

[77] J. L. Finney, D. T. Bowron, A. K. Soper, T. Loerting, E. Mayer, and A. Hallbrucker. Structure of a New Dense Amorphous Ice. *Physical Review Letters*, 89 (20):205503–+, October 2002. doi: 10.1103/PhysRevLett.89.205503.

[78] S. Klotz, G. Hamel, J. S. Loveday, R. J. Nelmes, M. Guthrie, and A. K. Soper. Structure of High-Density Amorphous Ice under Pressure. *Physical Review Letters*, 89:B5502+, December 2002. doi: 10.1103/PhysRevLett.89.285502.

[79] K. P. Stevenson, G. A. Kimmel, Z. Dohnálek, R. S. Smith, and B. D. Kay. Controlling the morphology of amorphous solid water. *Science*, 283:1505–1507, 1999.

[80] Z. Dohnálek, G. A. Kimmel, R. L. Ciolli, K. P. Stevenson, R. S. Smith, and B. D. Kay. The effect of the underlying substrate on the crystallization kinetics of dense amorphous solid water films. *J. Chem. Phys.*, 112:5932–5941, 2000.

[81] G. A. Kimmel, K. P. Stevenson, Z. Dohnálek, R. S. Smith, and B. D. Kay. Control of amorphous solid water morphology using molecular beams: I. Experimental results. *J. Chem. Phys*, 114:5284–5294, 2001.

[82] G. A. Kimmel, Z. Dohnálek, K. P. Stevenson, R. S. Smith, and B. D. Kay. Control of amorphous solid water morphology using molecular beams: II. Ballistic deposition simulations. *J. Chem. Phys*, 114:5295–5303, 2001.

[83] D. Laufer, E. Kochavi, and A. Bar-Nun. Structure and dynamics of amorphous water ice. *Phys. Rev. B*, 36:9219–9227, 1987.

[84] A. G. G. M. Tielens. *The Physics and Chemistry of the Interstellar Medium*. The Physics and Chemistry of the Interstellar Medium, 2005.

[85] P. Ehrenfreund, H. J. Fraser, J. Blum, J. H. E. Cartwright, J. M. García-Ruiz, E. Hadamcik, A. C. Levasseur-Regourd, S. Price, F. Prodi, and A. Sarkissian.

Physics and chemistry of icy particles in the universe: answers from microgravity. *Planet. Space Sci.*, 51:473–494, 2003.

[86] E. F. van Dishoeck. *Ann. Rev. Astron. Astrophys.*, 42:119, 2004.

[87] M. Ohring. *The Materials Science of Thin Films*. Academic Press, second edition, 2001.

[88] A. Lakhtakia and R. Messier. *Sculptured Thin Films: Nanoengineered Morphology and Optics*. SPIE, 2005.

[89] V. F. Petrenko and R. W. Whitworth. *Physics of Ice*. Oxford University Press, 1999.

[90] G. P. Johari and O. Andersson. *Thermochim. Acta*, 461:14, 2007.

[91] J. H. E. Cartwright. Solar and stellar physics through eclipses. In S. O. Selam O. Demircan and B. Albayrak, editors, *ASP Conference Series*, pages 265–69, 2007.

[92] T. Loerting and N. Giovambattista. *J. Phys.*, 18:R919, 2006.

[93] Kumar P. Xu L. Yan Z. Mazza M. G. Buldyrev S. V. Stanley, H. E. *Physica A*, 386:729, 2007.

[94] R. Messier, V. C. Venugopal, and P. D. Sunal. Origin and evolution of sculptured thin films. *J. Vac. Sci. Technol. A*, 18:1538–1545, 2000.

[95] A. F. Jankowski and J. P. Hayes. Sputter deposition of a spongelike morphology in metal coatings. *J. Vac. Sci. Technol. A*, 21:422–425, 2003.

[96] K. G. Libbrecht. The physics of snow crystals. *Rep. Prog. Phys.*, 68:855–895, 2005.

[97] R. Bukowski, K. Szalewicz, G. C. Groenenboom, and A. van der Avoird. Predictions of the properties of water from first principles. *Science*, 315:1249–1252, 2007.

[98] G. A. Kimmel, K. P. Stevenson, Z. Dohnálek, R. S. Smith, and B. D. Kay. Control of amorphous solid water morphology using molecular beams: I. Experimental results. *J. Chem. Phys*, 114:5284–5294, 2001.

[99] P. A. Sánchez, T. Sintes, J. H. E. Cartwright, and O. Piro. Effects of microstructures on mesoscopic morphological transitions in deposition growth models. *Proc. R. Soc. A*, 465:3875–3884, 2009.

[100] T. Kondo, H. S. Kato, M. Bonn, and M. Kawai. *J. Chem. Phys*, 127:094703, 2007.

[101] A. Hornekaer, A. Baurichter, V. V. Petrunin, A. C. Luntz, B. D. Kay, and A. Al-Halabi. *J. Chem. Phys.*, 124:124701, 2005.

[102] L. Colangeli, J. R. Brucato, A. Bar-Nun, R. L. Hudson, and M. H. Moore. In M. C. Festou et al., editor, *Comets II*, pages 695–717. University of Arizona Press, 2004.

[103] M. E. Palumbo. *J. Phys.: Conf. Series*, 6:211, 2005.

[104] C. Hill and P. Forti. *Cave Minerals of the World*. Natl. Speleological Soc., 1997.

[105] J. B. Corliss, J. Dyamond, L. I. Gordon, J. M. Edmond, R. P. V. Herzen, K. Green, D. Williams, A. Bainbridge, K. Crane, and T. H. Van Andel. *Science*, 203:1073–1083, 1979.

[106] R. D. Coatman, N. L. Thomas, and D. D. Double. Studies of the growth of "silicate gardens" and related phenomena. *J. Mater. Sci.*, 15:2017–2026, 1980.

[107] R. Grün. Electron spin resonance (ESR) dating. *Nature*, 338:543–544, 1989.

[108] Wittenberg University Speleological Society. `http://www.wusscavers.com`.

[109] P. P. Provencio and V. J. Polyak. *Geomicrobiol. J.*, 18:297–309, 2001.

[110] E. S. Barghoorn and S. A. Tyler. *Science*, 147:563–577, 1965.

[111] E. Bonucci. *Calcification in Biological Systems*. CRC, 1992.

[112] R. D. Barnes. *Invertebrate Zoology*. Harcourt Brace Jovanovich, Inc., 1987.

[113] J. L. Sumich. *An Introduction to the Biology of Marine Life*. Wm. C. Brown.., 1996.

[114] Department of Geology. University of Kerala. Marine ecosystem. `http://dgukenvis.nic.in`.

[115] M. L. Jones. Riftia pachyptila jones: Observations on the vestimentiferan worm from the galápagos rift. *Science*, 213:333–336, 1981.

[116] Woods Hole Oceanographic Institution. `http://www.whoi.edu`.

[117] A. Koschinsky, D. Garbe-Schönberg, S. Sander, K. Schmidt, H.H. Gennerich, and H. Strauß. Hydrothermal venting at pressure-temperature conditions above the critical point of seawater, 5S on the Mid-Atlantic Ridge. *Geology*, 36:615–618, 2008.

[118] S. Perkins. New type of hydrothermal vent looms large. *Science News*, 160, 2001.

[119] J.R. Delaney, V. Robigou, R.E. McDuff, and M.K. Tivey. Geology of a vigorous hydrothermal system on the Endeavour segment, Juan de Fuca Ridge. *Journal of Geophysical Research*, 97:19663–19682, 1992.

[120] G. Wächtershäuser. Pyrite formation, the first energy source for life: a hypothesis. *Syst. Appl. Microbiol.*, 10:207–210, 1988.

[121] W. Martin and M. J. Russell. On the origins of cells: a hypothesis for the evolutionary transitions from abiotic geochemistry to chemoautotrophic prokaryotes, and from prokaryotes to nucleated cells. *Phil. Trans. R. Soc. Lond. B*, 358:59–85, 2003.

[122] J. R. Glauber. *Furni Novi Philosophici*. Amsterdam, 1646.

[123] S. Leduc. *The Mechanism of Life*. Rebman, London, 1911.

[124] B. Stockwell and A. Williams. Experiment in space. *School Sci. Rev.*, 76:7–14, 1994.

[125] G. L. Früh-Green *et al.* 30,000 years of hydrothermal activity at the lost city vent field. *Science*, 301:495–498, 2003.

[126] G. Proskurowski, M. D. Lilley, J. S. Seewald, G. L. Früh-Green, E. J. Olson, J. E. Lupton, S. P. Sylva, and D. S. Kelley. Abiogenic hydrocarbon production at lost city hydrothermal field. *Science*, 319:604–607, 2008.

[127] W. Martin and M. J. Russell. On the origin of biochemistry at an alkaline hydrothermal vent. *Phil. Trans. R. Soc. B*, 362:1887–1926, 2007.

[128] Modern Mechanix. `http://www.modernmechanix.com`.

[129] J. H. E. Cartwright and O. Piro. The dynamics of Runge–Kutta methods. *Int. J. Bifurcation and Chaos*, 2:427–49, 1992.

[130] D. D. Double and A. Hellawell. The hydration of Portland cement. *Nature*, 261: 486–488, 1976.

[131] M. G. Fontana. *Corrosion Engineering*. McGraw-Hill, third edition, 1986.

[132] M. J. Russell and A. J. Hall. The emergence of life from iron monosulphide bubbles at a submarine hydrothermal redox and pH front. *J. Geol. Soc. Lond.*, 154:377–402, 1997.

[133] C. Ritchie, G. J. T. Cooper, Y.-F. Song, C. Streb, H. Yin, A. D. C. Parenty, D. A. MacLaren, and L. Cronin. Spontaneous assembly and real-time growth of micrometre-scale tubular structures from polyoxometalate-based inorganic solids. *Nature Chem.*, 1:47–52, April 2009. doi: 10.1038/nchem.113.

[134] M. Traube. Experimente zur Theorie der Zellenbildung und Endosmose. *Archiv. Anat. u. Physiol.*, pages 87–165, 1867.

[135] W. Pfeffer. *Osmotic Investigations*. Van Nostrand Reinhold, 1985.

[136] C. Collins, W. Zhou, A. Mackay, and J. Klinowski. The 'silica garden': a hierarcharical nanostructure. *Chem. Phys. Lett.*, 286:88–92, April 1998. doi: 10.1016/S0009-2614(98)00081-5.

[137] C. Collins, W. Zhou, and J. Klinowski. A unique structure of $Cu_2(OH)_3NH_3$ crystals in the 'silica garden' and their degradation under electron beam irradiation. *Chem. Phys. Lett.*, 306:145–148, June 1999. doi: 10.1016/S0009-2614(99)00438-8.

[138] D. Balköse, F. Özkan, U. Köktürk, S. Ulutan, S. Ülkü, and G. Nişli. Characterization of Hollow Chemical Garden Fibers from Metal Salts and Water Glass. *J. Sol-Gel Sci. Technol.*, 23:253–263, 2002.

[139] S. Thouvenel-Romans and O. Steinbock. Oscillatory Growth of Silica Tubes in Chemical Gardens. *J. Am. Chem. Soc.*, 125:4338–4341, 2003.

[140] B. Martin, A. Tharrington, and X. l. Wu. Chiral symmetry breaking in crystal growth: Is hydrodynamic convection relevant? *Phys. Rev. Lett.*, 77:2826–2829, 1996.

[141] D. Böschel, M. Janich, and H. Roggendorf. Size distribution of colloidal silica in sodium silicate solutions investigated by dynamic light scattering and viscosity measurements. *J. Coll. Interface Sci.*, 267:360–368, 2003.

[142] S. W. Jones, O. M. Thomas, and H. Aref. Chaotic advection by laminar flow in a twisted pipe. *J. Fluid Mech.*, 209:335–357, 1989.

[143] S. Thouvenel–Romans, J. Pagano, and O. Steinbock. Bubble guidance of tubular growth in reaction–precipitation systems. *Phys. Chem. Chem Phys.*, 7:2610–2615, 2005.

[144] The Dow Chemical Company. *Calcium Chloride handbook*. 2003.

[145] J. Pagano, Jr. T. Bánsági, and O. Steinbock. Bubble guidance of tubular growth in reaction–precipitation systems. *J. Phys. Chem. C*, 111:9324–9329, 2007.

[146] S. Thouvenel-Romans, W. van Saarloos, and O. Steinbock. Silica tubes in chemical gardens: Radius selection and its hydrodynamic origin. *Europhys. Lett.*, 67:42–48, July 2004. doi: 10.1209/epl/i2003-10279-7.

[147] A.B. Rodríguez-Navarro. XRD2DScan a new software for polycrystalline materials characterization using two-dimensional X-ray diffraction. *Journal of Applied Crystallography*, 39:905–909, 2006.

[148] J. H. E. Cartwright, B. Esrcibano, S. Khokhlov, and C. I. Sainz-Díaz. Chemical gardens from silicates and cations of group II: A comparative study of composition, morphology and microstructure. *Phys. Chem. Chem. Phys.*, page (submitted), 2010.

[149] Ying Tao, Baojun Zhu, and Zhenhua Chen. Chemical gardens from silicates and cations of group II: A comparative study of composition, morphology and microstructure. *Journal of Crystal Growth*, 293:382–386, 2006.

[150] H.D. Lutz, H. Möller, and M. Schmidt. Lattice vibration spectra. Part LXXXII. Brucite-type hydroxides M(OH)2 (M = Ca, Mn, Co, Fe, Cd) IR and Raman spectra, neutron diffraction of Fe(OH)2. *J. Mol. Struct.*, 328:121–132, 1994.

[151] Kaifu Zhong, Pu Jin, and Qianwang Chen. Ni Hollow Nanospheres: Preparation and Catalytic Activity. *Journal of Nanomaterials*, 2006:1–7, 2006.

[152] Pu Jin, Qianwang Chen, Liqing Hao, Ruifen Tian, Lixin Zhang, and Lin Wang. Synthesis and Catalytic Properties of Nickel-Silica Composite Hollow Nanospheres. *J. Phys. Chem. B*, 108:6311–6314, 2004.

[153] W. W. Mullins and R. F. Sekerka. Stability of a planar interface during solidification of a dilute binary alloy. *J. Appl. Phys.*, 35:444–451, 1964.

[154] L. Addadi and S. Weiner. A pavement of pearl. *Nature*, 389:912–915, 1997.

[155] A. P. Jackson, J. F. V. Vincent, and R. M. Turner. The mechanical design of nacre. *Proc R Soc London B*, 234:415–440, 1984.

[156] J.H.E. Cartwright and A.G. Checa. The dynamics of nacre self-assembly. *Journal of The Royal Society Interface*, 4:491–504, 2007.

[157] A. G. Checa, J. Ramirez-Rico, A. Ginzales-Segura, and A. Sanchez-Navas. Nacre and false nacre (foliated aragonite) in extant monoplacophorans. *Naturwissenschaften*, 96:111–122, 2009.

[158] S. Weiner and W. Traub. X-ray diffraction study of the insoluble organic matrix of mollusk shells. *FEBS letters*, 111:311–316, 1980.

[159] T. Imai, T. Watanabe, T. Yui, and J. Sugiyama. The directionality of chitin biosynthesis: A revisit. *Biochem. J*, 374:755–760, 2003.

[160] E. Belamie, P. Davidson, and M. Giraud-Guille. Structure and chirality of the nematic phase in α-chitin suspensions. *J. Phys. Chem. B*, 108:14991–15000, 2004.

[161] A. Lin and M. A. Meyers. Growth and structure in abalone shell. *Mater. Sci. Eng.*, 390:27–41, 2005.

[162] G. Bevelander and H. Nakahara. An electron microscope study of the formation of the nacreous layer in the shell of certain bivalve molluscs. *Calc. Tiss. Res.*, 3: 84–92, 1969.

[163] H. Nakahara. Nacre formation in bivalve and gastropod molluscs. In S. Suga and H. Nakahara, editors, *Mechanisms and phylogeny of mineralization in biological systems*, chapter 4.2, pages 343–350. Springer, 1991.

[164] A. M. Belcher, X. H. Wu, R. J. Christensen, P. K. Hansma, G. D. Stucky, and D. E. Morse. Control of crystal phase switching and orientation by soluble mollusk shell protein. *Nature*, 381:56–58, 1996.

[165] H. Nakahara. Calcification of gastropod nacre. In P. Westbroek and E. W. de Jong, editors, *Biomineralization and biological metal accumulation*, pages 225–230. Reidel, 1983.

[166] K. Wada. Spiral growth of nacre. *Nature*, 211:1427, 1966.

[167] Y. Levi-Kalisman, G. Falini, L. Addadi, and S. Weiner. Structure of the nacreous organic matrix of a bivalve mollusk shell examined in the hydrated state using cryo-TEM. *Journal of Structural Biology*, 135:8–17, 2001.

[168] Y. Fan, T. Saito, and A. Isogai. Preparation of chitin nanofibers from squid pen β-chitin by simple mechanical treatment under acid conditions. *Biomacromolecules*, 9:1919–1923, 2008.

[169] A. Morin and A. Dufresne. Nanocomposites of chitin whiskers from *Riftia* tubes and poly(caprolactone). *Macromolecules*, 35:2190–2199, 2002.

[170] G. De Luca and A. Rey. Chiral front propagation in liquid-crystalline materials: Formation of the planar monodomain twisted plywood architecture of biological fibrous composites. *Phys. Rev. E*, 69:011706, 2004.

[171] W. Burton, N. Cabrera, and F. Frank. The growth of crystals and the equilibrium structure of their surfaces. *Philosophical Transactions of the Royal Society of London A*, 243:299–358, 1951.

[172] A. Chernov. Protein crystals and their growth. *Journal of Structural Biology*, 142:3–21, 2003.

[173] F. Frank. The influence of dislocations on crystal growth. *Discussions of the Faraday Society*, 5:48–54, 1949.

[174] A. McPherson, Y. Kuznetsov, A. Malkin, and M. Plomp. Macromolecular crystal growth as revealed by atomic force microscopy. *Journal of Structural Biology*, 142:32–46, 2003.

[175] M. Markus and B. Hess. Isotropic cellular automaton for modelling excitable media. *Nature*, 347:56–58, 1990.

[176] P. Ball. *The self-made tapestry: Pattern formation in nature*. Cambridge University Press, 2001.

[177] J.H.E. Cartwright, O. Piro, and I. Tuval. Fluid dynamics in developmental biology: moving fluids that shape ontogeny. *HFSP J*, 0:000–000, 2009.

[178] A.G. Checa, J.H.E. Cartwright, and M.-G. Willinger. The key role of the surface membrane in why gastropod nacre grows in towers. *PNAS*, 106:38–43, 2009.

[179] Z. Tang, N.A. Kotov, S. Maganov, and B. Ozturk. Nanostructured artificial nacre. *Nature Materials*, 2:413–418, 2003.

[180] E Haeckel. Kristallseelen. In AL Mackay, editor, *Ernst Haeckel and biological form*. Leipzig, 1917.

[181] Y. Bouligand. Twisted fibrous arrangements in biological materials and cholesteric mesophases. *Tissue Cell*, 4:189–217, 1972.

[182] A.C. Neville. *Biology of fibrous composites: Development beyond the cell membrane*. Cambridge University Press, 1993.

[183] S. Cowin. Do liquid crystal-like flow processes occur in the supramolecular assembly of biological tissues? *Journal of Non-Newtonian Fluid Mechanics*, 119:155–162, 2004.

Published Work

- J. H. E. Cartwright, B. Escribano, and C. I. Sainz-Díaz, *The mesoscale morphologies of ice films: porous and biomorphic forms of ice under astrophysical conditions*, The Astrophysical Journal **687**, 1406–1414 (2008).

- B. Escribano, J. Vanyo, I. Tuval, J. H. E. Cartwright, D. L. González, O. Piro, and T. Tél, *Dynamics of tidal synchronization and orbit circularization of celestial bodies*, Physical Review E **78**, 036216 (2008).

- J. H. E. Cartwright, B. Escribano, O. Piro, C. I. Sainz-Díaz, P. A. Snchez, and T. Sintes, *Ice film morphologies and the structure zone model*, AIP Conference Series **982**, 696–701 (2008).

- C. I. Sainz-Díaz, B. Escribano, and J. H. E. Cartwright, *Microstructures in the formation of chemical gardens*, Materials Research Society Symposia Proceedings **1097E**, 1097-GG07-08 (2008).

- A. G. Checa, J. H. E. Cartwright, B. Escribano, and C. I. Sainz-Díaz, *Nacre: A unique biomaterial patterned by liquid crystals*, Materials Research Society Symposia Proceedings **1094E**, 1094-DD01-02 (2008).

- J. H. E. Cartwright, B. Escribano, and C. I. Sainz-Díaz, *Low-temperature ice films: The weird and wonderful forms of ice in space*, G.I.T. Laboratory Journal Europe **(3/4)**, 16–18 (2009).

- J. H. E. Cartwright, A. G. Checa, B. Escribano, and C. I. Sainz-Díaz, *Spiral and target patterns in bivalve nacre manifest a natural excitable medium from layer growth of a biological liquid crystal*, Proceedings of the National Academy of Science **106** (26), 10499–10504 (2009).

- J. H. E. Cartwright, B. Escribano, and C. Ignacio Sainz-Díaz, *Ice films follow structure zone model morphologies*, Thin Solid Films **518**, 3422–3427 (2010).

IN PREPARATION

- J. H. E. Cartwright, B.o Escribano, S. Khokhlov, and C. I. Sainz-Díaz, *Chemical gardens from silicates and cations of group II: A comparative study of composition, morphology and microstructure*, Physical Chemistry Chemical Physics, submitted, 2010.

- J. H. E. Cartwright, B. Escribano, and C. I. Sainz-Díaz, *Chemical gardens formation, morphology and composition. I. Effect of the nature of the cations*, Soft Matter, submitted, 2010.

- J. H. E. Cartwright, B. Escribano, C. I. Sainz-Díaz, and L. S. Stodieck, *Chemical-garden formation, morphology and composition. II. Chemical gardens in microgravity*, Soft Matter, submitted, 2010.

- J. Vanyó, B. Escribano, J. H. E. Cartwright, D. L. González, O. Piro, T. Tél, *A minimal dynamical model for tidal synchronization and orbit circularization*, Celestial Mechanics and Dynamical Astronomy, submitted, 2010.

- J. H. E. Cartwright, A. G. Checa, B. Escribano, and C. I. Sainz-Díaz, *Crystal Growth as an Excitable Medium*, Physical Review Letters, submitted, 2010.

- J. H. E. Cartwright, B. Escribano, H. Grothe, C. I. Sainz-Díaz, I. Tuval, and O. Piro, *Nonlinear dynamics of ice growth and charge production in thunderstorms*.